Magnetic trapping of atomic nitrogen and cotrapping of NH

A dissertation presented

by

Matthew Taylor Hummon

to

The Department of Physics

in partial fulfillment of the requirements

for the degree of

Doctor of Philosophy

in the subject of

Physics

Harvard University

Cambridge, Massachusetts

March 2010

Thesis advisor

John M. Doyle

Author

Matthew Taylor Hummon

Magnetic trapping of atomic nitrogen and cotrapping of NH

Abstract

We observe magnetic trapping of atomic nitrogen (^{14}N) and cotrapping of ground-state imidogen (^{14}NH, $X^3\Sigma^-$). Both are loaded directly from a room-temperature beam via buffer gas cooling. We trap approximately 1×10^{12} ^{14}N atoms at a peak density of 2×10^{12} cm^{-3} at 600 mK. We also trap similar numbers of the isotope ^{15}N. Observation times of magnetically trapped ^{14}N of over 100 s have been achieved. Utilizing a new pulsed cryogenic reservoir for introducing buffer gas into the cell, we are able to cotrap ^{14}N and ^{14}NH and subsequently rapidly remove most of the buffer gas. This allows for observation times of trapped NH of up to 10 s. This is sufficiently long to study N-NH collisions in the magnetic trap. From our observations, we estimate a ratio of elastic to inelastic N-NH collisions of $\gamma \approx 100$ at a temperature of 570 mK.

Contents

Title Page i
Abstract iii
Table of Contents iv
List of Figures vi
List of Tables viii
Citations to Previously Published Work ix
Acknowledgments x
Dedication xi

1 Introduction **1**
1.1 Motivation 1
1.1.1 Few-body physics 2
1.1.2 Precision measurement 4
1.1.3 Many-body physics 5
1.2 Techniques 5
1.2.1 Direct laser cooling of molecules 6
1.2.2 Sympathetic cooling of molecules 7
1.3 Cold collisions in a magnetic trap 8
1.3.1 Dipolar Relaxation 9
1.3.2 Electronic interaction anisotropy 10

2 Experimental Overview **19**
2.1 Trapping apparatus 19
2.2 Atomic and molecular beam source 23
2.2.1 Nitrogen RF plasma source 23
2.2.2 DC glow discharge source 25
2.3 Detection of trapped species 27
2.3.1 Nitrogen Detection 27
2.3.2 NH detection 33
2.3.3 Chromium 34
2.4 Trap Loading and Measurement 35

3 Results and analysis **38**
3.1 Trap Dynamics . . . 39
3.1.1 Trapped atom density distribution . . . 39
3.1.2 Inelastic collision trap loss . . . 40
3.1.3 Evaporative loss . . . 43
3.1.4 Discussion of two-body loss . . . 45
3.1.5 Background gas collisions . . . 45
3.1.6 Assumptions in trap dynamics calculations . . . 47
3.2 N-N collisions . . . 48
3.2.1 Trapping of ^{15}N . . . 53
3.3 N-NH collsions . . . 54

4 Future Directions **59**
4.1 Killing the film . . . 59
4.2 Improved Nitrogen Detection . . . 62
4.3 Cold atomic nitrogen beam source . . . 63

A Atomic Nitrogen Detection **65**
A.1 Two-photon excitation . . . 66
A.2 Characterization of TALIF parameters . . . 70
A.2.1 Detection sensitivity . . . 81
A.2.2 Conclusion . . . 82

B Atomic Chromium Data **84**

C Simulation of Trap Dynamics **89**
C.1 Overview of simulation . . . 89
C.2 Results of Simulation . . . 93

D Manganese Monohydride **98**
D.1 Introduction . . . 98
D.2 Previous Work on MnH . . . 99
D.3 Preparation of Targets . . . 100
D.4 Experimental Setup . . . 101

List of Figures

1.1 Simple illustration of interaction potentials for collisions 12
1.2 N - NH interaction potential 15
1.3 N-NH collision cross-section without dipolar contribution 16
1.4 Simple illustration of resonant interactions 17

2.1 Vacuum chamber 21
2.2 Trapping apparatus 22
2.3 Depiction of beam sources 23
2.4 Setup for evacuation of DC discharge manifold 26
2.5 Two-photon absorption laser induced fluorescence in atomic nitrogen. 27
2.6 Depiction of fluorescence detection 29
2.7 207 nm laser setup. 32
2.8 Repeated 207 nm acquisition 36
2.9 Nitrogen signal normalization 37

3.1 A superb nitrogen time decay 49
3.2 Nitrogen time decay at constant cell temperature. 50
3.3 Nitrogen k_{2b} versus η. 51
3.4 Trap average inelastic loss rates from quantum scattering calculations by Timur Tscherbul. 53
3.5 N-15 trapping data 54
3.6 NH decay. 55
3.7 NH N cell temperature deviation 56
3.8 N decay for density calibration. 57
3.9 NH loss vs N density 58

4.1 Helium vapor pressure curves 60

A.1 207 nm intensity distribution at focus 71
A.2 Pulse dye laser resonator cavity 72
A.3 Fizeau interferometer 74

A.4 Pulsed dye laser spectral analysis 75
A.5 May 6 spectrum 76
A.6 Nitrogen signal versus excitation energy 77
A.7 Electronic energy levels in iron for laser induced fluorescence 78
A.8 Laser induced fluorescence spectrum of iron. 80
A.9 May 6 spectrum 81

B.1 Trapped Cr spectrum 85
B.2 Cr time decay 86
B.3 Cr 1-body loss rates. 87
B.4 Cr 2-body loss rates. 88
B.5 Cr trap loss due to leaky solenoid valve. 88

C.1 Polynomial fit to magnetic field. 91
C.2 DSMC simulation, $f(\eta)$ 94
C.3 DSMC simulation, Equilibrium η 95
C.4 DSMC simulation, Fraction of Helium collisions leading to evaporative loss 96
C.5 DSMC simulation, everything 97

D.1 MnH fluorescence spectrum. 102
D.2 MnH decay 103
D.3 MnH decay vs buffer gas density 104
D.4 MnH decay 105

List of Tables

1.1 Polarizabilities of selected S-state atoms 13
1.2 Interaction anisotropy in atom-molecule collisions. 14

2.1 Measured transmission of materials at 207 nm 31

3.1 Solutions to trap loss rate equations. 47

A.1 Parameters and typical values for atomic nitrogen excitation. 69

Citations to Previously Published Work

Portions of this thesis have appeared in the following paper:

M. T. Hummon, W. C. Campbell, H.-I Lu, E. Tsikata, Y. Wang, and J. M. Doyle, "Magnetic trapping of atomic nitrogen (^{14}N) and cotrapping of NH (X $^3\Sigma^-$), " Phys. Rev. A **78**, 050702(R) (2008).

Acknowledgments

Acknowledgments go here.

Dedication goes here.

Chapter 1

Introduction

Driven by the wide range of promising applications and new science, from quantum simulation and precision measurement, to the study of cold collisions and their role in cold chemistry and astrophysics, the field of cold and ultracold molecules has undergone great growth in the last decade [1]. To be able to access the full range of applications, one desires a general technique for producing dense, ultracold samples from a wide range of molecular species. A promising route toward this end, and the subject of this thesis, is to cotrap atoms and molecules and sympathetically cool the molecules through collisions with the cooled atoms.

1.1 Motivation

Following the lead of an excellent review article [1] on the field of cold and ultracold molecules, the scientific motivation for the studies of these systems can be divided into roughly three areas: few-body physics, precision measurement, and many-body

physics.

1.1.1 Few-body physics

It is hard to distill the field of few body physics into a few sentences, as collisions between atoms, molecules, and ions encompasses such a vast range of applications its hard to know where to begin. Recent progress has focussed on the study of near-threshold inelastic collisions by colliding Stark decelerated molecules with supersonic atomic or molecular beams [2, 3]. Other techniques aim to control cold collisions by the application of external electromagnetic fields [4]. The development of could sources of chemically interesting species is important for the study of reactions at cold temperatures and their applications to astrophysics. Both N and NH fall into this category so I will spend the next few paragraphs expanding on the study of cold chemistry.

Reactions in cold gas phase atom-molecule systems play a key role in dense interstellar clouds [5, 6]. If cold cotrapped atoms and molecules could be created at sufficient density, the parameters characterizing these reactions could be studied in the laboratory. Such studies may also lead to observation of novel chemical reaction pathways such as tunneling [7, 8].

There has been considerable interest in interstellar nitrogen recently, as new astronomical observations have provided evidence that most interstellar nitrogen in the gas phase is not, as previously thought, in molecular form, but rather in atomic form [6, 9, 10]. A network of cold chemical reactions [11] involving atomic nitrogen and neutral molecular radicals (OH, NO, CH, CN, and NH, in particular) [5, 6, 12] play an

important role in interstellar gas-phase chemistry models. Specifically, the existence of small barriers ($\sim$ 25 K) to these reactions is an important parameter and is beyond the sensitivity of current theoretical calculations [6].

For collisions at "very low temperatures" in the range of 4 - 100 K, many partial waves contribute to collisions, and the reagents are typically expected to be in a thermal mixture of internal quantum states and relative orientations. As a result, the chemical reaction rate is expected to be dominated by the channel in which the atom and molecule approach each other with anti-aligned spins. Chemical reaction rates are calculated using "capture" theory. Essentially, if the colliding partners have enough energy to overcome the centrifugal barrier for a particular channel, then the probability of having the reaction is set to one. If the colliding partners cannot make it to short range, then the probability of having the collision is zero. This approach works well for describing barrierless reactions down to about 10 K when the interaction is dominated by long range forces, as is the case for ion-molecule collisions [13]. For neutral-neutral chemical reactions at cold temperatures, the short range interactions are likely to play a significant role.

Theoretical study of these reactions predict rate coefficients on the order of $k \sim 10^{-11}$ cm^3 s^{-1} at temperatures of $\sim$ 10 K [5, 12], suggesting that the reactions may be observable using a cold, high density sample of trapped atomic nitrogen.

One technique for studying chemical reactions of neutral-neutral species is cinétique de réaction en ecoulement supersonique uniforme, or CRESU [14]. It achieves cooling of the reagents via a continuous flow supersonic expansion through a Laval nozzle. The reagents are typically created via pulsed laser photolysis of a suitable precursor.

Studies of about 50 different neutral-neutral reactions have been achieved at temperatures of 25 K, with some as low as 13 K using the CRESU technique [14]. The lowest temperature for a reaction between an atomic radical and molecular radical using this technique is 39 K for the reaction O + OH$\rightarrow$ H_2 + O, yielding a rate constant $k = (3.5 \pm 1.1) \times 10^{-11}$ cm^3sec^{-1} [15]. The development of cold bright sources for atomic and molecular radicals, combined with new guiding and trapping techniques promises to push beyond the limitations of studying chemistry in supersonic expansions.

1.1.2 Precision measurement

The internal structure of molecules make them particularly good candidates for probing new physics. In particular, the internal structure of molecules promises to lead to enhanced sensitivity to permanent electric dipole moments (EDMs) of the electron[16, 17] and to time variation of fundamental constants, such as changes in the fine structure constant and the electron to proton mass ratio [18–20]. For example, in the case of measurements of the electron EDM, polar molecules, such as ThO can be completely polarized with laboratory electric fields of 100 V/cm, which lead to internal electric fields experienced by the electron of 100 GV/cm [17]. This enhancement of the electric field experienced by the electron corresponds directly to an enhancement in electron EDM sensitivity. Using a source of cold ThO molecules also leads to a sensitivity enhancement due to an increase of molecules in the appropriate ro-vibrational quantum state for the measurement. Further information about the use of molecules in precision measurement can be found in Reference [1].

1.1.3 Many-body physics

The study of many-body physics with ultracold dipolar molecules has mainly focused on the phase diagrams of dipolar molecules, confined in a harmonic trap or an optical lattice, that arise from the long range and anisotropic nature of the dipole-dipole interaction [1]. With the ability to engineer interactions between molecules, dipolar molecules in optical lattices are considered interesting candidates for quantum simulation of condensed matter systems [21], or as use as qubits in a quantum computer [22].

1.2 Techniques

Many of the applications stated above require or benefit from a source of ultracold, dense molecules. For example, quantum information applications require molecules to be loaded into an optical trap or microchip surface trap, with typical depths on the order of 1 to 10 mK and dimensions of the order of 100 μm [1]. Experiments studying collisions, such as ones involving cold chemistry, dipolar collisions, or evaporative cooling, benefit from higher collision rates, and in some cases, suppressed inelastic channels [2, 3, 23].

Techniques for generating cold molecules generally fall into one of two categories. The first is to assemble ultracold atoms using photo- or magneto-association techniques [1]. When combined with coherent transfer to the rovibrational ground state, one can achieve trapped, ground state molecules with high phase space density [24]. With few exceptions [25], this technique is limited to bi-alkali species, and more gen-

erally is limited to atoms that can be cooled to the ultracold regime. This excludes many chemically interesting species such as oxides, carbides, and halides, where optical cooling transitions lie deep in the ultraviolet.

The second technique starts with a warm source of molecules and slows and cools them directly. Examples of this type of technique include buffer gas cooling [26], Stark [27], Zeeman[28, 29], and optical slowing[30], and kinematic cooling[31]. While these techniques are applicable to a large class of molecules, the resulting trapped molecules typically have have temperatures on the order of 10 to 500 mK, and densities on the order of 10^8 cm^{-3}. A technique to further cool and compress these samples would allow a sizable class of molecules to be cooled into the ultracold ($T < 1$ mK) regime. The potential for new applications and new science has motivated a significant amount of theoretical and experimental research toward this end [1]. In the next two sections, we will discuss two techniques toward this end: direct laser cooling of molecules and sympathetic cooling of molecules with cotrapped atoms.

1.2.1 Direct laser cooling of molecules

One approach is to develop laser cooling techniques to directly cool and trap the molecules. In a recent Letter [32], Stuhl and coworkers layout a design for an electrostatically remixed magneto-optical trap (ER-MOT) for the cooling and trapping of polar molecules. The challenge in adapting a traditional atom MOT for use with polar molecules lies in creating a quasi-closed cooling transition in the complex rovibrational electronic manifold of diatomic molecules. Stuhl and coworkers show that by choosing a molecule with good Franck-Condon overlap, cooling on a rotationally

closed $J'' \rightarrow J'' - 1$ transition, and using pulsed nonadiabatic electric fields to remix molecule ground states to remove dark states, a quasi-closed cooling transition can be formed with minimal laser complexity. Despite these restrictions, a sizable class of molecules, including some metal hydrides, metal halides, metal oxides, and metal carbides, fit this criterea.

Very recently, Shuman and coworkers have demonstrated deflection of a cold beam of SrF using the radiative force generated from a quasi-closed optical cycling transition [33]. With straightforward improvements to the apparatus and the addition of a second vibrational repump laser, they expect to be able to scatter more the 10^5 photons, which would provide sufficient cooling of the beam to load it into a trap.

1.2.2 Sympathetic cooling of molecules

Another approach toward further cooling of molecular species produced by direct cooling techniques is to sympathetically cool them with cotrapped atoms [1, 23, 34]. Cooling of the atomic sample occurs via laser cooling or evaporative cooling, and collisions between the atoms and cotrapped molecules in turn cool the molecular sample. For this technique to provide efficient cooling, the rate of molecules lost or heated due to inelastic collisions with the atoms must be small compared to rate of thermalizing, elastic collisions. A general rule of thumb is the ratio of elastic to inelastic collisions, $k_{\mathrm{el}}/k_{\mathrm{in}} \equiv \gamma > 100$. An understanding of the physical mechanisms involved in inelastic collisions between atoms and molecules is critical for choosing an atom-molecule pair that will lead to efficient sympathetic cooling. In the next section we will review the current understanding of these collisions.

1.3 Cold collisions in a magnetic trap

As discussed earlier, molecules produced using direct cooling techniques have temperatures in the tens to hundreds of mK. At these temperatures, electrostatic or magnetostatic traps must be used to provide sufficient trap depth. For these traps, low field seeking states of the trapped species must be used. These low field seeking states have higher energy than the high field seeking states. Inelastic collisions between species can cause the low field seeking state to relax to the lower energy, high field seeking state, leading to loss of the species from the trap. This process of Zeeman relaxation has been studied in many atomic [35–38] and more recently combined atomic and molecular systems [39–43].

As describe above, we are particularly interested in Zeeman-state-changing collisions that lead to loss of molecules from our magnetic trap. Typically, atoms and molecules are trapped in spin-streched states, $|J, m_J = J\rangle$. When two atoms collide, for one atom to change its Zeeman state, $|J, m_J = J\rangle \rightarrow |J, m_J = J - \Delta m_J\rangle$, conservation of angular moment requires that the change in angular momentum Δm_J goes into the rotational angular momentum of the two colliding atoms, as it cannot go into the electronic angular moment of the second atom. Hence we are interested in interactions that can couple the (internal) electronic angular momentum of an atom to the (external) rotational angular momentum of the colliding system.

In collisions between two particles with magnetic moments, the magnetic dipolar interaction provides such a coupling. It has the form:

$$V_{dd} = \frac{\mu_{\mathbf{1}} \cdot \mu_{\mathbf{2}} - 3(\hat{\mathbf{R}} \cdot \mu_{\mathbf{1}})(\hat{\mathbf{R}} \cdot \mu_{\mathbf{2}})}{R^3} \tag{1.1}$$

Alternatively, if the electronic interaction potential between the two colliding species is anisotropic, the interaction potential itself can drive Zeeman-state changing collisions [36]. To study the role that these two interactions play in Zeeman-state changing collisions in magnetic traps, a variety of experiments and theoretical calculations have been performed on both atomic and molecular species. We will briefly summarize them here, and discuss their implications for sympathetic cooling of molecules in magnetic traps.

1.3.1 Dipolar Relaxation

For collisions between two magnetically trapped S-state atoms, the magnetic dipolar interaction is typically the dominant inelastic channel, as the interaction potential for two colliding S-state atoms is isotropic to a high degree. From Fermi's golden rule, we expect the inelastic collision rate to scale roughly as μ^4, i.e. as the square of the matrix element of the interaction, $\left|\langle f|\, V_{dd}\, |i\rangle\right|^2 \approx \mu^4$. For alkali metal atoms (1 μ_{B}) and meta-stable helium (2 mu_{B}), inelastic rates from dipolar relaxation are small enough to allow for efficient evaporative cooling of the samples to quantum degeneracy. For atomic chromium (6 mu_{B}), the large inelastic rates from dipolar relaxation prevent efficient evaporative cooling of the sample in a magnetic trap [44–46]. From this rule of thumb, the magnetic moments of atomic nitrogen (3 mu_{B}) and NH (2 mu_{B}) are expected to be small enough to allow for efficient evaporative cooling of atomic nitrogen and sympathetic cooling of NH. Calculations of dipolar relaxation in N-N collisions using *ab initio* interaction potentials are performed by Timur Tscherbul in conjunction with the experimental work described in this thesis.

1.3.2 Electronic interaction anisotropy

For collisions of non-S-state atoms and molecules, the anisotropy of the interaction potential plays a significant role in Zeeman-state-changing collisions in a magnetic trap. By using helium as a structureless, non-magnetic collision partner, the interaction anisotropy of the atomic[37, 47] or molecular[39–41, 48] trap species can be probed directly. For example, in the case of helium-NH collisions, the anisotropy of the $^3\Sigma$ ground electronic state induced by the spin-spin interaction in the molecule drives Zeeman relaxation of NH in helium-NH colliisions [41]. Thus, when considering atomic species as candidates for sympathetic cooling partners for a molecule such as NH, it is important to consider the anisotropy of the interaction potential between the atom-molecule pair.

There has been a significant amount of theoretical investigation of the interaction potentials between (alkali metals/alkaline earths)-(NH/OH/NH_3) species. Alkali metals and alkaline earth atoms can be laser cooled to temperatures of 1 mK, and hence are attractive sympathetic coolant partners for molecules. The molecules NH, OH, and NH_3 are routinely trapped in magnetostatic or electrostatic fields at temperatures of 10 - 500 mK using buffer gas cooling or Stark deceleration.

For a concrete example, let us consider the A-NH_3 system[1] studied by Zuchowski and Hutson, where A stands for either an alkali metal or alkaline earth atom. In a recent paper [43] they investigate the origins of the anisotropy for this system, specifically they look at the anisotropy of the interaction energies arising from three

[1]Even though NH_3 is a molecule with symmetric-top symmetry, in collisions with an atomic species one can use a pair of interaction potentials where the dominant potential represents a cylindrical average about the NH_3 molecular axis, and thus is similar to that of a diatomic molecule.

separate mechanisms: the electrostatic, exchange, and dispersion interaction. The electrostatic interaction refers to the attractive part and the exchange interaction refers to the repulsive part (Pauli exclusion) of the intermolecular potential. The dispersive interaction refers to the typical isotropic C_6 and anisotropic $C_{6,2}$ interaction arising from the polarizability of each species. From their calculations they conclude in the A-NH_3 system the anisotropy is dominated by the attractive electrostatic interaction. When the atom approaches from the H_3 side, the electrostatic and exchange interactions roughly cancel and the interaction is dominated by the dispersive forces. When the alkali atom approaches from the N side, the attractive electrostatic interaction dominates due to the chemical bonding nature of the interaction. This large anisotropy of the electrostatic interaction is expected to lead to large inelastic rates in collisions of NH_3 with alkali metal and alkaline-earth atoms. Figure 1.2 shows a qualitative picture of the anisotropic interaction potentials. Classically, when an atom approaches a molecule on an interaction potential that depends on θ, it can exert a torque on the molecule, which can lead to the reorientation of molecule's magnetic moment.

From these theoretical studies of atom - molecule interactions, we see that it is desirable to reduce the amount of anisotropy arising from the electrostatic, exchange, and dispersion interactions. In Ref. [49], Lara and coworkers suggest a set of guidelines for choosing an atom-molecule system for sympathetic cooling: (i) light atomic partners with small polarizability will lead to larger centrifugal barriers, reducing the number of available inelastic collision channels, (ii) weak coupling of the molecule's valence electron to the molecular axis, as is the case for Hund's case b molecules

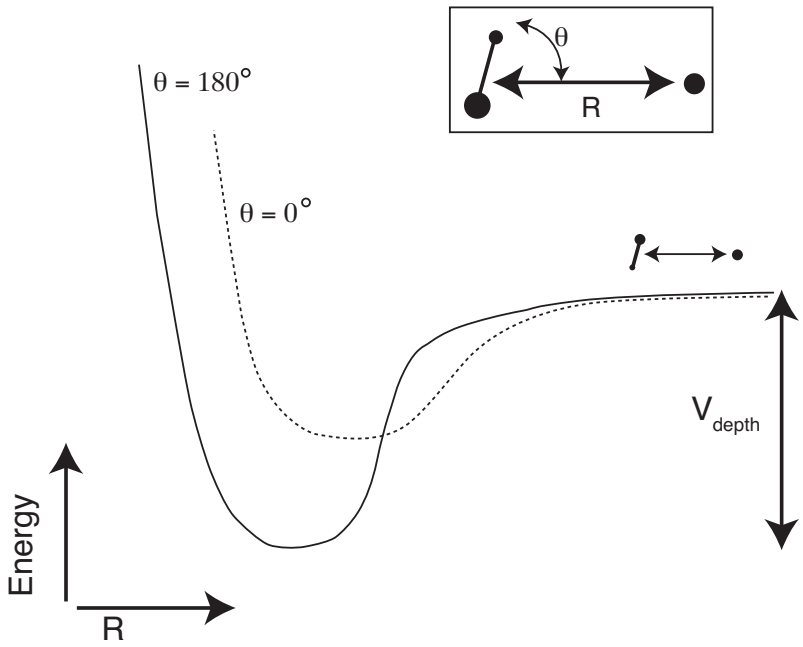

Figure 1.1: Simple illustration of interaction potentials for collisions. The actual interaction potential is a 2-dimensional surface over intermolecular spacing **R** and the angle θ. Here are shown two cuts from the surface. $\theta = 0°$ corresponds to the A-HN orientation and $\theta = 180°$ corresponds to the A-NH orientation.

atom	electronic state	mass	polarizability (a_0^3)	transition (nm)
H	$^2S_{1/2}$	1	4.5	122
He	$^1S_0$	4	1.4	58
He*	$^3S_1$	4	300	1083
Ne	$^1S_0$	20	2.7	74
Ar	$^1S_0$	40	11	107
N	$^4S_{3/2}$	15	7.6	120
P	$^4S_{3/2}$	31	25	178
As	$^4S_{3/2}$	75	30	189
Li	$^2S_{1/2}$	7	165	671
Na	$^2S_{1/2}$	23	160	589
K	$^2S_{1/2}$	39	293	766
Rb	$^2S_{1/2}$	87	320	780
Be	$^1S_0$	9	37	235
Mg	$^1S_0$	24	75	285
Ca	$^1S_0$	40	160	423
Zn	$^1S_0$	64	45	214
Cu	$^2S_{1/2}$	63	50	325
Ag	$^2S_{1/2}$	107	58	328
Au	$^2S_{1/2}$	197	44	242
Cr	$^7S_3$	52	79	425
Mn	$^6S_{5/2}$	55	65	403

Table 1.1: Static electric dipole polarizabilities of selected S-state atoms, polarizabilities from Refs. [50–54], transition wavelengths from Ref. [55].

like NH, is beneficial, and (iii) atoms that produce isotropic interaction energy surfaces with the molecule are needed. For example, one might expect light, closed shell alkaline earths to produce more isotropic interaction surfaces due to their low polarizability and closed shell structure. Tables 1.1 and 1.2 summarize the atomic polarizabilities and interaction anisotropy for potential atom-molecules systems.

From inspection of these tables, we see that light closed shell atoms, such as He and Mg have favorable collision probabilities with NH—indeed buffer gas cooling of NH with helium requires favorable collision properties. Additionally atomic nitrogen,

System	V_{depth} at θ_1 (cm^{-1})	V_{depth} at θ_2 (cm^{-1})
He-NH[a]	20	10
N-NH[b]	78	88
Alk-NH[c]	~ 700	~ 100
Mg-NH[c]	107	103
Ca-NH[c]	166	105
Mg - NH_3[d]	888	116
Rb - NH_3[d]	1862	110

[a] Estimated from Figure 1 in Ref. [40].
[b] From Jacek.
[c] Ref. [56].
[d] Ref. [43].

Table 1.2: Interaction anisotropy in atom-molecule collisions.

also a light atomic species with low polarizability, has a small electronic interaction anisotropy with NH. The closed shell species, He and Mg, cannot be confined using magneto- or electrostatic forces alone. Magnesium can be confined in a MOT at temperatures of 1 mK [57], and recent scattering calculations for the Mg-NH system indicate favorable collision rates at temperatures below 10 mK [42]. Atomic nitrogen has the advantage of being paramagnetic, and thus can be cotrapped with NH in a magnetic trap. Figure 1.4 shows two cuts through the theoretical N-NH interaction potential. We observe the the potential surface is fairly isotropic; the two potential curves for approach of the N atom from opposite sides of the molecule are very similar. Preliminary scattering calculations for the N-NH system performed by Timur Tschurbul are shown in Figure 1.3. The calculations shown here only show the effects of the electronic interaction anisotropy between N-NH; the inelastic loss contribution from the dipolar interaction is currently being calculated and finalized. From these calculations, we see that the inelastic collision cross section for N-NH system is larger

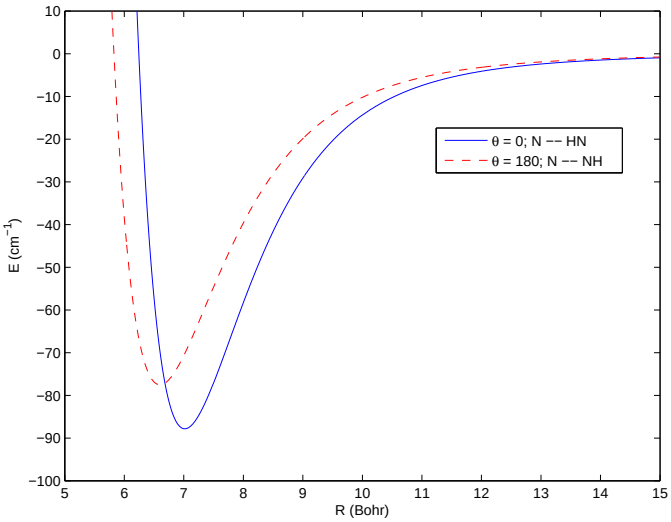

Figure 1.2: Calculated N - NH interaction potential, provided by Jacek Klos.

than the He-NH system, as expected from the larger anisotropy of the interaction. Nevertheless, the inelastic N-NH cross section from the interaction anisotropy is still at least two orders of magnitude smaller than the elastic cross section across a wide range of collision energies—small enough that sympathetic cooling may be possible.

The resonant structure in the N-NH inelastic collision cross-section is likely due to Feshbach-type resonances, as depicted in Fig. 1.4. The well depth, ($\sim 90\text{cm}^{-1}$), of the interaction potential is larger than the rotational spacing of the NH molecule ($E(N=1) - E(N=0) = 32\ \text{cm}^{-1}$). Hence, when the energy of a molecular bound state in the excited molecular potential coincides with the energy of the incoming atom-molecule system, a collision resonance occurs and enhances the inelastic cross section.

On a final note, we observe that atoms with favorable collision properties for sympathetic cooling of molecules will typically have small dispersion coefficients to reduce

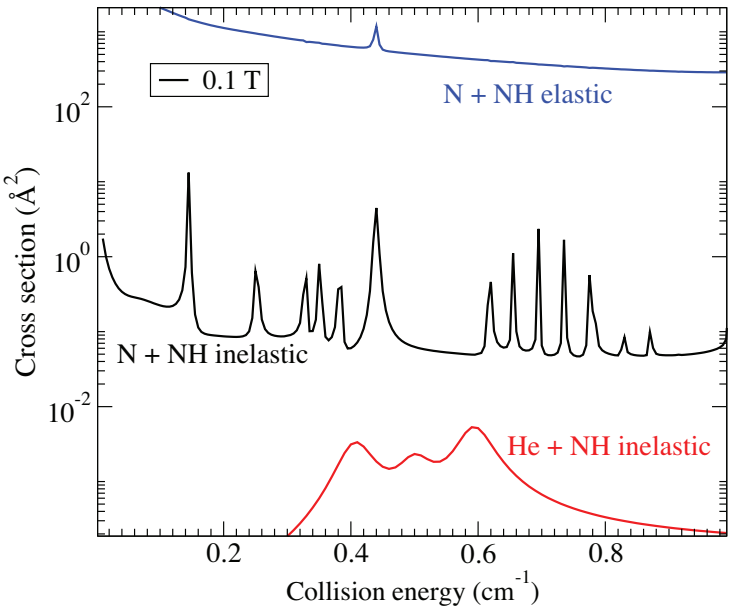

Figure 1.3: N-NH collision cross-section without dipolar contribution, calculated at a magnetic field of 0.1 T from Timur Tscherbul

the overall anisotropy during collisions. Dispersion coefficients involve integrals over all frequencies of the dynamic polarizability [58], where the dynamic polarizability, $\alpha(\omega)$ can be expressed as

$$\alpha(\omega) = \frac{2e^2}{3} \sum_m \frac{(E_m - E_n) \left| \langle m | \, \mathbf{r} \, | n \rangle \right|^2}{(E_m - E_n)^2 + (\hbar\omega)^2} \tag{1.2}$$

We see from this expression, that a significant contribution to the dispersion coefficients will be from the static dipole polarizability, $\alpha(0)$. Hence, atoms with small static dipole polarizabilities can be expected to have more favorable properties for sympathetic cooling than ones with larger. We see from equation 1.2, that this necessarily requires the first allowed electric dipole transition to have a large transition energy. As shown earlier in Table 1.1, atoms with small polarizability have their first accessible electric dipole transition in the ultraviolet, 285nm for Mg and 120nm for

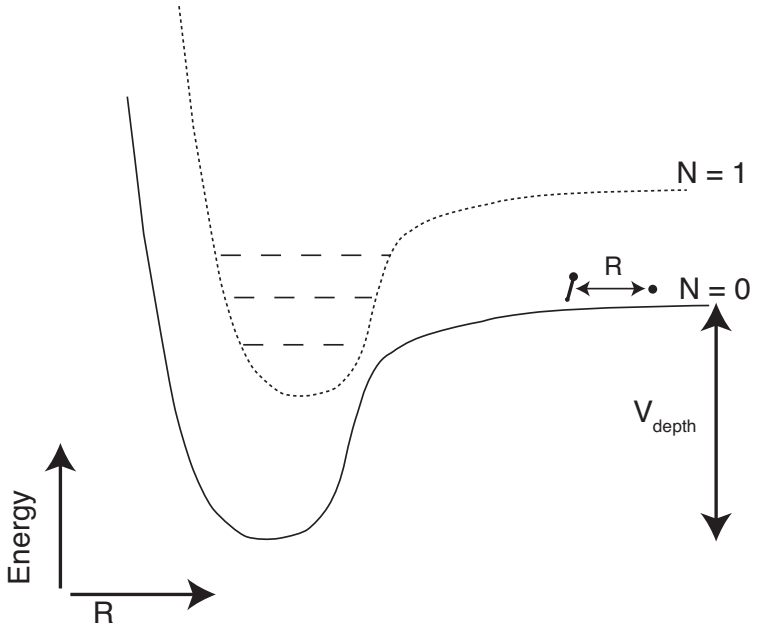

Figure 1.4: Simple illustration of resonant interactions. Dashed lines indicate bound states in the potentials. Here, N refers to the rotational quantum number of the diatomic molecule. The atom-molecule complex collide on the ground state, N=0 interaction potential. If the depth of the interaction potential, V_{depth}, is large compared to the molecule rotational spacing, then Feschbach-type resonances can occur in atom-molecule collisions.

N. Thus, atoms that have favorable collision properties for sympathetic cooling of molecules, such as Mg and N, are themselves technically challenging to laser cool, at least until high power ultraviolet lasers become available.

Chapter 2

Experimental Overview

The development of the trapping apparatus for the N and NH experiment has spanned four Ph.D. theses, [59–61]. The first section summarizes the current state of the trapping apparatus and details the recent changes made to it for working with atomic nitrogen. The second section describes the atomic and molecular beam sources used for loading the magnetic trap. The third section describes the techniques used for spectroscopic detection of the trapped species.

2.1 Trapping apparatus

The traditional buffer gas magnetic trapping experiments in our lab have used a superconducting magnet immersed in liquid helium. An inner vacuum chamber designed to fit inside the bore of the superconducting magnet contains the buffer gas trapping cell. Access to the inner vacuum chamber is limited to a 3 in window looking into the bore of the magnet.

To achieve greater access to the trapping region, both optically and mechanically, the superconducting trap magnet for the NH experiment was designed to run in vacuum, rather than immersed in liquid helium. A schematic of the vacuum chamber is shown in Figure 2.1. The trap magnet is surrounded by radiation shielding, thermally anchored at 4 K and 77 K, and the magnet itself is thermally anchored to a liquid helium bath with copper mechanical supports. A closed cycle pulse tube cooler, not shown, is used to provide additional cooling for the radiation shields and superconducting magnet leads. The room temperature molecular beam, shown on the left of Figure 2.1, enters the trapping region via 1 cm apertures in the radiation shields and buffer gas cell. The cylindrical copper buffer gas cell is cooled to a temperature of approximately 600 mK via a thermal link to a ^{3}He refrigerator, not shown.

Loading of the magnetic trap is achieved through thermalization of the species-to-be-trapped via collisions with the helium buffer gas. The superconducting magnetic trap provides a spherical quadrupole trapping potential with a trap depth of 3.9 T, determined by the magnetic field at the buffer gas cell wall. The magnetic field contours of the trapping potential are shown in gray in figure 2.2(b). The resulting depth of the magnetic trap expressed in temperature is about 5 K for NH and 7.5 K for N, much larger than the 600 mK temperature of the buffer gas.

To ensure that the species to be trapped thermalizes with the buffer gas in the volume of the trapping region, a buffer gas density on the order of $(10^{15}-10^{16})$ cm^{-3} is used. In the first phase of the experiment, this density was maintained in the cell with a continuous flow of buffer gas into the cell supplied from a fill line to room temperature, as depicted in Fig. 2.2(a). With careful heat sinking of the fill line, this

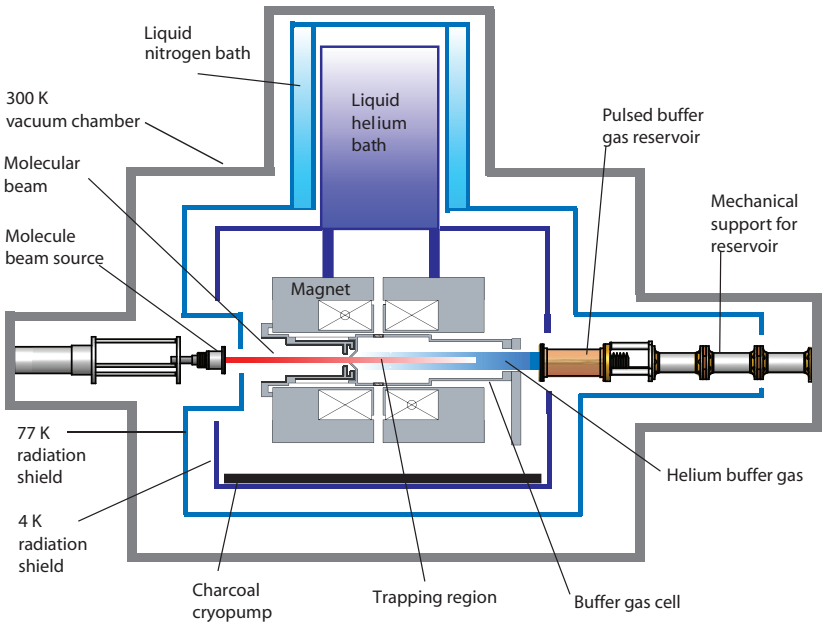

Figure 2.1: Vacuum chamber

allowed for the reliable, repeatable buffer gas densities to be achieved with minimal heating to the buffer gas cell. In the second phase of the experiment, the buffer gas was pulsed into the cell simultaneously with the species to be trapped, as shown in Fig. 2.2(b). This pulsed buffer gas loading technique was developed to allow for a more rapid removal of the buffer gas from the trapping region after the species-to-be-trapped has thermalized with the buffer gas. Removal of the buffer gas is necessary to study collisions of cotrapped atoms and molecules and to evaporatively cool the trap species to lower temperatures. Development of the pulsed buffer gas loading technique is described in the thesis of Edem Tsikata [61].

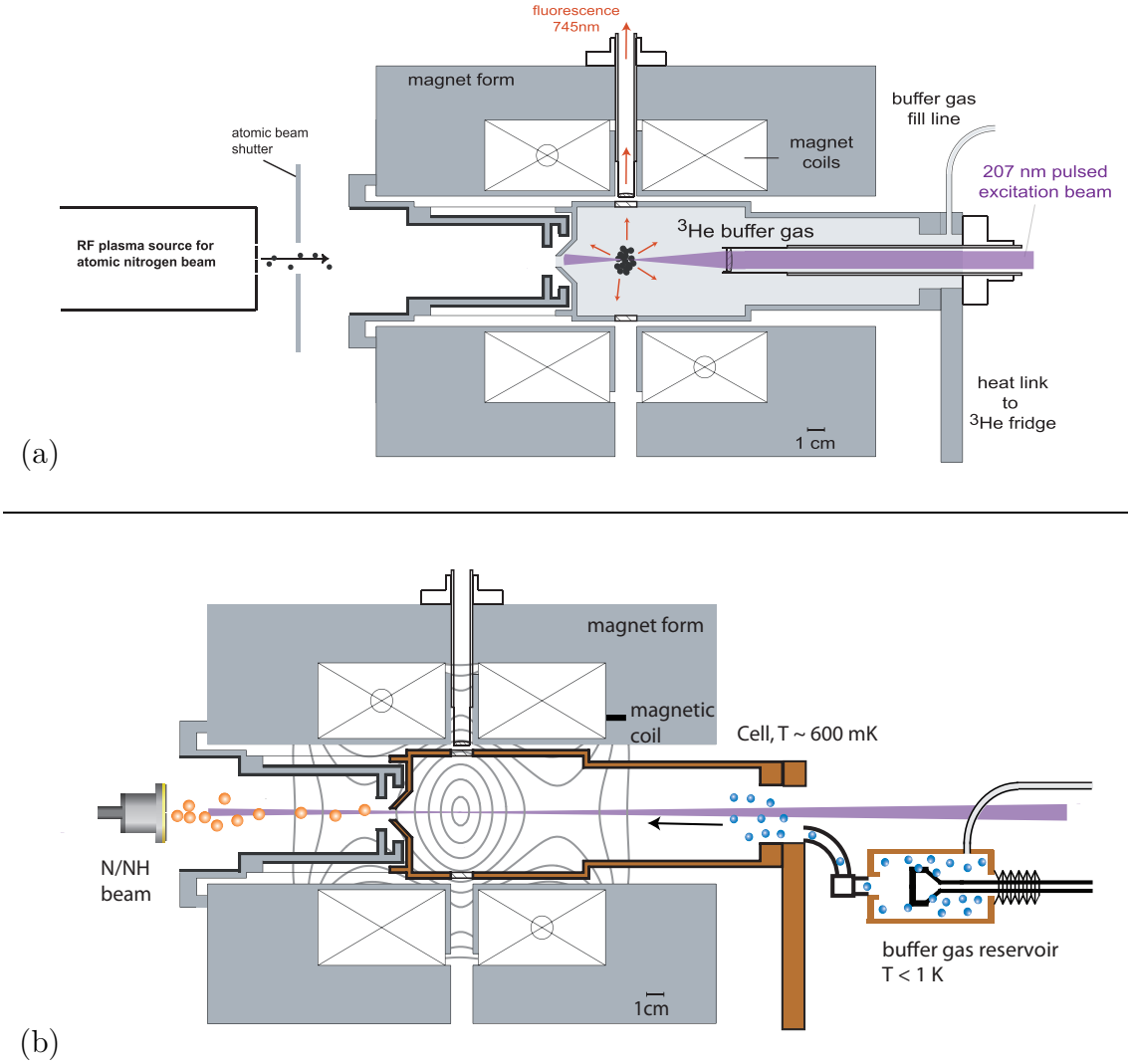

Figure 2.2: Trapping apparatus. (a) Trapping apparatus as used in phase I of the experiment. (b) Trapping apparatus showing changes made for phase II of the experiment.

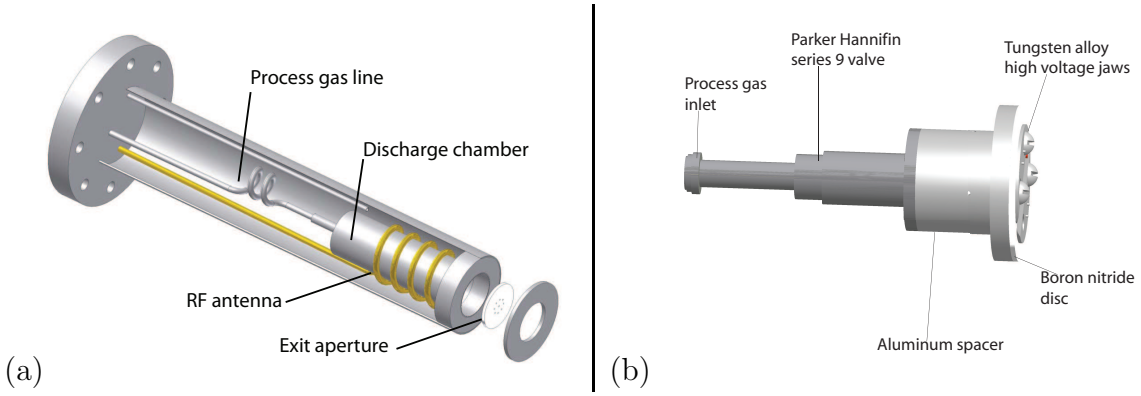

Figure 2.3: Molecular beam sources. (a) Depiction of the RF plasma source. (b) Depiction of DC glow discharge source with solenoid valve[61].

2.2 Atomic and molecular beam source

A principle advantage of the buffer gas trapping apparatus described above is the ability to load atoms or molecules into a magnetic trap from a room temperature beam, as a wide range of species can be accessed by various techniques. For the experiments described in this thesis, we generated molecular beams using two different techniques: in phase I we used a RF plasma source, and in phase II we used a DC glow discharge. These techniques were chosen since the production of the species of interest were well characterized.

2.2.1 Nitrogen RF plasma source

The molecular beam epitaxy community has developed techniques for creating beams of a range of species important for semiconductor growth. In particular, atomic nitrogen is an important dopant for certain III-V semiconductor materials. As such, high flux sources of atomic nitrogen have been developed and characterized [62].

For our experiment we used an Oxford Applied Research, model CARS-25 RF

plasma source. The basic operation principle is a radio-frequency plasma discharge is sustained in a chamber while process gas, in our case N_2, is flowed through the discharge chamber, as shown in Figure 2.3(a). The plasma is sustained by resonantly coupling 500 W of power at 13.56 MHz into an RF antenna wrapped around the discharge chamber. When the plasma source operates in high-brightness mode, characterized by increased fluorescence from the discharge chamber, dissociation efficiencies of $N_2 \rightarrow N$ can reach as high as a few percent [62]. With process gas flow rates of 1 to 2 sccm this corresponds to an atomic flux of 10^{16} atoms s^{-1} sr^{-1}. With the addition of H_2 to the process gas or use of NH_3 as the process gas, both N and NH can be simultaneously produced in the molecular beam for co-loading into the magnetic trap.

Initiation of the RF discharge must be done at low operating powers, so as not to damage the RF electronics that run the plasma source. Since the presence of the plasma effects the resonance conditions of the RF antenna through inductive coupling, the RF power to the plasma source must be slowly ramped up and the impedance matching tuning capacitors adjusted accordingly to maintain a stable discharge. During operation, the plasma source is cooled via gas flow from a liquid nitrogen dewar. The temperature of the discharge chamber also effects the stability of the discharge, and the cooling gas flow must also be tuned and monitored during operation of the plasma source. To achieve stable operation of the discharge source at full RF power often requires about 20 minutes time of tuning the various discharge parameters and waiting for temperatures to stabilize. As a result, the plasma source must be run continuously during the experiment. In order to isolate the trapping region from

plasma source a simple shutter is placed after the plasma source and just before the entrance to the 77 K radiation shield, as shown in Figure 2.2(a). The shutter consists of a copper plate, heat sunk at 77 K, that is mounted on a rod connected to a rotational vacuum feed through. A 1 cm aperture in the copper plate allows the molecular beam to pass to the trapping region for certain orientations of the plate. A pneumatic actuator is used to rotate the copper plate in front of the molecular beam to generate loading pulses of 20 ms duration. The shutter can be operated at a repetition rate of 4 Hz for continuous loading of the magnetic trap.

2.2.2 DC glow discharge source

A molecular beam source based on a DC glow discharge was also used for loading atomic N and NH into the magnetic trap. The bulk of the results described in Chapter 3 were taken using this source. The operation of the DC glow discharge source has been described previously in the thesis of Dima Egorov [59]. Figure 2.3(b) shows a schematic of the source. The flow of the process gas, (ammonia or N_2+H_2) is controlled by a solenoid valve[1]. The process gas then flows through a region of high electric field, generated by a pair of tungsten alloy jaws held at 1 KV, where the process gas is dissociated and the radicals are produced. This discharge source is run without a shutter between the source and the trapping region, as we rely on the proper sealing of the solenoid valve to stop flow of the gas into the trapping region. Not having a shutter allows the source to be placed closer to the trapping region, yielding a larger flux of atoms and molecules. The elastomer poppet that seals

[1]Parker Hannefin General valve P/N 9-1646-900

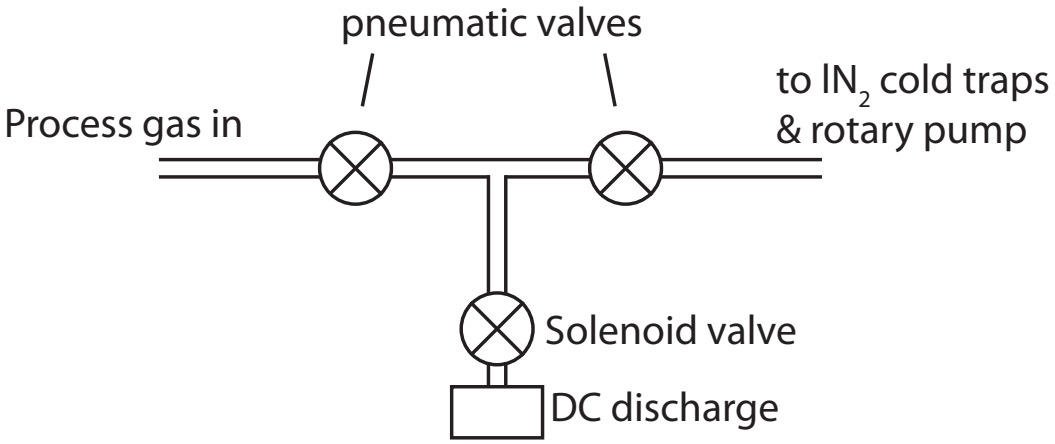

Figure 2.4: Setup for evacuation of DC discharge manifold

against the stainless steel base in the solenoid valve can degrade during operation. It was found after a few days of operation, a leak in the solenoid valve would develop that was large enough to limit trapping lifetimes to a few tens of seconds. Poppets made from both Vespel and Kel-F were tried, but both would lead to failure after a few days of operation. On the one hand, the leaky valve posed a problem for taking trap lifetime measurements of atomic nitrogen. On the other hand, it demonstrates the ability of our apparatus to perform collision experiments between a magnetically trapped sample and an external molecular beam. To solve the problem the leaky valve posed for taking time decays of atomic nitrogen, a simple manifold of valves, shown in Figure 2.4 was setup to allow the manifold behind the solenoid valve to be rapidly evacuated directly after the trap was loaded.

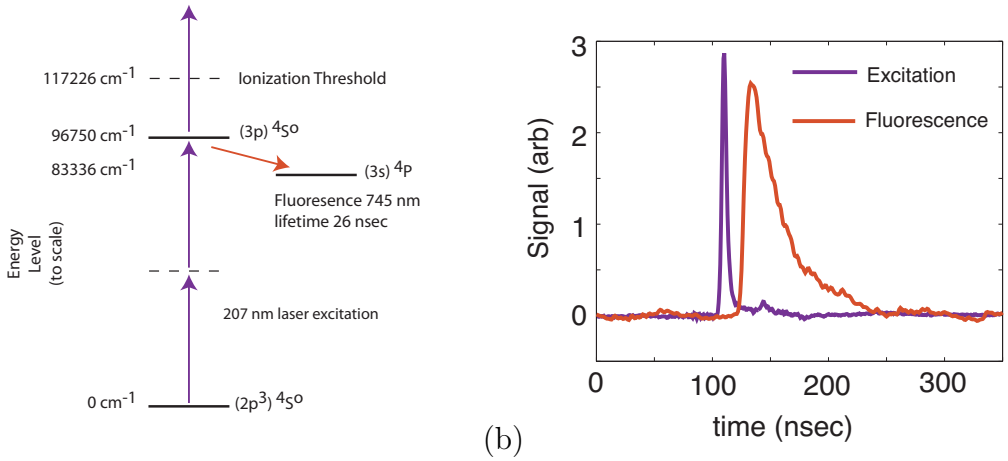

Figure 2.5: Depiction of two-photon absorption laser induced fluorescence in atomic nitrogen. (a) Partial electronic energy level structure for atomic nitrogen. (b) Data showing the excitation pulse and subsequent atomic fluorescence.

2.3 Detection of trapped species

2.3.1 Nitrogen Detection

A challenging aspect of working with atomic nitrogen is the spectroscopic detection. The most accessible electric dipole transition from the ground state of nitrogen is at 120 nm [55], which makes VUV-laser spectroscopy possible [63–65], but technically challenging. A more widely used technique for detection of ground state atomic nitrogen called two-photon absorption laser induced fluorescence (TALIF) [66, 67], is depicted in Figure 2.5(a). It involves pulsed excitation via a two-UV-photon absorption transition followed by detection of infrared (IR) fluorescence. Data showing the excitation pulse and subsequent atomic fluorescence is shown in Figure 2.5(b). A brief overview of the TALIF technique and laser setup for detection of atomic nitrogen is given here. A more detailed analysis of two-photon excitation is reserved for Appendix A.

The level structure for detection of atomic nitrogen using the TALIF technique is shown in Fig. 2.5(a). The two-photon absorption cross-section for excitation from the ground $(2p^3)^4S$ state to the $(3p)^4S$ excited state at 96750 cm^{-1} is small, on the order of 10^{-36} cm^4 [68]. Since the two-photon excitation rate, $W^{(2)}$, scales as the square of the incident laser intensity ($W^{(2)} \sim \sigma^{(2)} I^2$), maximum detection efficiency is typically achieved using focused light from a nanosecond pulsed laser. Pulse energies of 100s of μJs over 10 ns duration focused down to beam diameters on the order of 100 μm provide enough photon flux to efficiently drive the two-photon excitation. After the nitrogen atom undergoes excitation via absorption of two photons of wavelength 206.7 nm, it can decay to the ^4P manifold of states near 83336 cm^{-1}, emitting a photon of wavelength near 745 nm. If the laser intensity is high enough, the nitrogen atom can absorb a third photon, resulting in photo-ionization of the atom. In our case, we collect the fluorescence emitted at 745 nm and detect it using a photomultiplier tube, as shown in Fig. 2.6.

A second possible two-photon transition for detection of atomic nitrogen is via absorption of two photons at 211 nm and excitation to the $(3p)^4D$ near 94883 cm^{-1} (not shown in Fig. 2.5(a)) [66]. One disadvantage to this transition is that the fluorescence is emitted at 869 nm, where PMTs are significantly less sensitive. Also, in the large inhomogeneous magnetic trapping fields, the transition at 211 nm will be broadened due to differential Zeeman shifts of the ground ^4S and excited ^4D states. For the transition at 207 nm, the ground ^4S and excited ^4S states both have Lande g-factors of 2, leading to negligible Zeeman broadening of the transition. For these two reasons, all data taken in this thesis is for the transition at 207 nm.

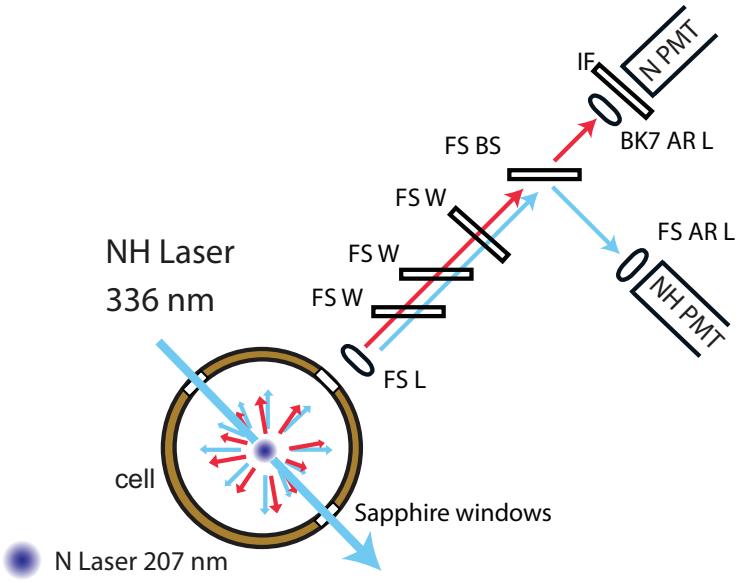

Figure 2.6: Depiction of fluorescence detection. FS W, fused silica window; FS BS, fused silica dichroic beamsplitter, FS L, fused silica lens; IF, interference filter.

In phase I of the experiment, the lens used to focus the excitation laser onto the trapped atomic nitrogen sample was placed inside the trapping cell, 6 cm from the trapped atoms along the axial dimension, as shown in Fig. 2.2(a). This placement was to ensure a focused beam diameter of less than 50 μm. This was a conservative estimate to ensure sufficient laser intensity to saturate the two-photon transition. As it turns out, the high intensities from the tightly focused laser beam also likely produced a fair amount of photoionization of the atomic nitrogen. In principle, one could use this resonantly enhance multi-photon ionization (REMPI) technique for detection of the trapped atomic nitrogen, although due to the large laser intensities and destructive nature of the technique, its advantages are not immediately clear. In the second phase of the experiment, the lens was placed about 100 cm from the atoms, yielding a focused beam diameter on the order of 250 μm. This placement was advantageous as it was outside the vacuum chamber, allowing for adjustments of

the laser beam focus during the experiment, yet still provided tight enough focusing for efficient two-photon excitation.

As described above, the focusing lens is placed along the axial dimension of the magnetic trap. In the future, moving the excitation laser for nitrogen to enter from the side of the cell would allow greater optical and mechanical access along the axis of the magnet, which, for example, would aid in fluorescence imaging of the trapped atoms. The side port cell windows through which the NH detection laser enters, Fig. 2.6, are made of sapphire. This choice of material allows for the cell windows to be thin, thermally conductive, and transparent at 336 nm, the detection wavelength of NH. Thicker windows would take up more space in the trapping region and reduce the overall trap depth. This design choice was made before we were considering trapping atomic nitrogen in this apparatus, as sapphire is not sufficiently transparent at 207 nm. A 1 mm thick window of sapphire transmits only 35% of the light at 207 nm, which would lead to reduced nitrogen detection sensitivity, as well as possible heating of the cell windows. A new buffer gas cell incorporating MgF_2 or CaF_2 cell windows (or perhaps even no windows at all) would allow the nitrogen laser to enter from the side of the cell.

On a more general note, Table 2.1 shows the transmission of various materials at 207 nm. While UV grade fused silica transmits well at 207 nm, we have found the not all manufacturers' regular grade fused silica and crystalline quartz provide sufficient transmission. Transmission at 207 nm is particularly sensitive to impurities in the fused silica. As a result, we individually test each optic for transmission at 207 nm before incorporating it into the experiment, especially for elements that reside inside

Table 2.1: Measured transmission of materials at 207 nm. Values are rounded to the nearest 5% and are for uncoated optics and include surface reflections.

part number	material	transmission
CVI PW-1010-CQ	crystalline quartz	0.70
CVI PW1-1525-UV	fused silica	0.50
Optosigma 045-0395	UV grade fused silica	0.90
MDC KF 450028	fused silica	0.90
Edmund Optics TechSpec	UV fused silica	0.90
Edmund Optics	1mm sapphire	0.35
CVI[a]	MgF_2, CaF_2	0.90

[a] Specified by manufacturer.

the vacuum chamber.

Figure 2.7 shows the schematic for production of laser radiation at 207 nm. A pulsed dye laser using Rhodamine 640 laser dye produces about 45 mJ of light at 620 nm. The 620 nm light is frequency doubled in a non-linear KDP crystal using type-I phase matching to produce about 10 mJ of light at 310 nm. The polarization of the resulting 310 nm light is orthogonal to the 620 nm light. For efficient generation of 210 nm light using type-I phase matching in a non-linear β-BBO crystal, the polarization of 310 nm and 620 nm light must be parallel. This is achieved by separating the light using a dichroic beam splitter and rotating the polarization of the 310 nm using a half waveplate and then recombining the light before the nonlinear β-BBO crystal using a second dichroic beam splitter. The resulting 2 mJ of light at 207 nm is separated from the fundamental beams by using a pair of dispersive Pellin-Broca prisms. In order to maintain stable operation of the laser during the experiment, the pulsed dye laser is run continuously at its operating repetition rate of 10 Hz. This is necessary as neither the dye laser cavity nor the β-BBO crystal are temperature stabilized. A mechanical shutter is used to selectively send laser pulses to the apparatus

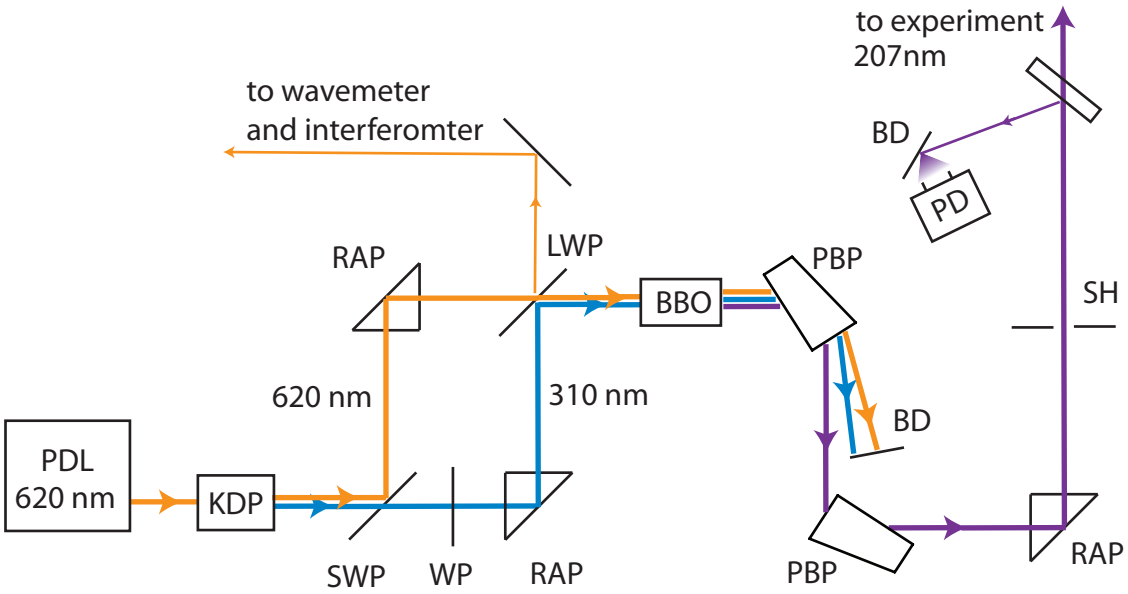

Figure 2.7: 207 nm pulsed dye laser (PDL) setup. KDP; 1st stage doubling crystal; SWP, short wave pass beam splitter; WP, 1/2 wave plate; RAP, right angle prism; LWP, long wave pass beam splitter; BBO, second state sum-frequency mixing crystal; PBP, Pellin-Broca Prism; BD, beam dump, SH, shutter; PD, photodiode.

for nitrogen detection. The pulse energy of each pulse is monitored by picking off a fraction of the 207 nm beam and directing it onto an alumina beam dump. A fast photodiode then monitors the scattered light from the beam dump. The frequency of the laser is monitored by sending a portion of the 620 nm fundamental to be analyzed using a Coherent Wavemaster wavemeter. The 207 nm light is sent to the trapping apparatus using a series of prisms and mirrors. Before being focused onto the atoms, the laser beam is expanded and collimated using a pair of lenses in the Galilean telescope configuration. The expansion of the beam before the final focusing lens allows for a tighter focus to be achieved at the position of the atoms.

2.3.2 NH detection

Detection of NH is performed using laser induced fluorescence (LIF) excited on the $|A^3\Pi_2, \nu' = 0, N' = 1\rangle \leftarrow |X^3\Sigma^-, \nu'' = 0, N'' = 0\rangle$ transition. The NH fluorescence is collected by the same lens that collects ^{14}N fluorescence and, using a dichroic mirror, is sent to a separate PMT for detection. The NH fluorescence that is detected by the PMT is at the same wavelength as the excitation laser used to excite the NH molecules. With continuous illumination of the molecules, the dominant source of noise on the NH fluorescence signal is light scattered out of the laser beam, presumable by the cell windows and frozen ice on them. To increase our signal to noise, we modulate the NH laser beam at 1 MHz using an acousto-optic modulator (AOM). The 1st order diffraction of the laser beam after the AOM is sent to the experiment, while the 0th order beam is blocked using an iris. This technique can provide extinction ratios of 1/200 with turn-off times of approximately 100 ns. The lifetime of the excited state of NH is 440 ns [60]. By observing the fluorescence only after the NH laser has been extinguished, we can achieve an increase in our signal to noise of approximately 50 using this technique. To gate the collection of the signal from the NH PMT we use a switch[2] after the current preamplifier. We trigger the switch using a delay generator triggered off the AOM modulation signal. With this method the dominant noise on our NH LIF fluorescence signal is still limited by background scatter from the excitation laser, as the extinction from the AOM is not perfect during the 500 ns window following excitation. This imperfect extinction is due to the finite response time (limited bandwidth) of the crystal in the AOM itself. The DC extinction ratio

[2]MiniCircuits ZYSWA-2-50DR-B

of the AOM—i.e. the extinction ratio measured at long times after the initial turn off—is significantly better, on the order of 10^{-3}. To achieve faster turn off times an AOM with a larger bandwidth could be used; this corresponds to an AOM with a larger center frequency. The current AOM has a center frequency of 125 MHz. While AOMs for use at frequencies in the visible spectrum can have center frequencies as high as 1 GHz yielding extinction times on the order of a 3 ns [69], AOMs for use at ultraviolet frequencies use fused silica crystals that suffer from decreased diffraction efficiencies for center frequencies larger than 200 MHz. Use of a second AOM with center frequency 200 MHz in series with the current AOM may result in improved signal to noise detection from LIF of NH.

2.3.3 Chromium

For certain measurements we use atomic chromium as a diagnostic tool, as trapping of atomic chromium has been previously studied in several experiments in our lab [70–72]. Atomic chromium is produced via laser ablation of a solid elemental target that has been epoxied to the buffer gas cell near the molecular beam entrance. We detect trapped atomic chromium on the $|^7\mathrm{S}_3, m_j = +3\rangle \rightarrow |^7\mathrm{P}_4\rangle$ transition at 425 nm using light from a frequency doubled Ti:Sapph laser. Absorprtion spectroscopy on this transition provides temperature and density information about the trapped chromium. Additionally, laser induced fluorescence on this transition can be performed at the same time using the collection optics for atomic nitrogen detection.

2.4 Trap Loading and Measurement

In this section we describe the actual process by which we load the magnetic trap and measure the trapped atomic and molecular density profiles in time. The sequence is as follows, with times referenced to the initial molecular beam firing at $t = 0$.

$t = -8$ s: Fluorescence collection for NH is begun before any species are loaded into the trap to provide data for background subtraction.

$t = -0.05$ s: Cryogenic buffer gas reservoir pulsed valve is actuated (open time $<$ 20 ms), to fill trapping cell with buffer gas.

$t = 0.0$ s: Molecular beam is actuated (open time $\sim$ 40 ms), sending atoms and molecules into the trapping region.

$t = 0.5$ s: If data is being taken at an elevated cell temperature, heat is applied to the cell using a resistive heater.

$t = t_N$: A mechanical shutter opens for 0.35 s, allowing three pulses of 207 nm excitation light into the apparatus for nitrogen detection. The atomic fluorescence for each pulse is recorded and averaged using an oscilloscope. The pulse energy time profile is also recorded for each laser pulse using the fast photodiode and averaged on the oscilloscope.

To acquire a complete time trace for an atomic nitrogen decay, the entire loading process is repeated for a different value of t_N, with times ranging between 0.5 s and 120 s. A separate loading sequence for each value of t_N is necessary, as we find repeatedly firing the 207 nm laser causes loss of nitrogen atoms (and NH). Figure

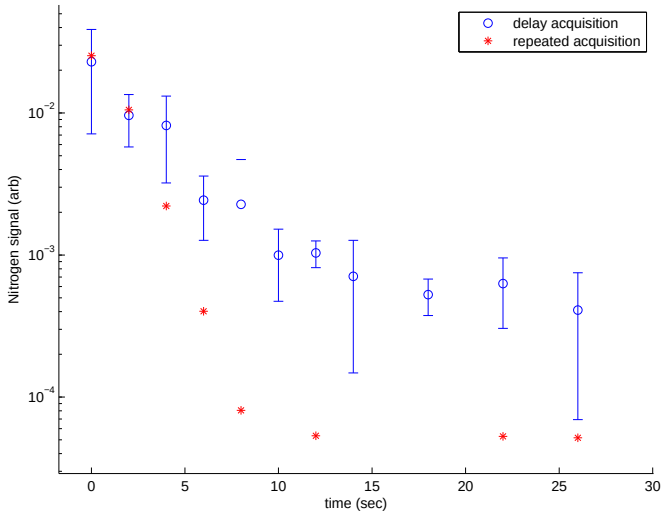

Figure 2.8: Repeated 207 nm acquisition.

2.8 shows a comparison of nitrogen trap decay taken two different ways. The trace shown with circles is taken using the delayed firing method described above. The trace shown with stars is taken with repeated firing of the 207 nm laser during each loading sequence. This latter method clearly shows loss of nitrogen atoms due to the additional firing of the 207 nm laser. To take a full time trace of atomic nitrogen, multiple points (typically just 2 or 3) at each delay time are taken to average shot-to-shot fluctuations. Additional data points are taken where no atoms or molecules are loaded into the trap to provide data for background subtraction for the nitrogen signal. The final points in the nitrogen time trace represent the integrated nitrogen fluorescence after background subtraction and normalization from dividing by the square of the measured pulse energy. Figure 2.9 shows the logarithm of the nitrogen signal plotted as a function the logarithm of the measured pulse energy. A fit to the form $y = ax + b$, with the value of $a = 1.99(15)$ confirms the dependance of the

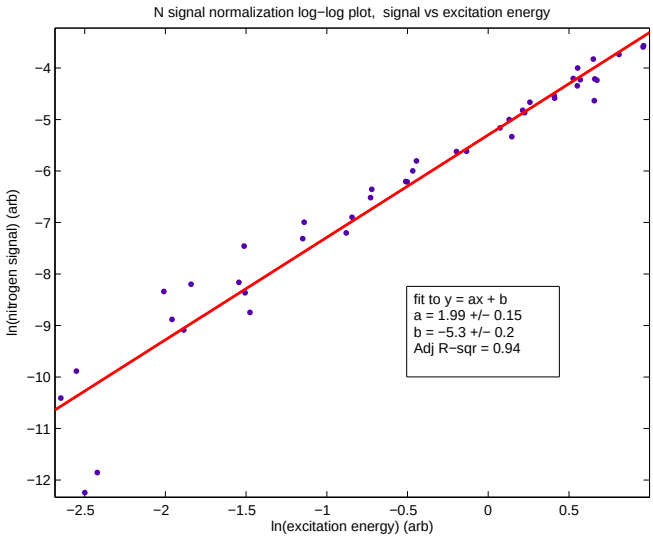

Figure 2.9: Nitrogen signal normalization.

nitrogen signal on the square of the pulse energy.

Since each acquisition takes about 3 min, the total acquisition time for a single nitrogen decay is a bit over one hour. Due to the long acquisition time, cell temperatures and buffer gas and process gas pressures are monitored and held as constant as possible. The delay time t_N is varied in a double zig-zag pattern in order to minimize the effects of linear drifts on the measurements. The ^{3}He refrigerator used to cool the buffer gas trapping cell has a single-shot run time of about 8 hr, which allows for the acquisition of about five nitrogen times traces per day.

Chapter 3

Results and analysis

In this Chapter we present the results of the first magnetic trapping of atomic nitrogen. We obtain observation times of longer than 1 minute. From our observations of trap loss of the atomic nitrogen, combined with quantum scattering calculations performed by Timur Tscherbul we estimate we trap about 1×10^{12} N atoms at densities of 2×10^{12} at a temperature of 600mK.

We also demonstrate cotrapping of atomic nitrogen with molecular NH. Using the pulsed valve buffer gas loading technique we are able to lower the background He density low enough to observe the effects of N-NH collisions in our magnetic trap. From observation of the NH trap loss rate, and comparison with Tscherbul's quantum scattering calculations we are able to measure a value of the ratio of elastic to inelastic N-NH collisions of $\gamma_{\mathrm{N-NH}} \approx 100$ at a temperature of about 550 mK. This large value of γ demonstrates the utility of atomic nitrogen as a collision partner for sympathetically cooling magnetically trapped molecules.

3.1 Trap Dynamics

An understanding of the dynamics of the atoms and molecules in the magnetic trap is necessary to extract measurements of the fundamental collision processes. The elastic and inelastic collisions between atoms, molecules, and the buffer gas all play a role in the thermalization and trap loss. Here we will develop a model to include all of these in order to interpret our data.

The role of collisions in magnetic traps has been treated in the past in the literature[73, 74], as well as in several theses from our group [70, 72, 75]. Here we will review the results and apply them to our system.

3.1.1 Trapped atom density distribution

For the experiments described in this thesis, we will discuss the dynamics of the atoms in the trap in the large η limit, where η is defined as the ratio of the trap depth to the atom temperature, $\eta = U_{\rm trap}/kT$. Taking this limit allows for certain simplifications. In particular, one can describe the density distribution as

$$n(\mathbf{r}) = n_0 \exp[-U(\mathbf{r})/k_{\rm B}T] \tag{3.1}$$

where n_0 is the density at the center of the trap, $U(\mathbf{r})$ is the potential energy of the atoms in the trap at position $\mathbf{r}$, and T is the temperature of the trapped atoms. For our magnetic trap, for the discussion here we will approximate the trapping potential as a spherical quadrupole field:

$$U(r,z) = U_{\rm trap}(r^2 + 4z^2)^{1/2}/R \tag{3.2}$$

where R is the position of the edge of the trap, defined by the cell wall, and U_{trap} is the depth at the edge of the trap. The actual magnetic trap does not have quite as tight confinement in the z-direction as equation 3.2. Evaluation of the expressions derived in the section done numerically for the real potential surface leads to slight numerical differences in the results. These differences will be noted as we proceed in this section.

To calculate the total number of atoms in the trap, given a peak density, one can integrate the density distribution over the volume of the trap:

$$N = \int^{V} n_0 \exp[-\eta(r^2 + 4z^2)^{1/2}/R] d^3r \tag{3.3}$$

$$\approx n_0 \left\{ \frac{4\pi R^3}{\eta^3} \right\} \tag{3.4}$$

where equation 3.4 is the expression in the large η limit. Here the edge of the trap is defined as the ellipsoid with radii R and $R/2$ along the r and z axis, respectively. We will define the term in braces in equation 3.4 the effective volume of the trap, $V_{\text{eff}} \equiv \frac{4\pi R^3}{\eta^3}$, as the product of it with the peak trap density gives the total number of atoms in the trap, $N = n_0 V_{\text{eff}}$. For the real trapping field the effective volume is about a factor of 2 larger, $V_{\text{eff}}^{(\text{real})} = 7.6\pi R^3/\eta^3$.

3.1.2 Inelastic collision trap loss

We will now consider the trap loss rate due to inelastic atom-atom collisions. For a particular outgoing collision channel (i), the atom-atom collision event rate $\Gamma^{(i)}$ is given by

$$\Gamma^{(i)} = k_{\text{in}}^{(i)} n \tag{3.5}$$

where $k_{\text{in}}^{(i)}$ is the rate coefficient in cm^3s^{-1} for outgoing collision channel (i). For a given inelastic collision, either one or both of the atoms can change their internal Zeeman state, which will typically lead to loss from the magnetic trap of either one or both of the atoms , respectively. Hence, the total inelastic loss rate due to atom-atom collisions can be represented as a sum over the set of all possible outgoing collision channels:

$$\Gamma_{\text{loss}} = \sum_i g_i k_{\text{in}}^{(i)} n \tag{3.6}$$

$$k_{\text{loss}} = \sum_i g_i k_{\text{in}}^{(i)} \tag{3.7}$$

where g_i is the number of atoms loss from the magnetic trap for collision channel (i). If the atoms began in a distribution of initial states, then equation 3.6 would also include a sum over initial states as well. For our trapping conditions, we assume all atoms are in a single state, the stretched Zeeman state $|J, m_J = J\rangle$, so equation 3.6 is sufficient.

The total atom trap loss rate due to inelastic collisions can be expressed as an integral over the trap volume of the local inelastic collision rate in the trap:

$$\dot{N} = -\int^V k_{\text{loss}} n^2 d^3r \tag{3.8}$$

$$= -n_0^2 \int^V k_{\text{loss}} (\exp[-U(\mathbf{r})/k_{\text{B}}T])^2 d^3r \tag{3.9}$$

In general, k_{loss} will depend on position in the trap. For example, the inelastic rate typically has a collision energy (temperature) and magnetic field dependance. If the atoms remain at a constant temperature, then the distribution of atoms in the trap

remain unchanged over time, and we have $\dot{N} = \dot{n}_0 V_{\text{eff}}$. This leads to the expression

$$\dot{n}_0 = -n_0^2 \frac{1}{V_{eff}} \int^V k_{\text{loss}} (\exp[-U(\mathbf{r})/k_{\text{B}}T])^2 d^3r \tag{3.10}$$

$$= -\left\langle k_{\text{loss}} \right\rangle n_0^2 \tag{3.11}$$

where $\left\langle k_{\text{loss}} \right\rangle$ represents the trap averaged inelastic loss rate constant for atom-atom inelastic collisions.

For the case where k_{loss} is independent of position in trap, the integral in equation 3.8 yields

$$\dot{N} = -k_{\text{in}} n_0^2 \left\{ \frac{\pi R^3}{2\eta^3} \right\} \tag{3.12}$$

The term in braces we will term the collision volume, $V_{\text{coll}} = \pi R^3 / 2\eta^3$. For integration over the real trapping field, $V_{\text{coll}}^{(\text{real})} = 1.0(\pi R^3/\eta^3)$. We can then write an expression for the evolution of the peak density of atoms in the trap,

$$\dot{n}_0 = -\frac{V_{\text{coll}}}{V_{\text{eff}}} k_{\text{loss}} n_0^2 \tag{3.13}$$

$$= -\frac{1}{8} k_{\text{loss}} n_0^2 \tag{3.14}$$

From this we see that, for the case where k_{loss} is independent of trap position, $\left\langle k_{\text{loss}} \right\rangle = (1/8) k_{\text{loss}}$, where the observed inelastic loss rate is a factor of 8 smaller due to the averaging the collision rates over the varying atomic density in the trap.

Before moving on, we will stop to consider a few specifics of inelastic loss for atomic nitrogen in our magnetic trap. When two nitrogen atoms collide in the magnetic trap, they both begin in the $|S = 3/2; m_s = 3/2\rangle$ state. For an inelastic collision, the final internal state of each atom can be any of the four available Zeeman states $m_s = \pm(3/2, 1/2)$. Calculations of dipolar relaxation in N-N collisions by Timur

Tscherbul, presented later in Section 3.2, show that the dominant exit channels are $|3/2;1/2\rangle\,|3/2;3/2\rangle$ and $|3/2,1/2\rangle\,|3/2;1/2\rangle$. In the first case, only one atom changes its spin projection, in the second case both atoms change their spin projection. In addition to the change in spin projection, the internal energy associated with the change in Zeeman state is released into kinetic energy of the colliding partners, $\Delta E = 2\mu_{\rm B}B$. For collisions at low magnetic field (< 0.4 T), this corresponds to an energy change of $k_{\rm B}0.5$ K. The trap depth for an atom in the $|3/2;1/2\rangle$ state is about 2.6 K. Hence, it is likely that atoms in the $|3/2;1/2\rangle$ state will have to undergo further collisions (about 10) before they exit the trap. Nevertheless, for the same total number of atoms, the density of atoms at the center of the trap in the $|3/2;1/2\rangle$ will be a factor of 27 lower due to decreased confinement, so they will not contribute to a significant fraction of the observed fluorescence signal. Spin exchange collisions between two nitrogen atoms in the $|3/2;1/2\rangle$ should proceed rapidly, so it is unlikely that any significant population in the state would persist in the trap. For these reasons, in our analysis we assume that atoms in the $|3/2;1/2\rangle$ state are immediately lost from the trap.

3.1.3 Evaporative loss

Inelastic atom-atom collisions are not the only source of atom loss from our magnetic trap. Two atoms may collide elastically, exchange energy, and promote one of the atoms to sufficiently high energy to leave the trap. This process is termed evaporation, and we now consider the dynamics of this process in our magnetic trap.

Again, we can express the total trap loss rate due to evaporation as an integral

over the trap volume of the local evaporation loss rate,

$$\dot{N} = -\int^{V} k_{\text{evap}} n^2 d^3 r \tag{3.15}$$

In this case, k_{evap} depends on position in the trap, and some fraction of elastic collisions will result in the evaporation of atoms from the trap. Using an argument[1] described by Ketterle in Ref. [73], the local atom loss rate in an arbitrary trap due to evaporation can be expressed as

$$\dot{n}(r) = -\sigma_{\text{el}} \bar{v} \eta_{\text{eff}} e^{-\eta_{\text{eff}}} n_0^2(r) \tag{3.16}$$

where, σ_{el} is the elastic collision cross-section, $\bar{v}$ is the mean thermal velocity, and $\eta_{\text{eff}} = \eta - U(r)/kT$ is the local effective "η." Integrating equation 3.16 over the trap volume, and rewriting the result in terms of peak trap density yields

$$\dot{n}_0 = -\left(\frac{V_{\text{coll}}}{V_{\text{eff}}}\right) \sigma_{\text{el}} \bar{v}_{\text{rel}} f(\eta) n_0^2 \tag{3.17}$$

$$= -\left(\frac{1}{8}\right) k_{\text{el}} f(\eta) n_0^2(r) \tag{3.18}$$

where $f(\eta)$ can be interpreted as the fraction of elastic collisions leading to evaporation at a given trap depth η, and can be expressed as

$$f(\eta) = 2\sqrt{2}[e^{-\eta}(2\eta - 6) + e^{-2\eta}(6 + 4\eta + \eta^2)] \tag{3.19}$$

$$\approx 4\sqrt{2} e^{-\eta}(\eta - 3) \tag{3.20}$$

We see that as the trap depth, η is increased, the atom loss rate due to evaporation is suppressed exponentially. Combining equations 3.11 and 3.18 to obtain the trap

[1]This argument is based on the principle of detailed balance. For a sample to remain in steady state distribution, the rate at which atoms are promoted to high energies must be the same as the rate for those high energy atoms to be promoted to lower energies.

dynamics due to combined elastic and inelastic atom-atom collisions yields

$$\dot{n}_0 = -(\langle k_{\text{evap}} \rangle + \langle k_{\text{loss}} \rangle) n_0^2 \tag{3.21}$$

$$= -\langle k_{\text{2b}} \rangle n_0^2 \tag{3.22}$$

where, $\langle k_{\text{evap}} \rangle = \frac{k_{\text{el}}}{8} f(\eta)$, and we term $\langle k_{\text{2b}} \rangle$ the two-body loss rate constant (loss due to atom-atom collisions). The two-body loss rate constant is the value which we observe in our experiments.

3.1.4 Discussion of two-body loss

Recall the figure of merit for evaporative cooling of a magnetically trapped species is the ratio of elastic collision rate to inelastic collision rate, $\gamma = k_{\text{el}}/k_{\text{loss}}$. As a rule of thumb, γ should be larger than 100 for efficient evaporative cooling. Inspecting equation 3.21, we see that we can write the two-body loss rate constant as

$$\langle k_{\text{2b}} \rangle = \frac{k_{\text{el}}}{8}(f(\eta) + \frac{1}{\gamma}) \tag{3.23}$$

We see that, in principle, by measuring the two-body loss of atoms in our trap at several different trap depths, η, we can extract a value for γ. This measurement of γ can be performed without knowing the absolute density of atomic nitrogen in our trap. This is important, since calibrating the absolute amount of atomic nitrogen in our trap is difficult using the TALIF detection technique.

3.1.5 Background gas collisions

An additional complication to the interpretation of atom loss from our magnetic trap comes from the presence of collisions with background helium gas. Loss from

background gas collisions[2] has the form

$$\dot{n}_0 = -(k_{\mathrm{He-el}} f_{\mathrm{He}}(\eta) + k_{\mathrm{He-in}}) n_{\mathrm{He}} n_0 \tag{3.24}$$

$$= -k_{\mathrm{He}} f_{\mathrm{He}}(\eta) n_{\mathrm{He}} n_0 \tag{3.25}$$

where k_{He} is the atom-He elastic collision rate constant, $f_{\mathrm{He}}(\eta)$ the fraction of atom-He collisions the lead to an atom evaporating over the trap edge, and n_{He} is the helium density. We have ignored loss due to inelastic collisions with He, as it is typically 10^8 times smaller than the elastic collision rate for collisions with S-state atoms [76]. In reference [75], Brahms evaluates an expression for $f_{\mathrm{He}}(\eta)$ numerically and shows it to be roughly of the form

$$f_{\mathrm{He}}(\eta) = \left(\frac{1}{2}\eta^{3/2} + \frac{1}{4}\eta^{5/2}\right) e^{-\eta} \tag{3.26}$$

and thus an additional term is needed to describe the trap dynamics:

$$\dot{n}_0 = -(\langle k_{\mathrm{evap}} \rangle + \langle k_{\mathrm{loss}} \rangle) n_0^2 - n_{\mathrm{He}} k_{\mathrm{He}} f_{\mathrm{He}}(\eta) n_0 \tag{3.27}$$

$$\dot{n}_0 = -\langle k_{\mathrm{2b}} \rangle n_0^2 - \frac{1}{\tau} n_0 \tag{3.28}$$

When the trap is initially loaded, and the bulk of the buffer gas pumped out of the trapping region, the trap loss is dominated by 2-body collisions. At later times, when the atom density had decreased due to evaporation, the 1-body collision term dominates. Solutions to equation 3.28 are given in Table 3.1. The experimental trap decays are typically fit to one of these forms.

[2]We are in the long mean free path regime $(\sigma_{\mathrm{He}} n_{\mathrm{He}})^{-1} \gg$ cell dimensions.

Name	equation, $\dot{n}_0 =$	solution, $n_0(t) =$
1 body	$-\frac{1}{\tau}n_0$	$n_0(0)e^{-t/\tau}$
2 body	$-\langle k_{2b}\rangle n_0^2$	$n_0(0)\cdot(1+\langle k_{2b}\rangle n_0(0)\cdot t)^{-1}$
(1+2) body	$-\langle k_{2b}\rangle n_0^2-\frac{1}{\tau}n_0$	$n_0(0)\cdot\big(\exp[t/\tau]+\tau\langle k_{2b}\rangle n_0(0)(\exp[t/\tau]-1)\big)^{-1}$

Table 3.1: Solutions to trap loss rate equations.

3.1.6 Assumptions in trap dynamics calculations

Let us review the assumptions that we have made in the preceding analysis of trap loss dynamics.

The first assumption was the edge of the trap was defined by an equi-potential ellipsoid, and that any atom with $U > U_{\rm trap}$ is removed from the trap. In our actual trapping geometry, the edge of the trap is defined by the buffer gas cell wall, and atoms leave the trap for $R > R_{\rm cell}$. As a result, atoms can have orbits in the magnetic trap with $U > U_{\rm trap}$ but who's trajectories do not cross the cell wall. The main result of this assumption is that in the real trap, a smaller fraction of atom-atom collisions will lead to evaporation, $f^{(\rm real)}(\eta) < f(\eta)$.

The second assumption we have made is the temperature of the trapped sample stays at a constant temperature throughout the observed time decay. In the limit where collisions with the buffer gas dominate, this is certainly true, as the buffer gas pins the atom temperature to the cell wall temperature. When collisions with the buffer gas are absent, the trapped atoms reach a thermal equilibrium when the cooling due to evaporation balances the heating due to inelastic collisions When the

buffer gas collision rate is similar to the atom-atom evaporation rate, it is possible to enter an intermediate regime, where cooling from evaporation may work to balance heating from collisions with the buffer gas, and the resulting equilibrium temperature may be sensitive the relative atom-helium densities.

To investigate these two assumptions in more detail, we performed a molecular dynamics Monte-Carlo simulation. The details of the simulation are described in Appendix C. Briefly, it simulates the trajectories of and collisions between trapped atoms and helium buffer gas for the geometry and conditions of our experiment. The two essential results are that for the buffer gas and trapped atom densities of our experiment we can: (1) assume the temperature of the trapped atoms is pinned to the temperature of the cell wall via collisions with the buffer gas, and (2) the fraction of atom-atom collision that lead to evaporation is approximately $f^{(\mathrm{real})}(\eta) \approx (1/3)f(\eta)$.

3.2 N-N collisions

Figure 3.2 shows a time decay of nitrogen with combined (1+2) body fit. Over the course of two days, we take data at two different cell temperatures ($\sim$ 610 mK and 640 mK), and at five different magnetic trap depths between 3.3 and 3.9 T. This magnetic field range represents, at the high end, the maximum design field of the magnet. At the low end, the reduced confinement of the trap leads to lower nitrogen densities, and 1-body loss from He becomes the dominant contribution to the observed nitrogen loss rate.

Figure 3.3 summarizes the results of the observed nitrogen two-body loss rate vs η. The solid lines in the plot show best fits of the data, for a fixed value of γ, to the

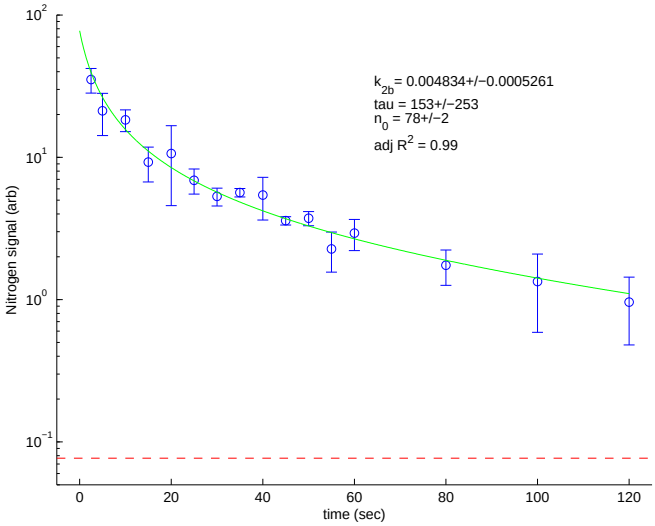

Figure 3.1: A superb nitrogen time decay. The solid lines shows a fit to a combined (1+2) body decay. The dashed line shows the typical level of background noise. Taken at a trap depth of 3.8 T. The cell cools from 650 mK to 550 mK over approximately a 10 sec time scale.

expression derived in section 3.1.4

$$\langle k_{2b} \rangle = \frac{k_{el}}{8}(f(\eta) + \frac{1}{\gamma}) \tag{3.29}$$

For very small γ, inelastic collisions dominate at all trap depths, and $\langle k_{2b} \rangle$ is a flat line independent of η. For very large η, evaporative collisions dominate, and $\log_{10}[\langle k_{2b} \rangle]$ varies linearly with η, with a maximum slope of magnitude $\log_{10}[e] = 0.4$, close to the value shown in Figure 3.3 for a $\gamma = 3 \times 10^4$. The data shown here for atomic nitrogen does not discriminate will between a very large γ or a very small γ, due to the large uncertainties in the measured values of $\langle k_{2b} \rangle$ and the relative narrow range of η over which data could be acquired.

Instead let us consider the absolute magnitude of $\langle k_{2b} \rangle$. For temperatures cor-

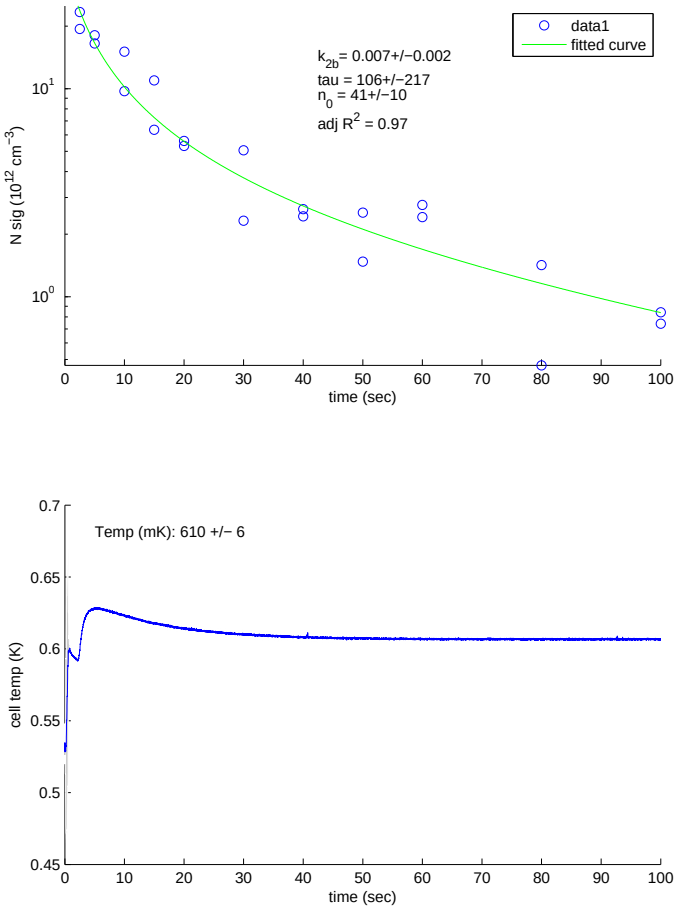

Figure 3.2: Nitrogen time decay at constant cell temperature. Taken at an $\eta = 11.7$.

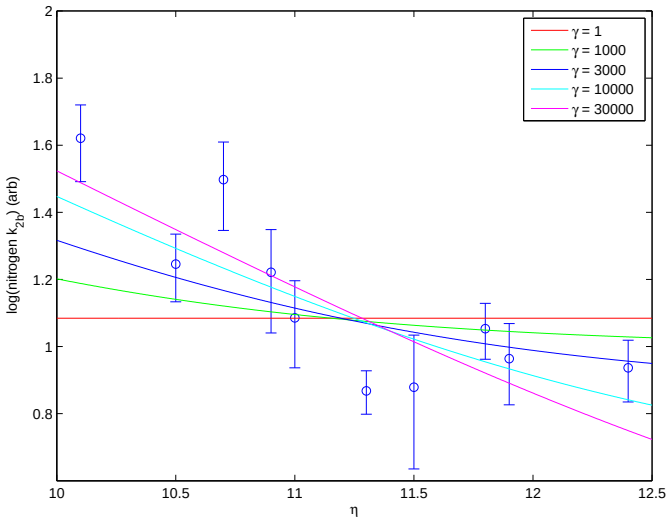

Figure 3.3: Nitrogen k_{2b} versus η. Note that the $\log_{10}[k_{2b}]$ is the quantity actually shown, due to the exponential dependance of k_{2b} on η.

responding to an $\eta > 11$, the fraction of elastic collisions that lead to trap loss is suppressed by a faction $f(\eta > 11)^{-1} > 3 \times 10^4$ according to the Monte-Carlo simulations. Hence, for $\eta > 11$ we would expect $\langle k_{2b} \rangle$ to be dominated by inelastic loss. To extract an absolute value for $\langle k_{2b} \rangle$ from a single nitrogen time decay, we need to be able to calibrate our nitrogen TALIF signal to give absolute nitrogen trap densities. A discussion of the estimate for this calibration is given in Appendix A. Despite significant effort to achieve a reliable calibration, their still remain large overall uncertainties in the TALIF signal calibration. The first is simply an uncertainty of about a factor of 3 from the collection efficiency of the lens system. An additional factor of (at least) 3 comes from uncertainty in the excitation probability, dominated mostly by the spectral properties of the pulsed laser used for excitation. Taking values[3] from the middle of each of these uncertainty ranges gives the calibrated nitrogen time decay

[3]A collection efficiency of 10^{-4} and an effective linewidth $\Delta_{(2)} = 2\pi \times 10 \times 10^9$ rad/s

shown in Figure 3.2. The (1+2) body fit to the time decay yields a measured 2-body loss rate constant of $\langle k_{2b} \rangle = 7(2) \times 10^{-15}$ cm^{3}s^{-1}.

For comparison, we show the trap averaged 2-body loss rate constant predicted by the scattering calculations of Timur Tscherbul in Figure 3.4. The scattering calculations yield inelastic rate constants as a function of magnetic field and temperature for individual outgoing collision channels. The two dominant outgoing channels from the calculations are the $|3/2; 3/2\rangle\,|3/2; 1/2\rangle$, where only one of the atom changes its state, and $|3/2; 1/2\rangle\,|3/2; 1/2\rangle$, where both atoms changer their state. The trap average inelastic loss rate constant, $\langle k^{(i)}_{\rm loss} \rangle$ is calculated for each channel and then summed with the appropriate weighting factor to give the total trap averaged 2-body loss rate constant $\langle k_{2b} \rangle$, as described in Section 3.1.2. At a temperature of 600 mK the loss rate from the scattering calculations has a value $\langle k_{2b} \rangle_{\rm th} = 8.5 \times 10^{-14}$ cm^{3}s^{-1}, and order of magnitude larger than the measured value. One source of uncertainty for the value of $\langle k_{2b} \rangle_{\rm th}$ is the accuracy of the N-N interaction potential used for the scattering calculations. The potential surface is believed to be good about 5%[4]. Scattering calculations using the interaction potential rescaled by a factor of 1.05 yield values for $\langle k_{2b} \rangle_{\rm th}$ similarly scale up by a factor of 1.05. This leads us to believe that the main source of discrepancy between the measured and theoretical value of $\langle k_{2b} \rangle$ is the calibration of the atomic nitrogen density. Scaling the measured nitrogen density down by a factor of 10 would bring the two values for $\langle k_{2b} \rangle$ into agreement. This correction, while large, is still within our uncertainty for the nitrogen density calibration. Using the theoretical value of $\langle k_{2b} \rangle$ to calibrate our nitrogen density gives values of

[4]Timur Tscherbul, private comm.

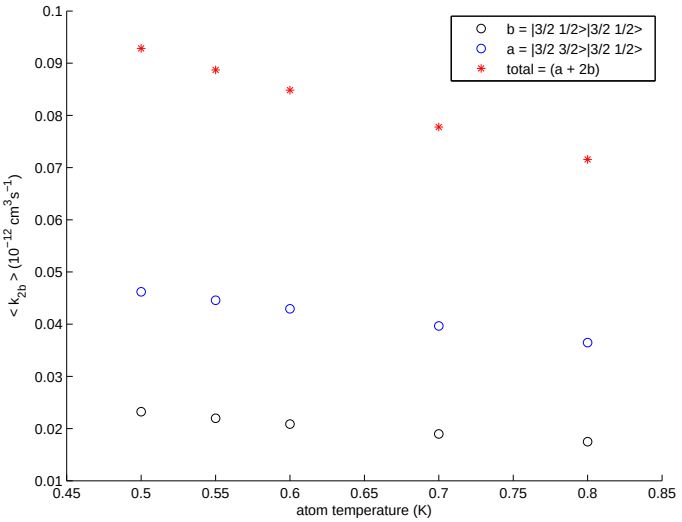

Figure 3.4: Trap average inelastic loss rates from quantum scattering calculations by Timur Tscherbul.

the peak nitrogen density in the trap of $n_0 = 2 \times 10^{12}$ cm^{-3}, which corresponds to $N = 1 \times 10^{12}$ total trapped nitrogen atoms.

3.2.1 Trapping of ^{15}N

We note that we also have observed trapping of the bosonic isotope of nitrogen, ^{15}N. At temperatures of 0.5 K no significant difference in the collision properties due to quantum statistics is expected between the fermionic and bosonic species of nitrogen. In the future, for evaporative cooling of nitrogen to ultracold temperatues, the bosonic species will be needed. Figure 3.5 shows the observed TALIF spectrum and time decay for ^{15}N in the magnetic trap. The data shown in this time decay suffers additional loss due to collisions from the process gas that has leaked through the solenoid valve in the molecular beam source. Due to the limited quantities of $^{15}N_2$

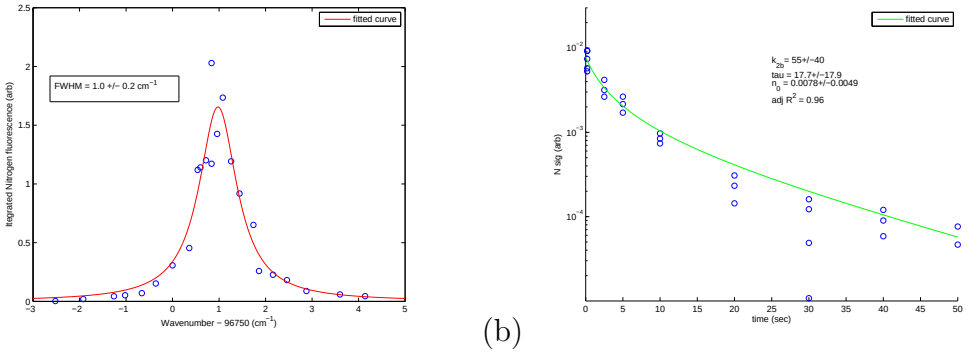

(a) (b)

Figure 3.5: N-15 trapping data.

process gas we had on hand and the overall level of signal-to-noise in typical nitrogen time traces, we did not attempt to pursue a quantitative comparison between ^{15}N and ^{14}N trap loss rates.

3.3 N-NH collsions

By using a mixture of N_2 and H_2 as the process gas for our molecular beam source, we can produce atomic nitrogen and NH in the same beam, and co-load them into the magentic trap. From previous measurements, we estimate that we have peak atomic nitrogen densities on the order of 10^{12} cm^{-3} and background helium densities of 10^{12} cm^{-3} or less. From previous calibration of the LIF fluorscence dectection using absorption spectroscopy of NH [60], we estimate we have initial loading densities of NH on the order of 10^8 cm^{-3}. Since we trap many fewer NH atoms, we don't expect to see any effect of collision with NH on the nitrogen time decay. However, by varying the amount of nitrogen cotrapped with NH, we may be able to extract information about N-NH collision processes.

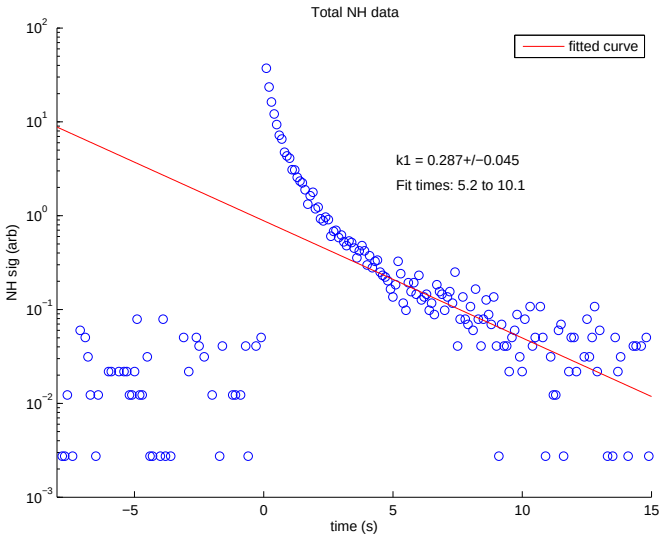

Figure 3.6: NH decay. Taken at trap depth of 3.9 T, cell temperature 570 mK, $\eta = 9.1$.

Since the density of trapped nitrogen is similar to the density of background helium gas, we must be careful that the process by which we vary the nitrogen density does not inadvertently also vary the amount of helium background gas. Thus, to change the amount of nitrogen loaded into the trap, we vary the N_2 - H_2 mixture of the process gas between (90%, 10%) to (3%, 97%). The cell temperature time profile must also be repeatable from run to run, since variations in the profile could change the NH loss rate as well. Figure 3.7 shows the fractional variation from the mean cell temperature time profile for each of the data sets. We see that the cell temperature time profiles agree within 2% of the mean at all times.

To take the data, we co-load N and NH molecules into the trap and observe the NH fluorescence decay for 15 s after loading. Then, at 15 s we detect the amount of atomic nitrogen cotrapped with NH. A typical NH time decay is shown in Figure 3.6. At times less then three seconds, the NH loss is rapid, as the He buffer gas is

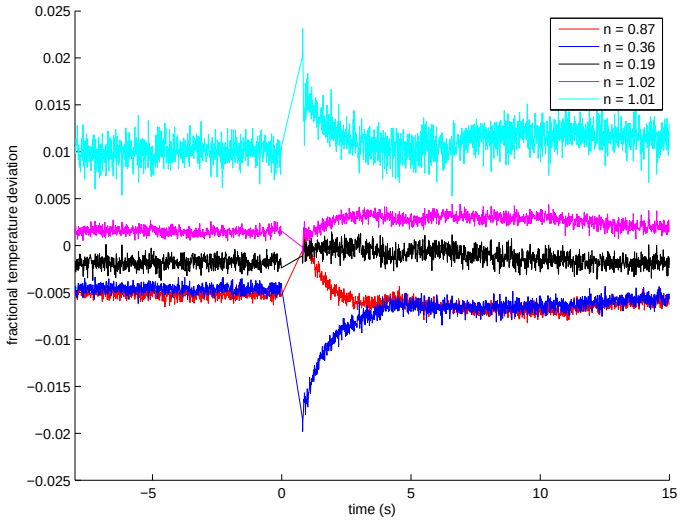

Figure 3.7: NH N cell temperature deviation

being pumped out of the cell. For times between five and ten seconds, the NH decay fits well to a single exponential before being obscured by noise. We fit for the NH loss rate between five and ten seconds for each of the different cotrapped nitrogen densities, and the results are shown in Figure 3.9. To calibrate the absolute nitrogen density, we take an additional N decay curve, shown in Figure 3.8. We then set the calibration of the nitrogen density by matching the observed $\langle k_{2b} \rangle$ loss rate with the calculated rate from quantum scattering calculations. Since the nitrogen density changes between the five to ten second observation period and the detection time at 15 s, we use the $\langle k_{2b} \rangle$ loss rate to infer the average nitrogen density in the trap during the measurement window.

The slope of the best fit line in Figure 3.9 is the observed N-NH loss collision rate consant, $\langle k_{N-NH} \rangle$, where we are describing the total NH loss by the eqation of the form:

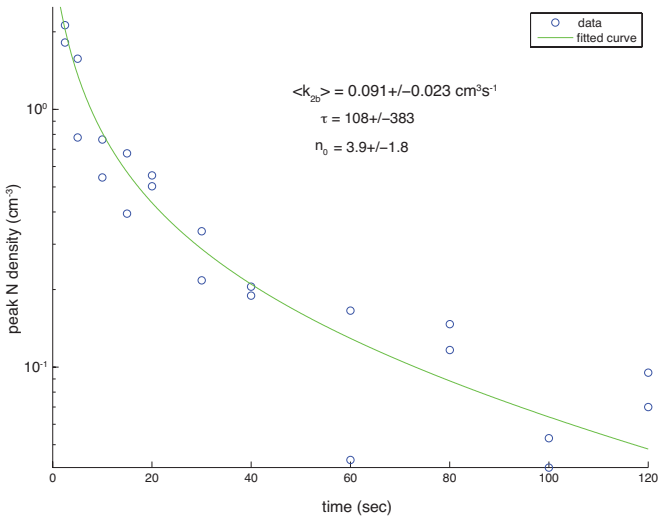

Figure 3.8: N decay for density calibration.

$$\dot{n}_0^{(NH)} = -\left(n_0^{(N)}\left\langle k_{\mathrm{N-NH}}\right\rangle + n_0^{(He)}\left\langle k_{\mathrm{He-NH}}\right\rangle\right) n_0^{(NH)} \tag{3.30}$$

were the large brackets $\langle\rangle$ denote averaging over the trap volume. To relate the observed $\left\langle k_{\mathrm{N-NH}}\right\rangle$ loss to the actual value $k_{\mathrm{N-NH}}$, we perform the trap average numerically over the real trapping field to arrive at the expression

$$k_{\mathrm{N-NH}} = 0.9\left(\frac{\eta_{(\mathrm{N})} + \eta_{(\mathrm{NH})}}{\eta_{(\mathrm{NH})}}\right)^3 \left\langle k_{\mathrm{N-NH}}\right\rangle \tag{3.31}$$

$$= 14.\left\langle k_{\mathrm{N-NH}}\right\rangle \tag{3.32}$$

Using this expression we arrive at a value of $k_{\mathrm{N-NH}} = 2.0(8) \times 10^{-12}$ cm^{3}s^{-1}. The uncertainty in $k_{\mathrm{N-NH}}$ is a reflection of the systematic uncertainty in the measurement of the NH loss rate and atomic nitrogen density. By changing the duration of the window over which we fit the NH loss by ± 1 s we see shifts of about $\pm 30\%$ in the best

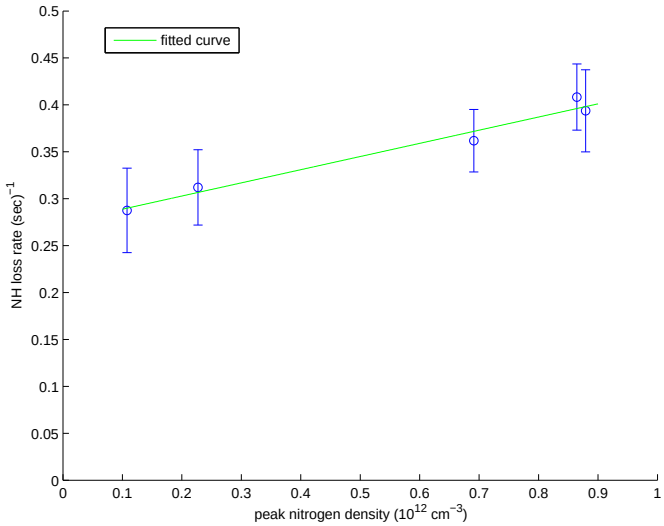

Figure 3.9: NH loss vs N density

fit value for $k_{\mathrm{N-NH}}$. It should be noted this measurement represents loss from all N-NH collisions, both elastic (evaporative) and inelastic. For the data taken here, $\eta = 9$ for NH. If we simply look at the fraction of elastic N-N collisions that lead to evaporative loss at $\eta = 9$, we find $f(\eta) \approx 10^{-3}$. Preliminary scattering calculations from Timur Tscherbul give a $k_{el}^{(\mathrm{N-NH})} = 2 \times 10^{10}$, then roughly 10% of the measured loss is due to evaporative collisions, and we have $\gamma_{\mathrm{N-NH}} = 110(+90, -35)$. For comparison, Tscherbul calculates a preliminary $\gamma_{\mathrm{N-NH}} = 770$.

This measurement of a large γ in an atom-molecule system opens the door for future work towards sympathetic cooling of molecules to ultracold temperatures.

Chapter 4

Future Directions

4.1 Killing the film

For the eventual path of evaporative cooling of atomic nitrogen and NH, the background density of helium must be lowered. For evaporative cooling, the depth of the trap is lowered, and once lowered below the temperature of the cell walls a single (or few) collision(s) with helium can remove an atom or molecule from the trap. Since typical evaporation times are 100 s [77], and elastic rate constants $k_{\mathrm{el}} = 10^{-10}$ cm^{-3}s^{-1}, this implies that the background helium density be less than 10^8 cm^{-3}.

We believe our current background buffer gas densities are set by desorption of helium from a film coating the inside of our trapping cell. First let's consider the case were the helium film is thick enough so that the buffer gas above the film is at the equilibrium vapor pressure. Vapor pressure curves for ^{3}He and ^{4}He are shown in Figure 4.1. If atomic nitrogen and NH are to be loaded from a room temperature molecular beam, it is unlikely the cell temperature could be cooled below 100 mK

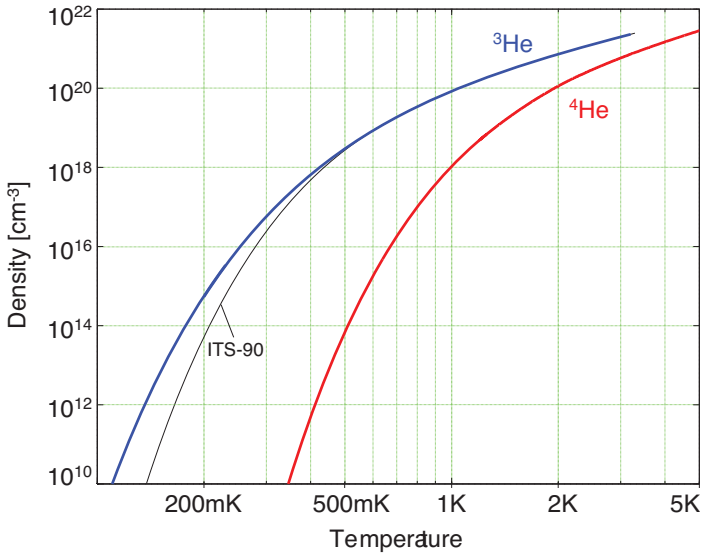

Figure 4.1: Helium vapor pressure curves. [78]

with a dilution refrigerator [79] to ensure low enough ^{3}He vapor pressure simply due to cell heating from blackbody radiation.

Next we can consider the situation of a thinned ^{3}He film, where a ^{3}He atom is now more tightly bound to the cell wall due to its binding energy with the surface of the copper. The dynamics for this situation and their effects on trapped atom lifetimes have been simulated and experimentally investigated in the theses of Michniak and Brahms [71, 75]. In experiments described in Brahms's thesis **??**, they load atoms into a magnetic trap using helium buffer gas desorbed from this thin film. Following loading, they observe lifetimes of 100 s at full trap depth, though atom loss is rapid for trap depths below 500 mK. They conclude the likely source of loss is collisions with background gas of densities on the order of 10^{11}cm^{-3}. In experiments described in Michniak's thesis [71], they achieve 1000 s trap life times at trap depths of 160 mK

by performing a "cryo-bakeout." They heat the cell to a temperature of 600 mK for a period of 10 s to drive the ^{3}He film off the cell walls and into a separate pumping region before cooling the cell to 400 mK to reabsorb any remaining helium. Since NH is only $2\mu_B$, this "cryo-bakeout" would have to occur at lower temperatures, between 200 and 400 mK, to avoid removing the NH from the trap. Given the experiences of Brahms and Michniak, it appears the window of experimental conditions is fairly small for achieving the low background helium densities necessary for further cooling of NH after loading with ^{3}He buffer gas.

Instead one can consider loading with ^{4}He buffer gas. Using the pulsed valve buffer gas loading technique with ^{4}He is a bit more technically challenging, as ^{4}He is superfluid at these temperatures. Our pulsed valve becomes a leaky valve if we introduce ^{4}He into the reservoir. While a redesign of the trapping cell and valve might solve this problem, moving to a closed cell geometry with ^{4}He is more feasible. Doret and coworkers have recently demonstrated evaporative cooling of meta-stable He to quantum degeneracy using buffer gas loading with ^{4}He as the buffer gas [80]. They produce their meta-stable He using a cryogenic RF discharge generated in the trapping region of the cell [77]. Recent work in our lab has demonstrated production of N and NH in a cryogenic discharge at 10 K. Thus, we expect that N and NH produced in a cryogenic RF discharge can be loaded into a magnetic trap. Such a setup should provide ideal conditions for further study of cold collisions of N and NH in a magnetic trap. Construction of a new experimental trapping cell for production of N and NH is currently underway.

4.2 Improved Nitrogen Detection

While the pulsed dye laser used in these experiments for pulsed laser excitation has been suitable for initial investigations of cold magnetically trapped atomic nitrogen, the detection method suffers from significant shot-to-shot variation of the nitrogen fluorescence. Future experiments with atomic nitrogen will greatly benefit from a more reliable, precise technique for detection using a pulsed laser that produces frequency-stable narrowband single mode emission. This would significantly enhance the spectral resolution, excitation probability, and overall signal-to-noise of the atomic nitrogen detection. With increased signal to noise, it should be possible to image the resulting nitrogen fluorescence. This fluorescence, when viewed from a direction orthogonal to the direction of the laser propagation, would be able to provide a spatial density distribution of the trapped atomic nitrogen, from which trap temperatures could be estimated.

Two techniques are available for producing pulsed single mode emission at 207 nm. Both techniques require pulse amplification of narrowband CW-laser followed by frequency conversion in non-linear optical crystals. The CW-laser is used to seed the gain medium, which is typically pumped with an injection-seed Nd:YAG laser. If the pump laser is not injection-seeded and allowed to run multimode, intensity variations of the pump laser can cause additional broadening of the resulting laser radiation [81]. The first method consists of pulse amplification using laser dye as the gain medium. Pulsed dye amplifiers are available commercially, though careful tuning of the dye laser concentration is required to avoid frequency chirps of the amplified radiation of approximately 2×300 MHz (at the atomic tranisition frequency) [82]. Alternatively,

one can use Ti:Sapphire as the gain medium which leads to a smaller magnitude of frequency chirp at the expense of additional complexity of the laser is setup [83, 84].

Finally, one could consider moving towards spectroscopy of atomic nitrogen using the single photon transition near 120 nm. Considerable work in the development of reliable narrowband sources of CW light at 121.6 nm (Lyman-α) has been performed in the context of laser-cooling (anti-)hydrogen in a magnetic trap [64, 65, 85]. These techniques can also also be used for generation of light at 120 nm [86, 87]. This would open the possibility of laser-cooling for atomic nitrogen in a magnetic trap, though cooling times would be on the order of minutes for the current amount of power available from these sources [85].

4.3 Cold atomic nitrogen beam source

Previous experiments in our lab [88, 89] have worked on the development of high-flux beam sources for cold, slow atoms and molecules. In one experiment, guiding of O_2 molecules was demonstrated using permanent magnetic octopole guide. The guide was loaded with a near-effusive beam of O_2 produced in from two-stage buffer gas cell. In this experiment, guiding efficiencies as large as 10% were observed for a guide depth of 0.5 T with the $2\mu_B$ species. By using a slightly more complex Halbach-type guide, still built out of permanent magnets, it should be possible to achieve guide depths of 0.8 T [90, 91]. Guiding of a $3\mu_B$ species produced from a beam source similar to the one in Ref. [89] with this deeper guide should be extremely efficient. This would allow the nitrogen beam to be guided into a high vacuum region for loading into a trap or for use in collision experiments. Similar techniques have already been

demonstrated for production of cold beams of ND_3 via electrostatic guiding [92]. For cold nitrogen beams produced for use in collision experiments, the forward velocity of the beam could be tuned close to zero using two, or perhaps even a single stage of Zeeman deceleration [93].

The main difference between generating a *high flux* source of N atoms versus O_2 molucules is the introduction of the species into the buffer gas cell. With O_2, the molecules were simply introduced into the cell via a capillary tube, which is not an option for atomic nitrogen. One option is the production of atomic nitrogen via a cryogenic rf discharge, where N_2 molecules that have been frozen onto the cell wall are etched off and dissociated by the plasma. Using this technique, atomic nitrogen has been observed in our lab at temperatures of 4 K, though the amount of nitrogen has not been characterized. In reference [94] the authors demonstrate extraction of atomic nitrogen produced in an RF discharge at 200 K into a 2 K gas of helium. For production of the cold O_2 beam, a process gas flow of 10 sccm was used. Studies of RF-plasma sources indicate it may be possible to achieve efficient dissociation with RF powers as low as 150 W for process gas flows of 10 sccm [95, 96], although the calibration techniques used in those measurements are fairly indirect. Given the favorable guiding and slowing parameters for atomic nitrogen, development of a high flux cold beam source would be beneficial for cold collision experiments with nitrogen. We should also note that the guiding techniques discussed here for atomic nitrogen will work almost as well for the $2\mu_B$ species NH.

Appendix A

Atomic Nitrogen Detection

In order to use the TALIF technique to determine absolute densities of atomic samples, a quantitative understanding of the technique, extending to the properties of the atoms, the radiation, and their interaction is required. In a series of experimental papers, Bamford and coworkers analyzed two-photon absorption and 3-photon ionization in atomic oxygen, which has a similar electronic structure to atomic nitrogen [97–99]. In Reference [98], Bamford and coworkers use a well characterized single mode laser to perform two-photon excitation and extract absolute values for two-photon cross sections. Their measured values are 50% larger than the best available theoretical values [100]. The spectral properties of our pulsed dye laser system are less well known than those in Reference [98], so the goal of this Appendix is to arrive at order of magnitude estimates for atomic nitrogen densities and to give a general overview of two photon excitation.

A.1 Two-photon excitation

The two-photon excitation rate for an atom in an oscillating electromagnetic field can be calculated using standard perturbation theory techniques. A derivation of the rate can be found in the Appendix of Reference [68]. Here, we will simply quote the result, as it bears similarity to single photon excitation. The result from perturbation theory for the two photon excitation rate, $W^{(2)}$ is

$$W^{(2)} = \hat{\sigma}^{(2)} \left(\frac{I}{\hbar\omega} \right)^2 \tag{A.1}$$

where I is the laser intensity in W/cm^2, $\hbar\omega$ is the photon energy, and $\hat{\sigma}^{(2)}$ is the two-photon rate coefficient. The two photon rate coefficient can then be expressed as

$$\hat{\sigma}^{(2)}(\Delta) = \sigma_0^{(2)} g(\Delta) G^{(2)}(0) \tag{A.2}$$

where $\Delta = 2\omega_L - \omega_0$, is the radial frequency two-photon detuning from the atomic resonance, g is the normalized ($\int g(\Delta) d\Delta = 1$) lineshape function, and $G^{(2)}(0)$ is the second-order intensity-correlation function which depends on the photon statistics of the laser. The two-photon cross section, $\sigma^{(2)}$, can be expressed as

$$\sigma^{(2)} = (2\pi)^3 \left(\frac{e^2}{4\pi\varepsilon_0 \hbar c} \right)^2 (\hbar\omega)^2 \left| \sum_i \frac{\langle e| r^\lambda |i\rangle \langle i| r^\lambda |g\rangle}{E_g - E_i + \hbar\omega} \right|^2 \tag{A.3}$$

where $r^\lambda = \mathbf{r} \cdot \varepsilon_\lambda$,$\varepsilon_\lambda$ is the polarization of the laser [100], $|g\rangle, |e\rangle$ are the ground and excited states, E_i is the energy of atomic state $|i\rangle$, and the summation is over a complete set of atomic states $|i\rangle$. When a single intermediate state dominates the sum in equation A.3, it is possible to re-express $\sigma^{(2)}$ in terms of oscillator strengths, f_{ij} [101],

$$\sigma^{(2)} = 2\pi^3 \frac{\hbar}{m} \left(\frac{e^2}{4\pi\varepsilon_0 \hbar c} \right)^2 \frac{(\hbar\omega)^2}{\omega_{gi}\omega_{if}} \frac{f_{gi} f_{ie}}{(E_g - E_i + \hbar\omega)^2} \tag{A.4}$$

Using this expression and the measured oscillator strength from Reference [102] for the transition from the ground state to first excite ^{4}P manifold yields an estimate of $\sigma^{(2)} = 5 \times 10^{-36}$ cm^4. In Reference [68], the full sum-over-states of equation A.3 is evaluated with the radial integrals carried out using model wavefunctions. The calculation yields a result for the nitrogen two-photon excitation cross section of $\sigma^{(2)} = 1.4 \times 10^{-36}$ cm^4. The author also carries out similar calculations for two-photon excitation cross sections of atomic oxygen, which are in good agreement with other experimental and theoretical values [100]. Therefore, we will use this value of $\sigma^{(2)}$ in our calculations.

We can model the excitation process of atoms in our trap using kinematic rate equations,

$$\dot{n}_{\rm gr}(r,t) = \hat{\sigma}^{(2)}\Phi^2(r,t)(n_{\rm ex}(r,t) - n_{\rm gr}(r,t)) \tag{A.5}$$

$$\dot{n}_{\rm ex}(r,t) = \hat{\sigma}^{(2)}\Phi^2(r,t)(n_{\rm gr}(r,t) - n_{\rm ex}(r,t)) - An_{\rm ex}(r,t) - \sigma_{\rm PI}\Phi(r,t)n_{\rm ex}(r,t) \tag{A.6}$$

where $n_{\rm gr}(r,t)$ and $n_{\rm ex}(r,t)$ are the atomic densities in the ground and excited states, $\hat{\sigma}^{(2)}$ and $\sigma_{\rm PI}$ are the effective two-photon and photon-ionization cross-sections, $\Phi(r,t) = I/(\hbar\omega)$ is the incident photon flux, and A is the fluorescence decay rate. The quantity of interest, the total number of fluorescence photons emitted per laser excitation pulse per unit volume is given by integrating the fluorescence rate over all time:

$$n(r)_{h\nu} = \int_{-\infty}^{\infty} An_{\rm ex}(r,t)dt \tag{A.7}$$

where $n_{\rm ex}$ is given from the solution of the kinematic rate equations. In the experiments described in this thesis, a high power (1 mJ) pulsed laser is focused onto the atomic nitrogen at intensities such that all the rates described in equations A.5, A.6

are comparable. Hence, in general, integration over the spatial and temporal profiles of the laser excitation, and numerical analysis of the rate equations are required for parts of the analysis in this thesis.

First, we will consider a more simple case. In the low intensity limit, where depletion of the ground state and photo-ionization are negligible, one can solve for the total number of fluorescence photons produced from the sample by integrating equation A.7 over all space [97], yielding:

$$N_{h\nu} = \int n_{h\nu}(r)dV \tag{A.8}$$

$$= \hat{\sigma}^{(2)} \frac{E^2}{(h\nu)^2} \int n_{\mathrm{gr}}(r) S^2(r) dV \int_{-\infty}^{\infty} F^2(t) dt \tag{A.9}$$

where we have taken the photon flux $\Phi(r,t) = E\ S(r)F(t)/h\nu$, where E is the pulse energy, and $\int S(r)dA = 1$, and $\int F(t)dt = 1$, where $S(r)$ and $F(t)$ are the normalized spatial and temporal profiles of the laser beam. Here we have assumed the spatial and temporal variations are independent. For the case of Gaussian spatial and temporal profiles and uniform atom density over length L, equation A.16 can be integrated to give

$$N_{h\nu} = n_{\mathrm{gr}} \left\{ \hat{\sigma}^{(2)} \frac{LE^2}{(h\nu)^2} \frac{1}{\pi w_0^2} \frac{\sqrt{2\ln(2)}}{\sqrt{\pi}\tau_{\mathrm{ex}}} \right\} \tag{A.10}$$

where $2w_0$ is the $1/e^2$ full-width of the spatial profile and τ_{ex} is the full-width-half-max of the temporal profile. For the low intensity limit, we see that the signal $N_{h\nu}$ scales as the square of the pulse energy, E, as expected for a two-photon process.

We note that the term in braces in equation A.10 has units of volume. Hence, we will term this the two-photon effective excitation volume, $V_{\mathrm{exc}}^{(2)}$. At higher intensities, where depletion of the ground state and photo-ionization become important, the

description	symbol	typical value	units
two-photon cross section [68]	$\sigma^{(2)}$	1.37	10^{-36} cm^4
photo-ionization cross section[a]	σ_{PI}	10^{-18}	cm^2
excited state lifetime [67]	A	26	nsec
excitation pulse energy	E	~ 0.6	mJ
beam waist	w_0	10 to 150	μm
effective laser linewidth	$\Delta\nu$	6 to 30	GHz
pulse duration (FWHM)	τ_{ex}	9.5	ns
2nd-order photon correlation coefficient[b]	$G^{(2)}(0)$	1.5 to 3	
photon collection efficiency	α	10^{-4}	
PMT sensitivity	β	3.5	mV ns photon^{-1}

[a] Actual value unknown, typical value given [97, 103].

[b] Actual value unknown, typical value given [99].

Table A.1: Parameters and typical values for atomic nitrogen excitation.

kinematic rate equations can numerically integrated to arrive at a value for $V_{\mathrm{exc}}^{(2)}$. Furthermore, one can generalize this approach to include a spatial varying atomic density profile, as are typically found in our magnetic trap, to arrive at an excitation volume dependent on trap geometry,

$$N_{h\nu} = n_0 V_{\mathrm{exc}}^{(2)} \tag{A.11}$$

now, where n_0 represents the peak density at the center of the trap, and $V_{\mathrm{exc}}^{(2)}$ depends on the spatial distributions of both the atoms and the laser excitation. Finally, to convert the relative nitrogen peak trap density to an absolute density, the collection efficiency of the PMT-lens system can be estimated. The parameters necessary to convert our measured fluorescence signal are summarized in Table A.1.

A.2 Characterization of TALIF parameters

In this section we will discuss how we measure or estimate the parameters listed in Table A.1 necessary for calibrating the TALIF technique.

Spatial profile

The spatial intensity distribution of the 207 nm laser light at the focus is required for calculation of the excitation probability. This, in general, is determined by the focal length of the focusing lens, the size of the beam at the position of the lens, and the mode quality of the beam itself. Figure A.1(a) shows the spatial intensity distribution of the 207 nm laser light near the focal point of a 1 m lens, measured using a CCD camera. The focused beam in general is astigmatic, as no great care is taken when aligning the beam. The quantity we desire is the integrated square of the normalized intensity profile, $\int S(r)^2 dA$. For a gaussian beam, the profile at the focus is given by,

$$S(r) = \frac{2}{\pi w_0^2} \exp[-2r^2/w_0^2] \tag{A.12}$$

$$\int S(r)^2 dA = \frac{1}{\pi w_0^2} \tag{A.13}$$

From the measured spatial distribution, one can numerically calculate a value for $\int S(r)^2 dA$. For the image in Figure A.1(a), the value is $\int S(r)^2 dA = \pi^{-1}(135\mu m)^{-2}$. Figure A.1(b) shows the measured effective beam waist using the CCD imaging camera at various positions near the focal point of the 1 m focusing lens used in the experiment. As the extent of the atom cloud in the direction of the laser beam propagation is a few mm, we can see from this figure that we can assume a constant laser

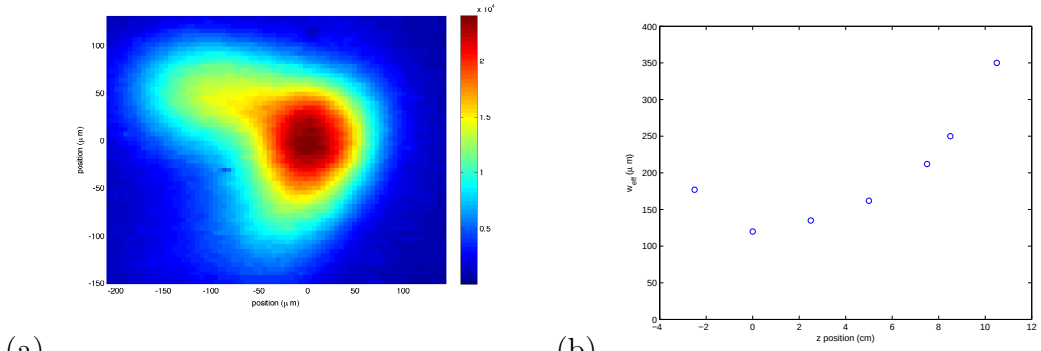

(a) (b)

Figure A.1: 207 nm intensity distribution at focus.

beam waist over the extent of the atom cloud. For data analyzed in this thesis we assume a value of $\int S(r)^2 dA = \pi^{-1}(120\mu m)^{-2}$.

Temporal profile

The temporal profile of the laser excitation is recorded using a fast photodiode[1] sampled using TDS 744A, 500MHz bandwidth oscilloscope. In order not to damage the photodiode with the pulse laser, a fraction of the laser is sent onto a piece of alumina beam stop toward which the fast photodiode faces (Fig. 2.7). The photodiode then collects the scattered light. From the recorded profiles, values of $\int F(t)^2 dt = \frac{\sqrt{2\ln(2)}}{\sqrt{\pi}(\tau_{\rm ex})}$ can be calculated, with typical values of $\frac{\sqrt{2\ln(2)}}{\sqrt{\pi}(9.5{\rm ns})}$, consistent with the specified pulse duration of $\tau_{\rm ex} = 10$ ns.

[1] Thorlabs DET10A silicon detector, rise time < 1 ns

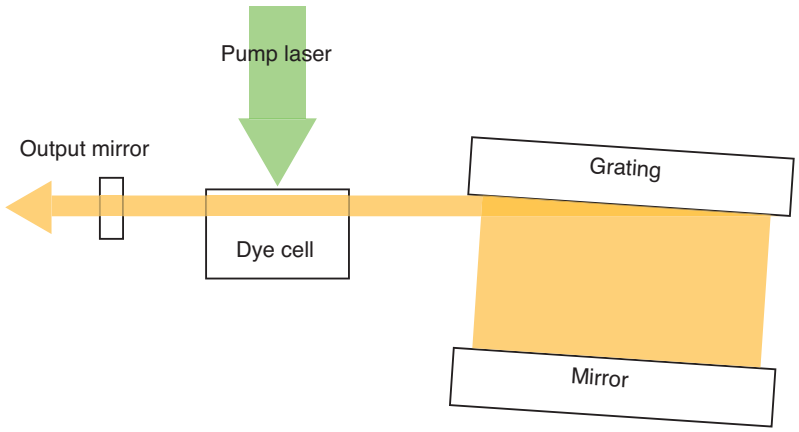

Figure A.2: Pulse dye laser resonator cavity.

Spectral profile

The spectral profile of the laser light has been the most vexing aspect of our analysis of two-photon excitation of atomic nitrogen, as well as a the likely source of significant shot-to-shot variation in our detected nitrogen fluorescence signal.

To begin the discussion, we will begin with a brief recap of the operation of the pulsed dye laser. The radiation at 206.7 nm is produced by tripling light at 620 nm produced from a nanosecond pulsed dye laser. The pulsed dye laser is a commercial Sirah Cobra-Stretch dye laser pumped by a Nd:YAG SpectraPhysics Quanta Ray Lab 130. The linewidth of the pump laser is specified as less than < 1 cm^{-1}, which indicates the pump laser oscillates in many longitudinal modes. This will lead to fast oscillations in the instantaneous intensity of the pump laser that can map on to intensity oscillations and frequency broadening of the resulting dye laser output [81]. The frequency selectivity of the pulse dye laser is determined by the dispersion of a grazing incidence grating making up one part of the cavity, shown in Figure A.2.

An upper limit for the total linewidth, $\Delta\lambda$, (FWHM) of the laser from a single pass analysis of the dispersive cavity gives the expression [104]:

$$\frac{\Delta\lambda}{\lambda} = \frac{2\sqrt{2}\lambda}{\pi l(1+\sin\phi)} \tag{A.14}$$

where l is the length of the grating illuminated and ϕ is the angle between the normals of the grating and the tuning mirror. For the parameters of the Sirah laser, this yields an upper limit of $\sim$ 2 GHz. The agrees well with the manufacturers specified time average linewidth of the laser of 1.4 GHz.

In addition to the dispersive frequency selection provided by the grating, the two end mirrors of the resonator cavity create a set of preferred longitudinal modes for lasing. For the specification of the Sirah dye laser, the longitudinal mode spacing is roughly 560 MHz, corresponding to the free spectral range of the laser cavity $c/2L$, where $L = 27$ cm is the center line length of cavity. As a result, we expect one to several longitudinal modes to lase for each laser pulse, giving a complex comb-like spectral distribution for the radiation produced from the pulsed dye laser.

To analyze the spectral properties of the output of the pulsed dye laser we use a Fizeau interferometer, similar to the ones described in References [105, 106]. A schematic of the interferometer is shown in Figure A.3. The interferometer consists of two flat parallel partial reflectors (95% reflecting), with a slight angular misalignment. The resulting interference pattern is recorded on a linear CCD array. Using this technique, the spectral profile of individual laser pulses can be recorded. Figure shows four typical individual pulse spectrums, along with a the average of 100 consecutive pulses. The spectrum show two free spectral ranges of the interferometer; the picks between 1 and 2 GHz are copies of the peaks between 3 and 4 GHz. The interferometer

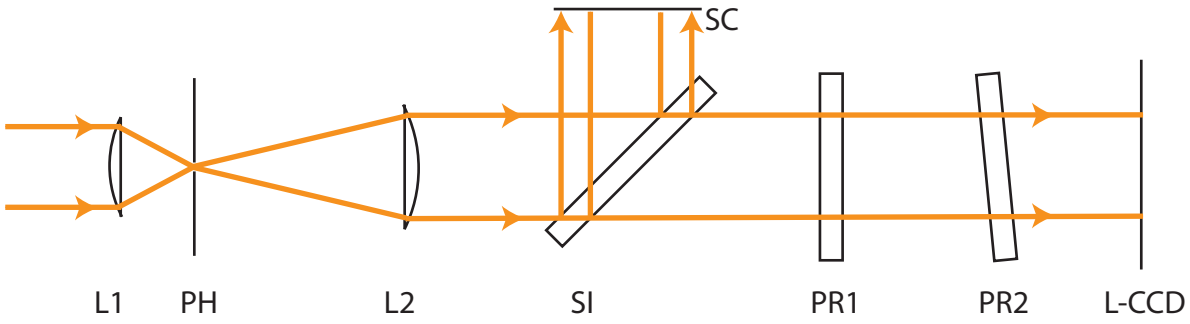

Figure A.3: Fizeau interferometer. Lens 1 (L1) focuses light onto pinhole (PH) for spatial filtering. L2 collimates the beam. Collimation is verified using a shearing interferometer (SI). Partial reflections 1,2 (PR1,2) make the Fizeau interferometer. The resulting interference pattern is record with a linear CCD array (L-CCD).

alignment was checked by co-aligning a frequency stabilized He-Ne laser beam, which made identification of the free spectral range simpler. The frequency calibration is approximate, made assuming a cavity mirror spacing of 7.0 cm. We see from the recorded spectra the mode spacing of the adjacent peaks are roughly 600 MHz, consistent with the 560 MHz mode spacing expected from the 27 cm resonator cavity. We also see that on average 2 to 3 modes lase, consistent with the 1.4 GHz linewidth predicted from the grazing incident grating.

While we seem to have a good understanding of the laser light at 620 nm, its complex structure may lead to complications in the interpretation of spectra taken with the 207 nm light generated from frequency mixing. From the interferometer measurements, it is clear there is shot-to-shot frequency jitter of the laser at 620 nm on the order of 1 GHz. This corresponds to a frequency jitter of 3 GHz at 207 nm and 6 GHz (0.2 cm^{-1}) at the atomic transition frequency.

We can also use the observed atomic transition linewidth to estimate the linewidth

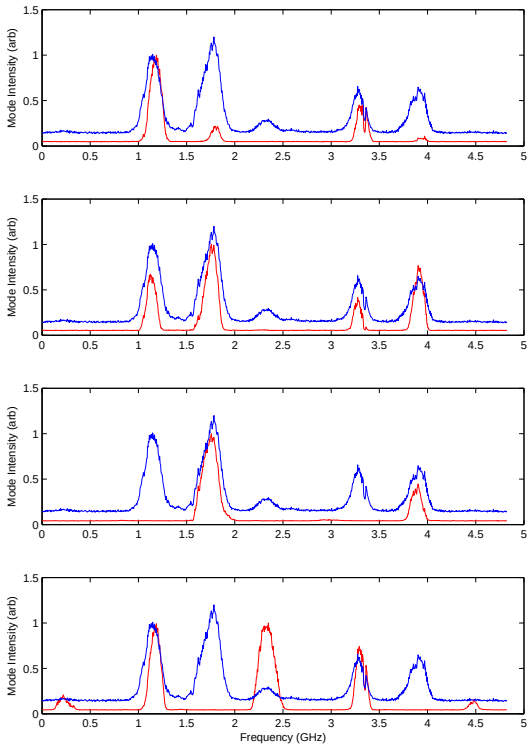

Figure A.4: Pulsed dye laser spectral analysis. The upper blue trace in each spectrum represents the average of 100 consecutive laser pulses. The lower red spectra represents individual pulses. The heights of the spectra have been normalized, and two free spectral ranges of the interferometer are shown on each spectrum.

of the laser at 207 nm. Here we will show data taken at room temperature about 1 cm after the exit of the atomic/molecular beam from the DC glow discharge. The measurements are made in the absence of any applied magnetic field, so the three broadening mechanisms we will consider Doppler broadening, laser lineshape broadening, and power broadening. Doppler broadening of a two-photon transition is similar to the case of a single photon transition. The motion of the atom causes a fractional shift in the atomic transition frequency—independent of whether the transition is

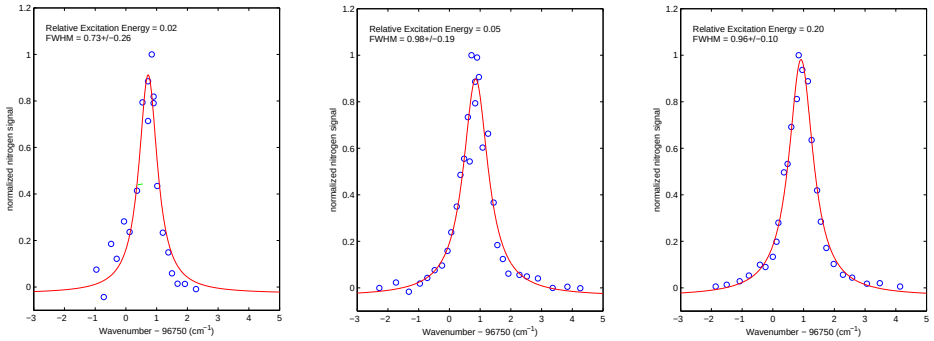

Figure A.5: Atomic nitrogen spectrum taken at room temperature using the DC glow discharge source.

a single or two photon transition. Therefore, the doppler broadening (FWHM) for nitrogen at a temperature of 300 K is 0.27 cm^{-1}. Figure A.5 shows the observer atomic nitrogen spectrum, plotted as the atomic transition frequency. The observed linewidths are all significantly wider than the expected doppler width. Measurement of NH produced in a similar mannner yield linewidths on the order of 2 to 3 GHz (< 0.1cm^{-1}), consistent with a Doppler temperate near 300 K. Therefore it is likely the observed nitrogen linewidth has contributions from either the fundamental laser linewidth, power broadening, or both.

If power broadening were a significant source of broadening, we would expect to see the effects of saturation in the excitation probability. Figure A.6 shows the observed nitrogen signal (on resonance) as a function of pulse excitation energy. The curves are plotted on a log-log scale so that it is straight forward to identify each of the excitation scaling regions. The regions with the steepest slope correspond to a fluorescence signal$\sim E^2$ dependance, the expected low energy limit. The intermediate slopes correspond to signal$\sim E$, indication the onset of either photo-ionization or saturation of the two-photon transition. Finally, at the highest pulse energies and the short

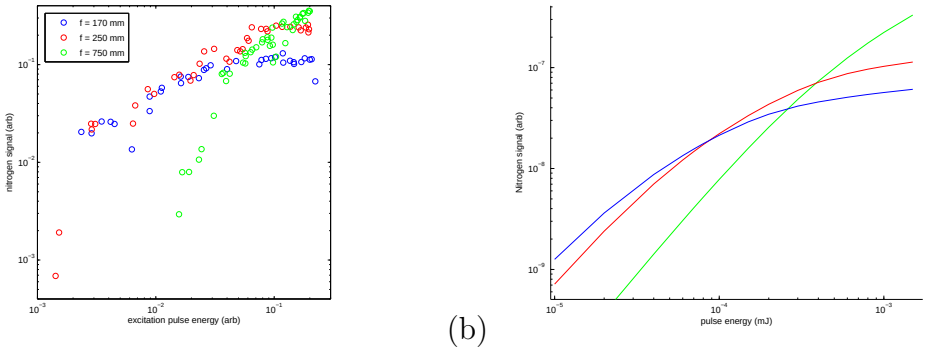

(a) (b)

Figure A.6: Nitrogen signal versus excitation energy for three different focal length lenses. (a) shows data taken 1 cm after the glow discharge. (b) shows simulated dependance calculated integration of the rate equations A.5, A.6

focal length lens, the signal becomes nearly independent of pulse energy, indicating saturation of the transition and additional photo-ionization. It is interesting to note that the simulations seems to indicate the slight downturn in nitrogen signal for the 750 nm lens at high pulse energies is more likely due to photo-ionization than saturation of the transition. The two free parameters that were varied to reach qualitative agreement between the simulation and experiment were laser linewidth ($\Delta_L = 5$ GHz) and photo-ionization cross section ($\sigma_{\mathrm{PI}} = 10^{-18}$ cm^2). Without the addition of σ_{PI}, the slight downturn of the 750 nm lens curve was not present.

The spectra in Figure A.5 where taken with the 750 mm focal length lens at the pulse energies noted on each plot. The first spectra is taken in the E^2 regime, away from saturation, the middle spectra is taken right at the onset of linear regime, and the third spectra is taken clearly in the linear regime. It may be the case that the slightly larger linewidths observed in the second two spectra are related to the onset of photo-ionization. For the first spectra taken will in the E^2 regime, we roughly expect the linewidth to be $(2\Delta_L^2 + \Delta_D^2)^{(1/2)}$. If we first subtract off the 0.2 cm^{-1} contribution

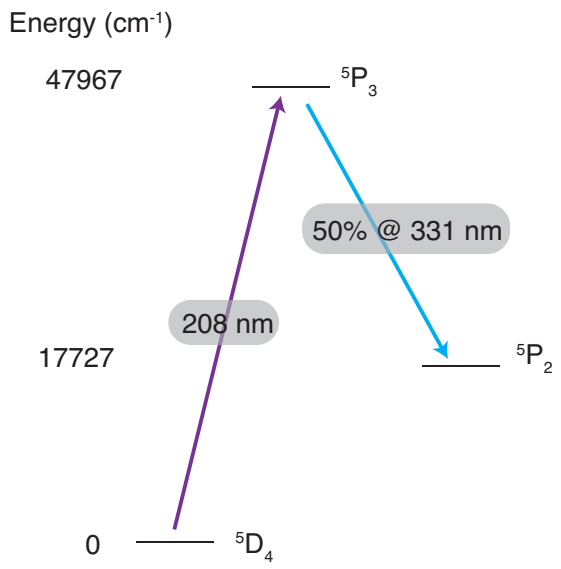

Figure A.7: Electronic energy levels in iron for laser induced fluorescence

from laser jitter, this yields a 207 nm laser linewidth of 0.3 cm^{-1}, or 9 GHz. This is somewhat puzzling, for if we simply triple the 1.4 GHz linewidth of the 620 nm light, we would expect a 207 nm linewidth closer to 4 GHz. From this analysis, it appears likely that the laser linewidth at 207 nm is between 1 and 10 GHz.

Another way to get a handle on the properties of the radiation produced by the pulsed dye laser is to an atomic species with a single photon transition as your spectral analyzer. In our case we used atomic iron (Fe), as it has an electronic energy level structure well suited for our purposes. The relevant energy levels are shown in Figure A.7. First, it has a single photon transition at 208 nm, which is a wavelength sufficiently close to the excitation wavelength used in atomic nitrogen TALIF. Second, about 50% of the fluorescence from the excited state is emitted at 331 nm, allowing

for straight forward detection using a colored glass filter[2] and a PMT. Atomic iron can be efficiently produced via laser ablation of a foil target into a room temperature cell filled with several Torr of helium gas. Detection of the atomic iron using the pulsed dye laser occurs about 6 ms after the ablation pulse, sufficiently long that the iron should be thermalized via collisions with the helium buffer gas to room temperature, although this is not independently verified. The full-width-half-max of a 300K doppler broadened spectrum of iron on this transition is about 0.08 cm^{-1}, sufficiently narrow to do simple probes of the pulsed dye laser spectral properties. At excitation pulse energies as low as 10 nJ, the peak laser power incident on the atoms from a 10 ns pulse is still on the order of 1 W, so power broadening will likely be the dominant broadening mechanism (with a saturation intensity on the order of $\sim$ 100 mW/cm^2).

Figure shows the atomic iron fluorescence taken at three different pulse energies. There is clear evidence of power broadening for the two spectra taken at higher energies. A fourth spectra, not shown, was taken at a pulse energy of 2 nJ and had a width similar to, or slightly large than the spectra at 10 nJ, possibly limited by electrical noise from the YAG flashlamp. If we take the 0.46 cm^{-1} linewidth, subtract from it the jitter of 0.1 $cm^{-1}$and include the 300 K Doppler broadening we arrive at an estimate of a 207 nm linewidth of 10 GHz.

To close the discussion on the spectral properties of the 207 nm we present a final nitrogen spectrum, taken in the magnetic trap at about 600 mK. The fit to a Lorentizian yields a full-width-half-max of 0.78 cm^{-1}, though it appears the fit may slightly under estimate the peak height. From spectrum like these, I suspect that

[2]Schott Glass UG-11

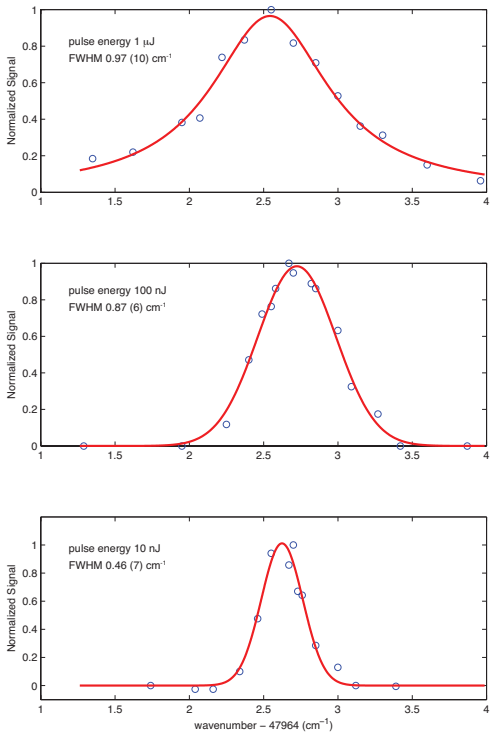

Figure A.8: Laser induced fluorescence spectrum of iron.

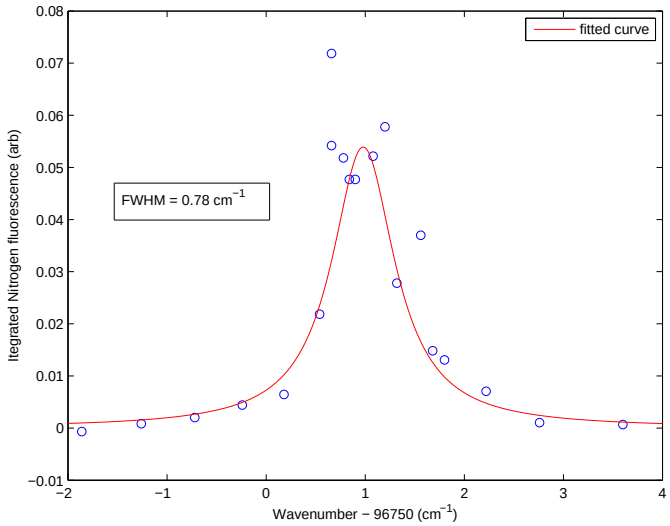

Figure A.9: May 6 spectrum.

we perhaps underestimate the amount of frequency jitter from shot-to-shot and the effect it has on our measured linewidths and signal peak heights. If the pulsed dye laser is to be used in future nitrogen trapping experiments, recording the Fizeau interferometer spectrum[3] for each excitation pulse might help sort out some the the remaining details.

A.2.1 Detection sensitivity

We can first estimate an upper limit on the collection efficiency with a simple calculation from the geometry, depicted in Figure 2.6. The quantum efficiency of the PMT will be considered separately. An 8 mm diameter clear aperture fused silica lens 40 mm from the atoms collects the fluorescence. In addition, there are three

[3]which could be calibrated using a co-propagating stabilized HeNe laser

uncoated fused silica vacuum windows, a sapphire window, a fused silica dichroic beamsplitter, and an interference filter. Assuming the fluorescence is isotropic and taking into account the transmission of each of the optical elements, this results in a fractional collection efficiency of approximately 7×10^{-4}. A crude method, using a small light bulb in place of the fluorescing atoms, was used to measure the collection efficiency, yielding approximately 3×10^{-4}. From previous experiments with NH, using simultaneous fluorescence and absorption detection in a similar setup, the fluorescence collection efficiency was measured to be 6×10^{-5}. A similar comparison of the absorption rate for Cr (50 GHz) to the fluorescence count rate divided by the quantum efficiency of the PMT (130 KHz) yields a photon collection efficiency of approximately 2.5×10^{-6}. This poor efficiency for Cr may be partly explained by the optical coatings for the lens and beamsplitter being optimized for nitrogen and NH wavelengths, which degrades the efficiency by a factor of approximately 2.5. The observed Cr fluorescence collection efficiency is then 6×10^{-6}, still lower than expected. For the calculations in this thesis, we take the collection efficiency to be approximately 1×10^{-4} for atomic nitrogen.

A.2.2 Conclusion

Based on observed in trap fluorescence excitation power curves, as well as a rough estimate of laser beam parameters, we can say with confidence the we are exciting atomic nitrogen in the low intensity limit. We can then use the expression derived

earlier to calculate the number of fluorescence photons per laser pulse.

$$N_{h\nu} = \int n_{h\nu}(r)dV \tag{A.15}$$

$$= \hat{\sigma}^{(2)} \frac{E^2}{(h\nu)^2} \int n_{\mathrm{gr}}(r) S^2(r) dV \int_{-\infty}^{\infty} F^2(t) dt \tag{A.16}$$

Our uncertainty in the absolute calibration is dominated by three paramters: the photon collection efficiency of our collection optics, the two-photon cross section, and the effective laser linewidth. Each of these values are probably good to within a factor of 2 to 3. Thus, we can expect our predicted atomic nitrogen densities to be good to about an order of magnitude.

Appendix B

Atomic Chromium Data

As mentioned in Chapter 2, we use atomic chromium as a test species for certain diagnostics. In particular, it is not possible to measure atom or molecule temperatures in the trap using either TALIF spectroscopy for N nor LIF for NH. The TALIF spectra are insensitive to Zeeman shifts, and the LIF spectra are truncated due to the limited collection volume of the fluoresce collection lens. Using absorption spectra taken with atomic chromium on the $|^7\mathrm{S}_3, m_j = +3\rangle \rightarrow |^7\mathrm{P}_4\rangle$ transition at 425 nm, it should be possible to compare a spectroscopically measured temperature with the cell thermometer temperature.

A sample Cr spectrum along with a simulated spectrum is shown in Figure B.1. While the simulation of the complete spectrum is somewhat complicated [72], the estimation of the temperature from a trap spectra can be done a bit more simply. The temperature information in the spectra resides in the high frequency tail of the spectra. The atoms at large frequency shifts correspond to atoms at high magnetic field, whose relative density goes as $\exp(-\mu B/k_\mathrm{B}T)$. The magnetic field correspond-

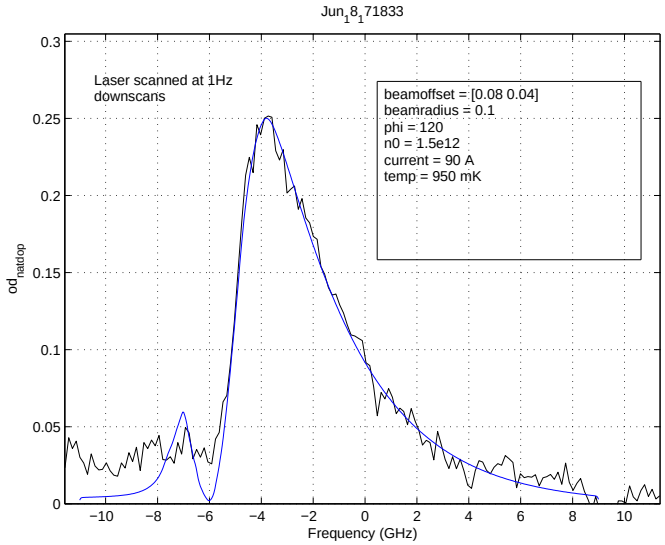

Figure B.1: Trapped Cr spectrum.

ing to a given frequency shift is calculated from the differential energy shift between the ground and excited states: $h\Delta f = (\mu_{\rm ex} - \mu_{\rm gr})B$. Hence, the relative density at large frequency shifts is given by

$$n(\Delta f) \sim \exp\left[-\frac{\mu}{\Delta\mu}\frac{h\Delta f}{k_{\rm B}T}\right] \tag{B.1}$$

Using either this expression or the spectrum fitting code, applied to the $|^7{\rm S}_3, m_j = +3\rangle$ state for the spectrum in Figure B.1 yields an atom temperature of approximately 950 mK. In contrast, the cell temperature for this spectrum reads approximately 600 mK. A partial explanation of the discrepancy lies in the likely presence of Cr atoms also trapped in the $|^7{\rm S}_3, m_j = +2\rangle$. Atoms in the most trapped $|3;3\rangle$ state have a value of $\mu/\Delta\mu = 6$, while atoms in the $|3;2\rangle$ state have a value of $\mu/\Delta\mu = 3.2$. If all the Cr atoms in the spectrum in Figure B.1 where in state $|3;2\rangle$, then the measured temperature would be 510 mK. As expected, the cell temperature falls

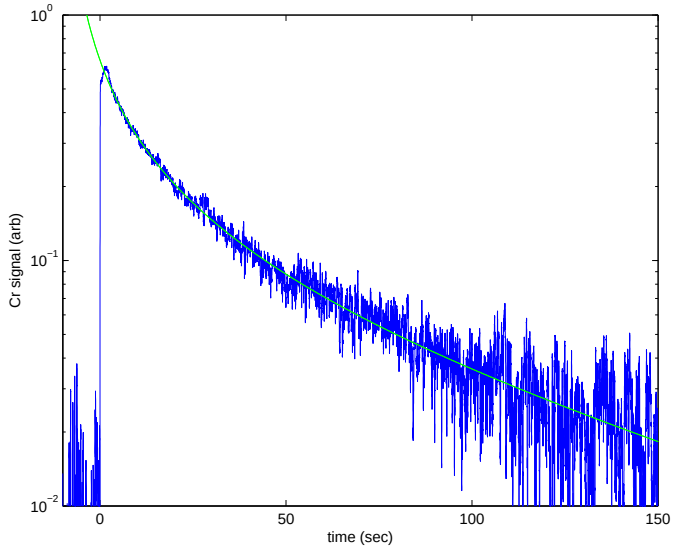

Figure B.2: Cr time decay. Taken using absorption spectrscopy. Cell temperature of 650 mK, trap depth of 2.5 T.

in between the two estimated spectroscopic temperatures. Without more accurate knowledge of the relative distributions of the $|3;3\rangle$ and $|3;2\rangle$ states, it is difficult to calculate a more precise atom temperature from the spectra.

In order to test the reliability of the trap dynamic models, Cr time decays were taken at a range of different cell temperatures and trap depths. Figure B.2 shows a typical time decay of atomic Cr, taken with the laser frequency fixed at the peak of the absorption spectrum. A fit to the data of a (1+2) body decay is used to extract 1-body and 2-body decay rates for each Cr time decay. The results of these measurements are shown in Figures B.3 and B.4. The 1-body loss rates are fitted to the expression for $f_{\mathrm{He}}(\eta)$ plus an additional offset. Agreement is good. The measured Cr two body loss rates are compared to best fit expressions for $k_{2\mathrm{b}} = (k_{\mathrm{el}}/8)(f(\eta) + 1/\gamma)$ for different values of fixed γ. From this analysis, it appears the data implies a $\gamma \approx 5000$, a value

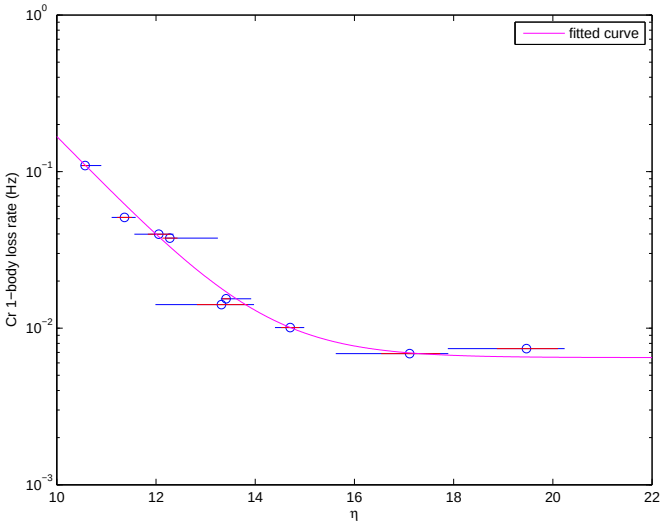

Figure B.3: Cr 1-body loss rates.

about 5 to 10 times larger than previous measurements indicate [44]. The discrepancy again may be due partly to the presence of the $|3;2\rangle$ in the magnet trap, or it may be partly due to a systematic shift in the measured atom temperatures. For the data shown above, the value of η was calculated using the cell thermometer temperature. An increase in the temperature brings the value of η into closer agreement with previous measurements.

Finally, in Figure B.5 we present the observation of Cr trap loss due to the introduction of N_2 process gas behind the closed solenoid valve of the molecular beam source. This data confirmed our suspicion that the molecular beam source was leaking and causing shortened nitrogen trap lifetimes. It also demonstrates the ability of our apparatus to perform collision experiments between a trapped species and an external molecular beam.

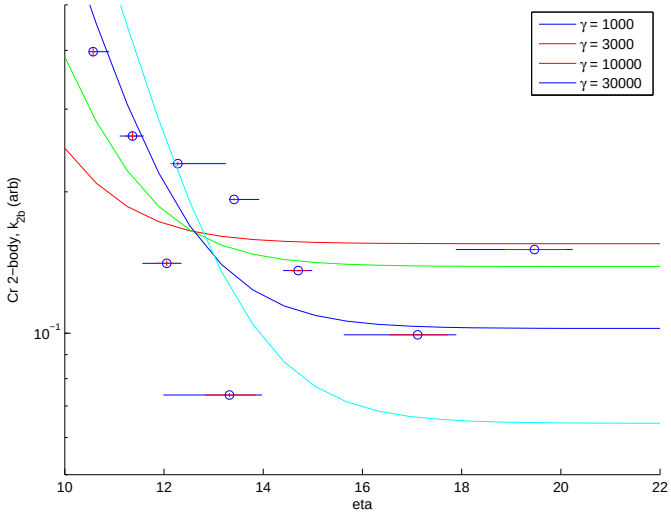

Figure B.4: Cr 2-body loss rates.

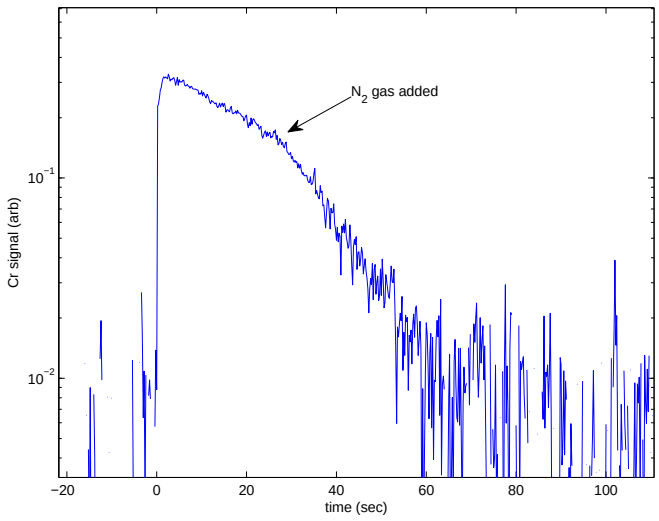

Figure B.5: Cr trap loss due to a leaky solenoid valve in the molecular beam source. N_2 process gas is add to the manifold behind the solenoid valve at appoximately 20 s.

Appendix C

Simulation of Trap Dynamics

In this Appendix we describe the Monte Carlo based molecular dynamics program we use for simulation of atoms colliding in a magnetic trap. The simulation is adapted from and based on the Bird method, also known as Direct Simulation Monte Carlo [107]. The Bird method is well suited for simulating rarified gas dynamics, and is often used to simulate supersonic jet expansions. The method has also been used to simulate evaporative cooling [108] and cross dimensional rethermalization [109] of an isolated atomic gas in a harmonic potential. Here we use it to simulate the dynamics of a trapped gas in the presence of a background helium buffer gas using a close approximation to actual geometry of our magnetic trapping and buffer gas cell.

C.1 Overview of simulation

The direct simulation Monte Carlo technique simulates the molecular dynamics of our trap species. In our trap we typically have more than 10^{12} atoms, ($> 10^{14}$

including helium atoms), which makes simulating the trajectory of each individual atom computationally intractable. The essential idea is to simulate a smaller number of atoms, say 10^5, and let each atom then represent a large number of molecules (10^7 for example) for the purpose of calculating the appropriate collision rates for each individual atom. The program simulates the molecular dynamics by breaking up the problem into discrete time steps. The size of the time step is set to be much smaller than the mean collision time between atoms. In each time step the program executes the following routines:

1. Calculates new position of particles based on individual trajectories and force from external trapping potential.

2. Calculates collision probabilities and chooses pairs of atoms for execution of collisions.

3. Samples positions of all particles to calculate density distribution that is used when calculating collision probabilities.

This sequence is then repeated, and information about the atoms' positions and velocities can be recorded and later analyzed. The calculation of each atoms' trajectory is deterministic, while the collision rates and outgoing collision velocities are determined probabilistically.

The routine for calculating the trajectory of a particle uses a simple "leapfrog" symplectic integration method. The symplectic integration method conserves the energy and angular momentum of the particle in the trap to a high degree, even over long integration times. The force on the particle from the magnetic trapping

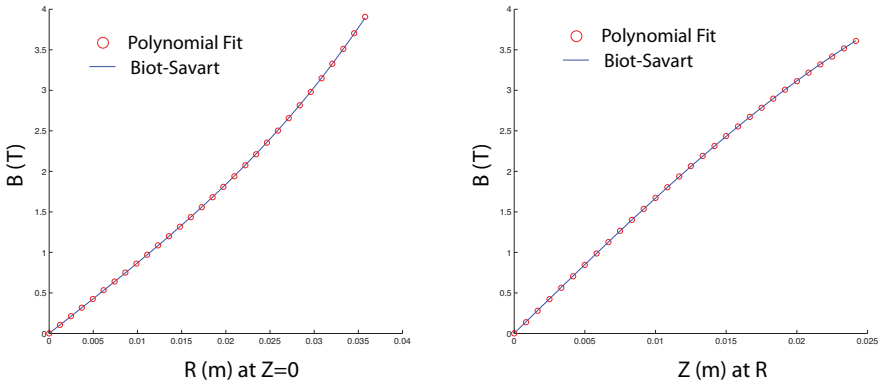

Figure C.1: Polynomial fit to magnetic field. Profile are shown along the radial and z-axis.

field is calculated in one of two ways. In the first case, the force is derived from the simple expression for the ellipsoidal quadrupole field, $U = \mu B_{\max}(r^2 + 4z^2)^{(1/2)}/R_{\max}$, which we used in deriving many of our analytic expressions. In the second case, we calculate the actual trapping magnetic field by integration of the Biot-Savart equation over the volume of our superconducting magnetic trap coils. We then fit an 11-term polynomial to the calculated magnetic field to arrive at an analytic expression for the trapping potential. A comparison of the polynomial fit to the numerical Biot-Savart equation is shown if Figure C.1.

The computational procedure for efficiently choosing collision partners is described in Reference [107]. Essentially it relies on dividing the physical space in the simulation into cells, and each molecule's position is tracked and assigned to the appropriate cell. When choosing collision partners for each particle, the choice is made at random from the set of particles in the same cell. With this technique, the time for choosing collision partners for N total number of particles scales as order N. If instead one chose collision partners for each atom by searching for its nearest neighbor from

the other N particles the process would scale as order N^2, making the process too inefficient for running the simulation. The size of the cells should be small enough that macroscopic properties, such as density and temperature, do not change on the length scale of the cell. At the same time the cells should be large enough to contain about 10 particles. Having larger (i.e. fewer) cells reduces the amount of computation and memory requirements as well. For our simulation we take advantage of the cylindrical symmetry of the trapping geometry and use a two dimensional cell grid. The cells are roughly uniformly spaced in both the radial and axial direction. The radial dimension has 25 cells and the axial direction has 30 cells.

When two particles are chosen to undergo an elastic collision, their positions are left unchanged and their final velocities are calculated using a hard-sphere model. The hard-sphere model calculates the post collision velocities and randomizes the direction of the final velocities in the center-of-mass before transforming them back to the lab frame. For inelastic collisions, one of the atoms is simply removed from the simulation immediately. Incorporating more sophisticated models of elastic and inelastic collisions collisions would be straightforward. For the conditions of the simulations done here, the elastic collision cross section is fairly uniform with collision energy and magnetic field. Nitrogen atoms that undergo inelastic collisions will no longer contribute to the experimentally measured fluorescence signal and are 3 times more weakly trapped. They may undergo about 10 secondary collisions before leaving the trap.

To be able to compare the analytic results derived in Chapter 3 with the results from our simulation, we can set the simulation to enforce the assumptions made in

our analytic calculations. Specifically, we can set that atoms be removed from the trap when they have energy $U > U_{\text{trap}}$, and use the same expression for the trapping potential surface $U(r, z) = U_{\text{trap}}(r^2 + 4z^2)^{1/2}/R$. We can then compare the trap dynamics run under the same conditions, except that we change the code to allow atoms to evaporate only when $r > R_{\text{cell}}$, and we used a polynomial fit to the real trapping potential surface.

The simulation code is written in Fortran 90, and adapted from the example programs provided from reference [107]. The code for calculating the particle trajectories for all atoms has been parallelized using OpenMP to allow for faster execution time on multi-core processors.

C.2 Results of Simulation

The simulations are run for a cell temperature of 600 mK. Initially there 5×10^{12} nitrogen atoms, which corresponds to an initial peak nitrogen density on the order of 10^{12} to 10^{13} cm^{-3}. The background helium density is set to 1.5×10^{11} cm^{-3}. The trap depth is varied between 2.4 to 4.0 T. These conditions are similar to those for which the data is taken. Typical collision rates for these conditions are on the order of 50 Hz. Rethermalization of the kinetic energy distributions typically occurs in about three collisions [109], roughly less than 100 ms. However rethermalization of the high energy tails of the spatial potential energy distributions can take many more than three collisions. Therefore we allow the atoms to evolve in the trap for 3 s of simulation time. One 3 s simulation takes about 15 min to run on a computer. Thus, it is possible to repeat the simulation over several different initial conditions using a

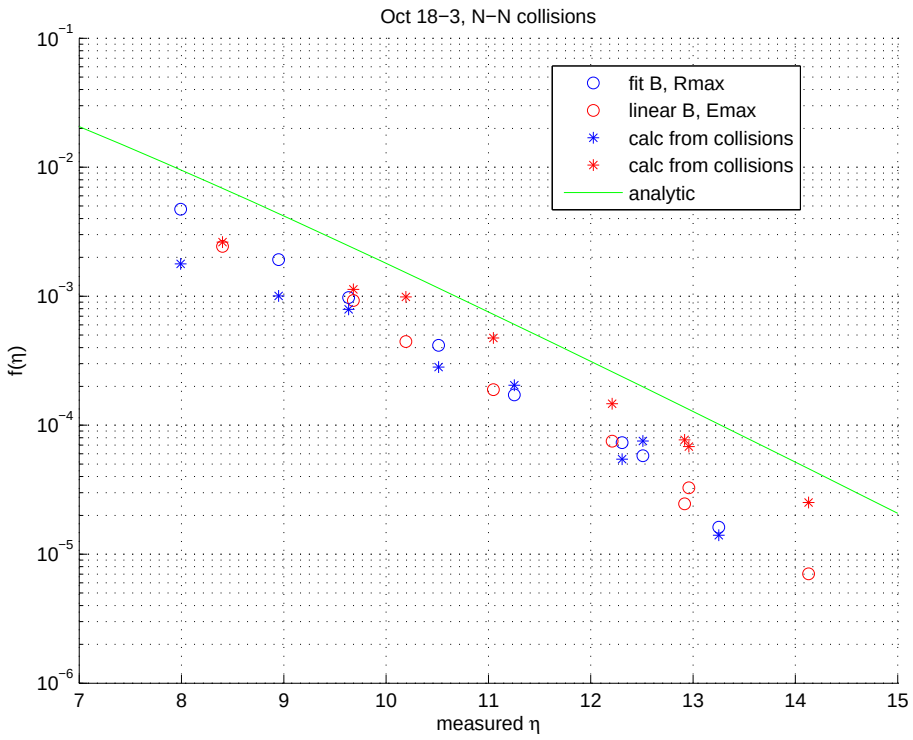

Figure C.2: DSMC simulation, $f(\eta)$.

single computer in the time span of a several hours.

Figures C.2 and C.3 show results for simulations involving only N-N collsions; no helium buffer gas is present.

Figure C.4 show results for simulations where both atomic nitrogen and helium buffer gas are present, but the N-N collision cross section is set to zero to observer the effections N-He collsions.

Finally, Figure C.5 show simulations with atomic nitrogen and helium buffer gas present, and all parameters set to typical values. We see that the temperature of the trapped nitrogen atoms is fixed to the cell temperature for all values of γ.

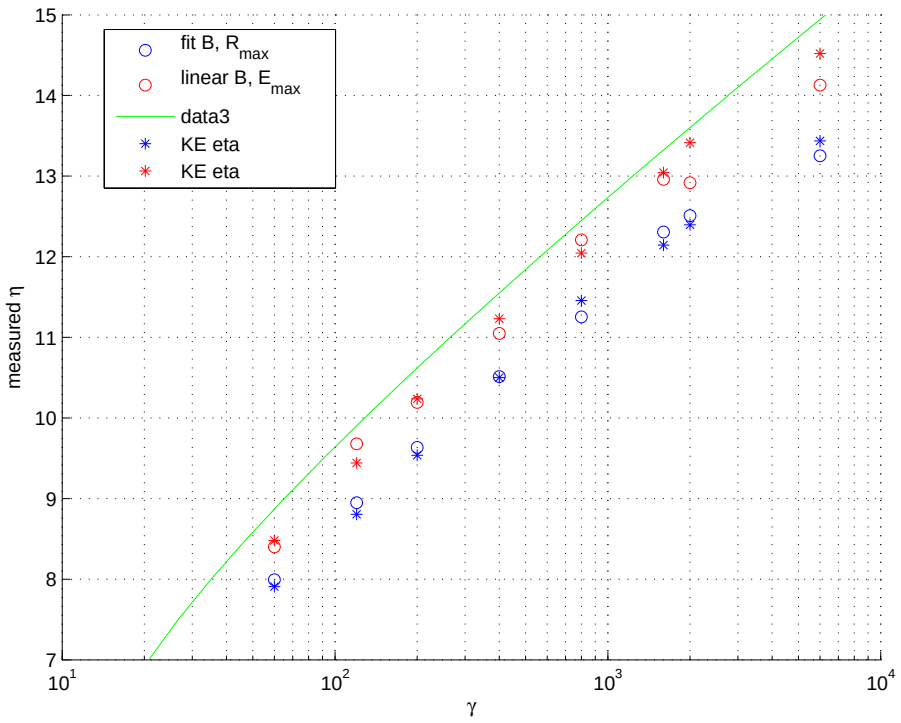

Figure C.3: DSMC simulation, Equilibrium η.

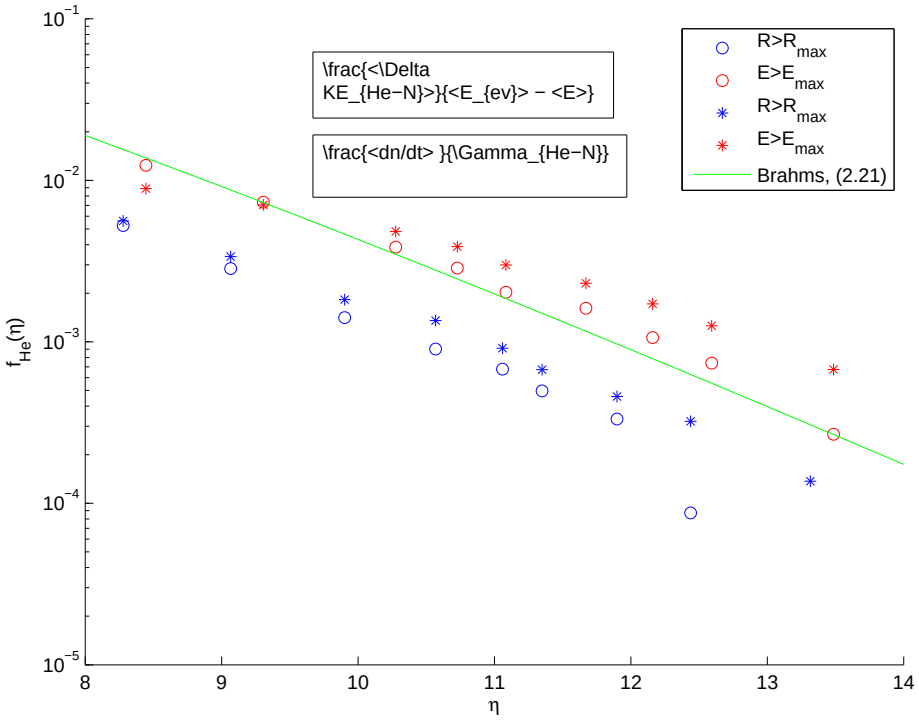

Figure C.4: Fraction of Helium collisions leading to evaporative loss. (Oct 20)

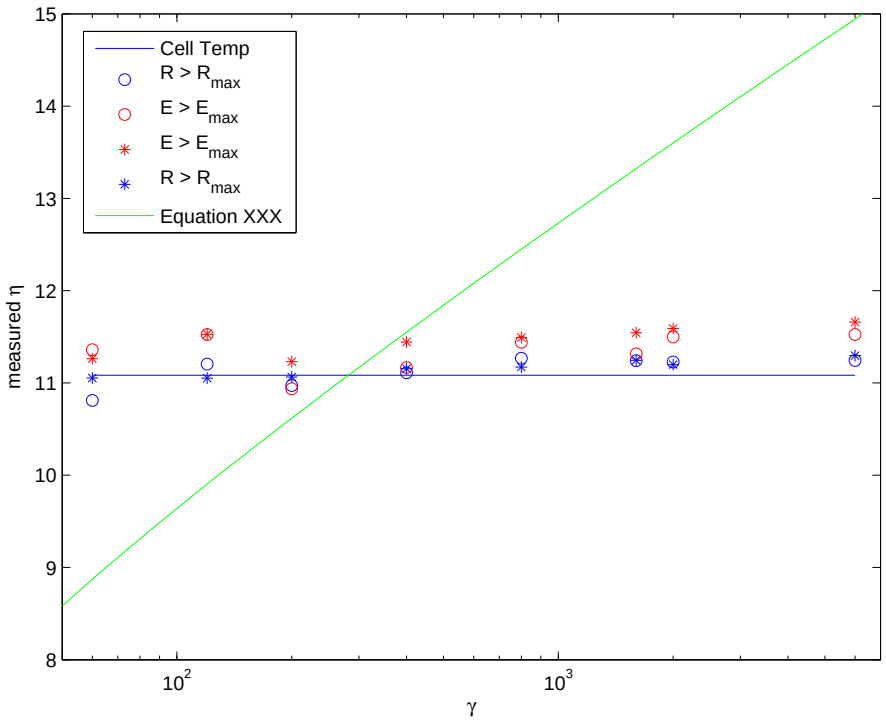

Figure C.5: DSMC simulation, T = 600 mK, Trap Depth = 3.3 T, buffer gas density 1.5×10^{11} cm^{-3}. Initial peak nitrogen density 10^{13} cm^{-3}.

Appendix D

Manganese Monohydride

D.1 Introduction

The goal of this experiment was to investigate the production of the MnH radical via laser ablation. We were motivated to study MnH by recent buffer gas trapping experiments performed by Michael Stoll and coworkers at the Fritz Haber Institute in Berlin[110]. Stoll and coworkers report magnetic trap lifetimes of MnH of 180 ms in the presence of buffer gas densities less than 1×10^{15} cm^{-3}. The NH trapping experiment can beam load atoms into a magnetic trap at buffer gas densities of 5×10^{14} cm^{-3}. This, combined with MnH's large magnetic moment of 6 Bohr magneton, makes MnH a good candidate for magnetic trapping and further studies of collisional Zeeman relaxation. The main experimental hurdle to pursuing these studies is the efficient production of MnH with a method amenable to beam loading into the NH trapping cell.

The experiment described in this Appendix investigates production of the MnH

radical via laser ablation of various solid precursors into a cold (4 to 16 Kelvin) helium or hydrogen buffer gas. Using laser induced fluorescence for detection of the MnH molecules, we estimate about 10^8 MnH molecules are produced per pulse. We concluded that this production rate was not large enough to warrant further pursuit of MnH in the magnetic trapping apparatus. The results of the experiment are summarized below.

D.2 Previous Work on MnH

The spectroscopy of MnH is well known through numerous studies that use molecular beams and laser induced fluorescence (LIF) [111–115]. The MnH for these experiments is produced by either laser ablation or dc discharge sputtering of Mn into a gas flow containing molecular hydrogen. No production numbers are given for these techniques, though they are expected to be low.

For production of MnH in a cold He buffer gas cell, one would like to have a stable, solid precursor that when ablated with a nanosecond pulsed laser produces large amounts ($> 10^9$) of MnH. The Berlin group produced MnH via laser ablation into a cold helium buffer gas of a solid Mn target prepared via electrolysis. For production of MnH from this target, a lower limit of 10^5 was given, as the LIF detection was not calibrated.

For many other molecules studied in this lab, we have seen efficient production of diatomic molecules via laser ablation of a sintered pressed targets that contain the constituent molecules. For example, a sintered pressed target of CaF_2 produces large amounts (10^{13}) of CaF when ablated with a 532 nm pulsed YAG. Unfortunately, it

appears that there does not exist a simple bi-element stable precursor for MnH. Various alkali/alkaline earth-Mn-hydrides have been synthesized, but the process requires pressures of $>$ 1000 bar hydrogen at temperatures of 875 C and yields only small samples [116].

D.3 Preparation of Targets

We decided to investigate three basic types of ablation targets for production of MnH: solid elemental manganese, solid electrolyzed manganese, and composite pressed targets. The first of these, solid Mn, was studied only in a H_2 buffer gas.

The electrolysis of Mn was performed according to the method used by the Berlin group. A Mn chip is suspended in distilled water with a platinum wire that is attached to the negative terminal of a power supply. A second platinum wire is attached to the positive terminal of the power supply and also submerged in the distilled water. The power supply is set at a voltage of 5-10 V and sulfuric acid is added (a few drops) to the water until a current of 100 mA is reached. The electrolysis is allowed to continue for about 1 hour.

Several types of composite pressed targets were made. From investigations in our lab, we know alkali hydrides, such as LiH, when ablated produce large amounts of their atomic constituents. Consequently, a target made from a mixture of LiH powder and Mn powder might be expected to yield MnH. Three pressed targets were made. The first consisting of just Mn powder ($< 10\ \mu$m), the second consisting of Mn powder and LiH powder, and the third consisting of Mn acetate powder. Each of the targets also contained about 5% by weight parrafin wax used as a binder to hold the pressed

target together.

The following procedure was used to create the pressed targets. The target materials + 5% parrafin wax by weight were measured into a glass beaker. A volume of hexanes sufficient to dissolve the wax was then added, and the mixture was place in the ultrasonic mixer for at least a half hour. The hexanes were then allowed to evaporate overnight. The residue left in the beaker the next day was then crushed into small particles. The residue was then put into a stainless steel form (about 0.25 inch outer diameter), and pressed in a hand tightened vice. The resulting targets were then epoxied with Stycast 2850 to a copper sample holder. The samples were then sealed in the buffer gas cell, and the cell filled with 1 atm of H_2 gas and left overnight at room temperature, with the hope that H_2 gas would diffuse in to the targets.

D.4 Experimental Setup

An aluminum buffer gas cell is cooled to about 4 Kelvin in an IR Labs dewar. Helium or H_2 buffer gas is introduced via a stainless steel fill line, and typical buffer gas densities are about 10^{16} to 10^{17} cm^{-3}. When running with H_2 buffer gas, it is necessary to maintain the cell at a temperature of about 15 K, as H_2 freezes at 14 K. To do this, a .25 cm thick stainless steel standoff was inserted in between the cell and heatlink to provide thermal separation from the 4 K bath, and about 400 mW of heat was applied to the cell using a 100 ohm wire wound resistive heater.

The buffer gas cell has three windows, used for laser excitation, ablation, and fluorescence collection. A 532 nm Nd:YAG "Minilite" pulsed laser was used for abla-

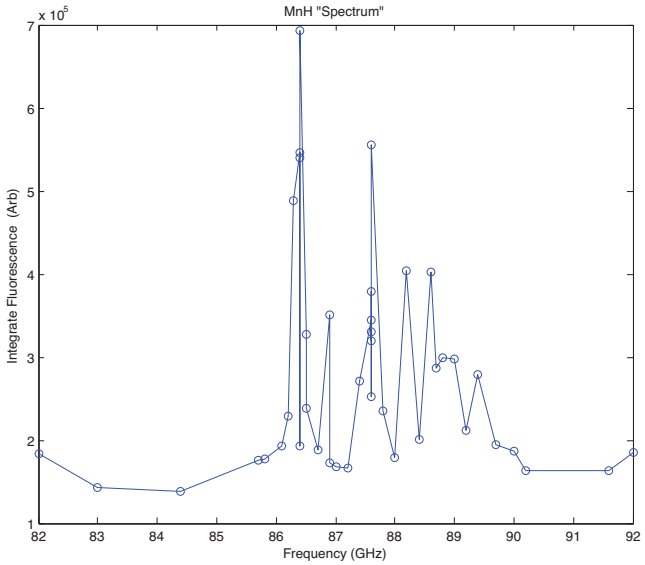

Figure D.1: MnH fluorescence spectrum taken using the Mn powder pressed target.

tion. A Coherent 899 dye laser operating with Rhodamine 6G was used to generate the light at 568 nm used for LIF measurements. A Coherent Wavemaster, Fizeau wavemeter was used to monitor the wavelength of the dye laser. A silicon photodiode was used to measure the transmitted laser intensity. A 1 inch diameter, 50 mm focal length lens is mounted to the cell and used for fluorescence collection. The fluorescence is then focused onto a PMT, which has a 10 nm bandwidth interference filter and colored glass filter to reduce the amount of light reaching the PMT produced from the ablation process. The PMT signal is amplified using a SRS DC-350 MHz pre-amplifier and then sent to an SRS multi channel scaler for photon counting.

Figure **??**, shows a MnH fluorescence spectrum taken using the Mn powder pressed target. The fluctuations in signal are probably due to both the hyperfine splitting of MnH as well as fluctuations from shot-to-shot in ablation yields. Of the samples

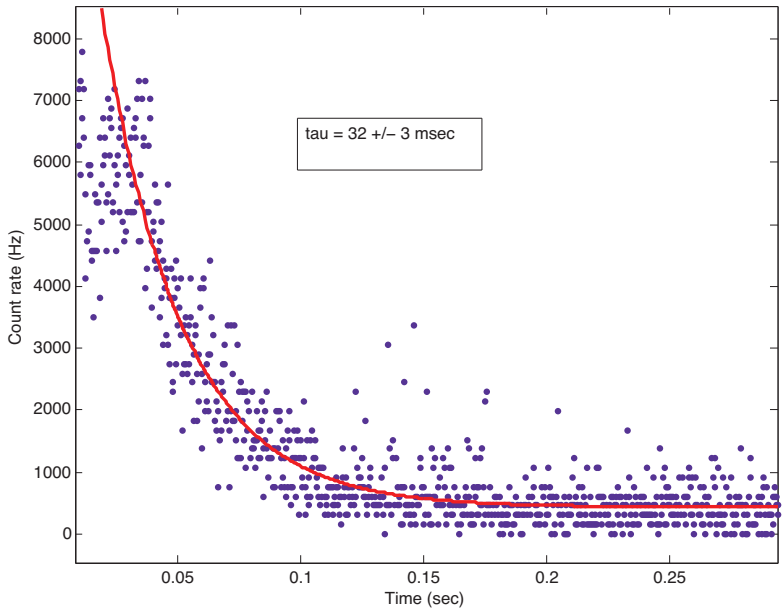

Figure D.2: Typical decay of MnH fluorescence signal.

tested, the two samples that seemed to most reliably yield decent signal were the Mn electrolyzed target and the Mn powder pressed target.

Figure D.2 shows a typical time decay of the MnH signal. The signal is fitted to exponential loss, yielding a $1/e$ lifetime on the order of 30 ms. This lifetime is consistent with loss of MnH to the cell walls after diffusion through the buffer gas. For some species produced via laser ablation, such as bismuth and several lanthanide elements, we have observed fast loss lifetimes (tens of ms) independent of buffer gas density. This process can hinder the efficient loading of atoms or molecules into a magnetic trap. To check to see if this process occurred in MnH we took lifetime measurements at several different buffer gas densities, as show in Figure D.3. The linear dependence of the lifetime on the buffer gas density shows the absence of any

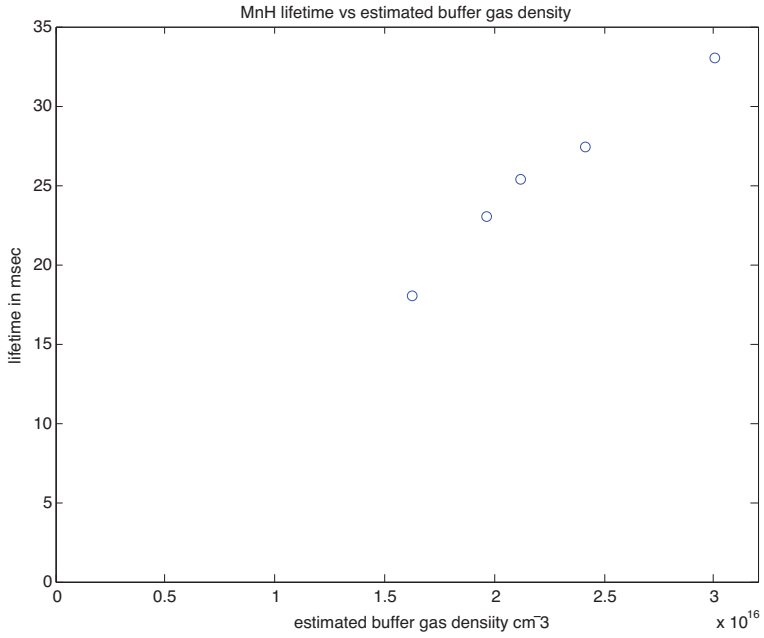

Figure D.3: MnH decay vs approximate buffer gas density, taken with H_2 buffer gas at a temperature of 15 K.

anomalous loss up to buffer gas densities on the order of 3×10^{16} cm^{-3}. At the time this data was taken, no model for this anomalous loss had gained much traction, and it was thought that the loss process might be dependent on the type of ablation target used, even for the same species. The data shown here is for MnH in a H_2 buffer gas at a temperature of 15 K. In the time after this data was taken, one model for the anomalous loss observed in atomic silver is atom-he dimer formation via three body recombination [75]. This suggests that diffusion lifetimes of atoms and molecules should, for the most part, be target indepent.

The MnH ablation yield versus H_2 buffer gas density was also studied. Figure D.4 shows individual decay traces of MnH fluorescence signal taken at different H_2 buffer gas densities. As the buffer gas increases, the peak signal size decreases and occurs

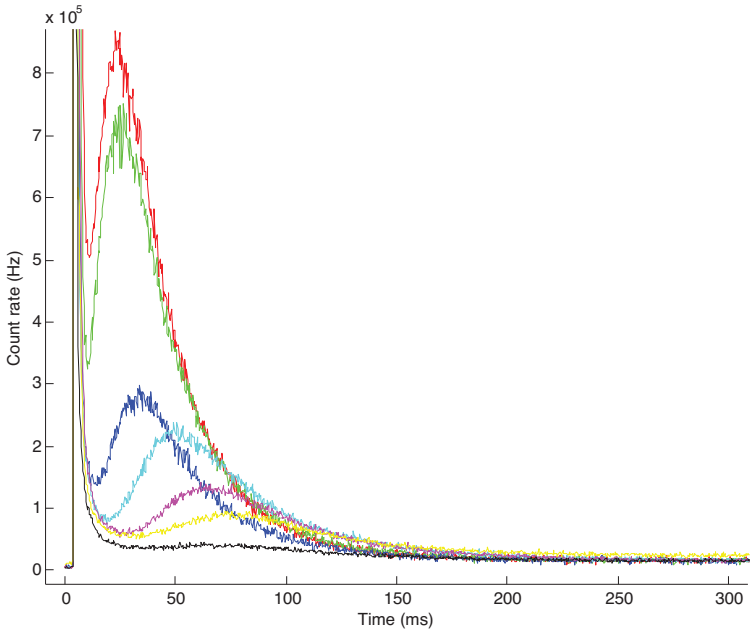

Figure D.4: Individual traces of MnH fluorescence signal taken at different H2 buffer gas densities.

at a later time after the ablation pulse. Presumably the delay of the peak at higher buffer gas density occurs from the MnH molecules taking a longer to diffuse into the fluorescence detection region. This systematic effect prevents any quantitative information about total MnH yield from being extracted. It is likely that the MnH ablation yield is fairly uniform over the buffer gas densities shown here.

Bibliography

[1] L. D. Carr, D. DeMille, R. V. Krems, and J. Ye, New Journal of Physics **11**, 055049 (2009), and references therein.

[2] J. J. Gilijamse, S. Hoekstra, S. Y. T. van de Meerakker, G. C. Groenenboom, and G. Meijer, Science **313**, 1617 (2006).

[3] B. C. Sawyer, B. K. Stuhl, D. Wang, M. Yeo, and J. Ye, Physical Review Letters **101**, 203203 (2008).

[4] S. V. Alyabyshev, T. V. Tscherbul, and R. V. Krems, Physical Review A (Atomic, Molecular, and Optical Physics) **79**, 060703 (pages 4) (2009), URL `http://link.aps.org/abstract/PRA/v79/e060703`.

[5] D. Edvardsson, C. F. Williams, and D. C. Clary, Chem. Phys. Lett. **431**, 261 (2006).

[6] M. Akyilmaz, D. R. Flower, P. Hily-Blant, G. P. des Forets, and C. M. Walmsley, Astron. Astrophys. p. 221 (2007).

[7] N. Balakrishnan and A. Dalgarno, Chem. Phys. Lett. **341**, 652 (2001).

[8] R. V. Krems, Int. Rev. Phys. Chem **24**, 99 (2005).

[9] S. Maret, E. A. Bergin, and C. J. Lada, Nature **442**, 425 (2006).

[10] D. C. Knauth, B.-G. Anderson, S. R. McCandliss, and H. W. Moos, Nature **429**, 636 (2004).

[11] A. Sternberg and A. Dalgarno, Astrophys. J. Supp. Ser. **99**, 565 (1995).

[12] T. J. Frankcombe and G. Nyman, J. Phys. Chem. A **111**, 13163 (2007).

[13] M. T. Bell and T. P. Softley, Molecular Physics **107**, 99 (2009).

[14] I. W. M. Smith, Angewandte Chemie-International Edition **45**, 2842 (2006).

[15] D. Carty, A. Goddard, S. P. K. Kohler, I. R. Sims, and I. W. M. Smith, The Journal of Physical Chemistry A **110**, 3101 (2005), URL http://dx.doi.org/10.1021/jp054429u.

[16] J. J. Hudson, B. E. Sauer, M. R. Tarbutt, and E. A. Hinds, Phys. Rev. Lett. **89**, 023003 (2002).

[17] A. C. Vutha, W. C. Campbell, Y. V. Gurevich, N. R. Hutzler, M. Parsons, D. Patterson, E. Petrik, B. Spaun, J. M. Doyle, G. Gabrielse, et al., J. Phys. B: At. Mol. Opt. Phys (2010), accepted for publication, arXiv:0908.2412v1 [physics.atom-ph].

[18] V. V. Flambaum and M. G. Kozlov, Physical Review Letters **99**, 150801 (pages 4) (2007), URL http://link.aps.org/abstract/PRL/v99/e150801.

[19] D. DeMille, S. Sainis, J. Sage, T. Bergeman, S. Kotochigova, and E. Tiesinga, Physical Review Letters **100**, 043202 (pages 4) (2008), URL http://link.aps.org/abstract/PRL/v100/e043202.

[20] T. Zelevinsky, S. Kotochigova, and J. Ye, Physical Review Letters **100**, 043201 (pages 4) (2008), URL http://link.aps.org/abstract/PRL/v100/e043201.

[21] R. Barnett, D. Petrov, M. Lukin, and E. Demler, Physical Review Letters **96**, 190401 (pages 4) (2006), URL http://link.aps.org/abstract/PRL/v96/e190401.

[22] D. DeMille, Physical Review Letters **88**, 067901 (2002).

[23] A. O. G. Wallis and J. M. Hutson (2009), arXiv:0906.5314v2 [physics.chem-ph].

[24] K. K. Ni, S. Ospelkaus, M. H. G. de Miranda, A. Pe'er, B. Neyenhuis, J. J. Zirbel, S. Kotochigova, P. S. Julienne, D. S. Jin, and J. Ye, Science **322**, 231 (2008).

[25] N. Nemitz, F. Baumer, F. Muenchow, S. Tassy, and A. Goerlitz, Physical Review a **79**, 061403 (2009).

[26] J. D. Weinstein, R. deCarvalho, T. Guillet, B. Friedrich, and J. M. Doyle, Nature **395**, 148 (1998).

[27] S. van de Meerakker, N. Vanhaecke, and G. Meijer, Annu. Rev. Phys. Chem. **57**, 159 (2006).

[28] E. Narevicius, A. Libson, C. G. Parthey, I. Chavez, J. Narevicius, U. Even, and M. G. Raizen, Phys. Rev. Lett. **100**, 093003 (2008).

[29] S. D. Hogan, A. W. Wiederkehr, H. Schmutz, and F. Merkt, Phys. Rev. Lett. **101**, 143001 (2008).

[30] R. Fulton, A. Bishop, and P. Barker, Phys. Rev. Lett. **93**, 243004 (2004).

[31] M. S. Elioff, J. J. Valentini, and D. W. Chandler, Science **302**, 5652 (2003).

[32] B. K. Stuhl, B. C. Sawyer, D. Wang, and J. Ye, Physical Review Letters **101**, 243002 (2008).

[33] E. S. Shuman, J. F. Barry, D. R. Glenn, and D. DeMille, Physical Review Letters **103**, 223001 (pages 4) (2009), URL `http://link.aps.org/abstract/PRL/v103/e223001`.

[34] P. S. Żuchowski and J. M. Hutson (2009), `arXiv:0902.4548v2 [physics.chem-ph]`.

[35] P. J. Leo, E. Tiesinga, P. S. Julienne, D. K. Walter, S. Kadlecek, and T. G. Walker, Phys. Rev. Lett. **81**, 1389 (1998).

[36] R. Krems, G. Groenenboom, and A. Dalgarno, J. Phys. Chem. A **108**, 8941 (2004).

[37] C. I. Hancox, S. C. Doret, M. T. Hummon, R. V. Krems, and J. M. Doyle, Physical Review Letters **94**, 013201 (2005).

[38] S. E. Maxwell, M. T. Hummon, Y. Wang, A. A. Buchachenko, R. V. Krems, and J. M. Doyle, Phys. Rev. A **78**, 042706 (2008).

[39] R. Krems, A. Dalgarno, N. Balakrishnan, and G. Groenenboom, Phys. Rev. A **67**, 060703 (2003).

[40] R. V. Krems, H. R. Sadeghpour, A. Dalgarno, D. Zgid, J. Klos, and G. Chalasinski, Phys. Rev. A **68**, 051401(R) (2003).

[41] W. Campbell, T. Tscherbul, H. Lu, E. Tsikata, R. Krems, and J. Doyle, Physical Review Letters **102**, 13003 (2009).

[42] A. O. G. Wallis and J. M. Hutson, Phys. Rev. Lett. **103**, 183201 (2009).

[43] P. S. Zuchowski and J. M. Hutson, Physical Review A **78**, 022701 (pages 9) (2008), URL `http://link.aps.org/abstract/PRA/v78/e022701`.

[44] S. V. Nguyen, R. deCarvalho, and J. M. Doyle, Phys. Rev. A **75**, 062706 (2007).

[45] S. Hensler, J. Werner, A. Griesmaier, P. Schmidt, A. G
"orlitz, T. Pfau, S. Giovanazzi, and K. Rzażewski, Applied Physics B: Lasers and Optics **77**, 765 (2003).

[46] Z. Pavlovic, R. Krems, R. Cote, and H. Sadeghpour, Phys. Rev. A **71**, 061402 (2005).

[47] C. I. Hancox, S. C. Doret, M. T. Hummon, L. J. Luo, and J. M. Doyle, Nature **431**, 281 (2004).

[48] J. Weinstein, R. deCarvalho, T. Guillet, B. Friedrich, and J. Doyle, Nature **395**, 148 (1998).

[49] M. Lara, J. L. Bohn, D. E. Potter, P. Soldan, and J. M. Hutson, Phys. Rev. A **75**, 012704 (2007).

[50] I. S. Lim, M. Pernpointner, M. Seth, J. K. Laerdahl, and P. Schwerdtfeger, Phys. Rev. A **60**, 2822 (1999).

[51] J. Stiehler and J. Hinze, J. Phys. B: At. Mol. Opt. Phys. **28**, 4055 (1995).

[52] J. Mitroy and J.-Y. Zhang, J Chem Phys **128**, 134305 (2008).

[53] H. Gollisch, Journal of Physics B: Atomic and Molecular Physics **17**, 1463 (1984).

[54] D. A. Crosby and D. A. Crosby, Physical Review A **16**, 488 (1977).

[55] Y. Ralchenko, F.-C. Jou, D. Kelleher, A. Kramida, A. Musgrove, J. Reader, W. Wiese, and K.Olsen, *NIST atomic spectra database, (version 3.1.3), [online]*, URL `http://physics.nist.gov/asd3`.

[56] P. Soldán, P. S. Żuchowski, and J. M. Hutson, Faraday Discuss. **142**, 191 (2009), `arXiv:0901.2493v2 [physics.chem-ph]`.

[57] T. E. Mehlstaeubler, K. Moldenhauer, M. Riedmann, N. Rehbein, J. Friebe, E. M. Rasel, and W. Ertmer, Phys. Rev. A **77**, 021402 (2008).

[58] A. Derevianko, W. Johnson, M. Safronova, and J. Babb, Physical Review Letters **82**, 3589 (1999).

[59] D. M. Egorov, Ph.D. thesis, Harvard University (2004).

[60] W. C. Campbell, Ph.D. thesis, Harvard University (2008).

[61] E. Tsikata, Ph.D. thesis, Harvard University (2009).

[62] M. Moldovan, L. S. Hirsch, A. J. Ptak, C. D. Stinespring, T. H. Myers, and N. C. Giles, J. Electron. Mater. **27**, 756 (1998).

[63] T. Nakayama, K. Takahashi, Y. Matsumi, N. Taniguchi, and S. Hayashida, Journal of Geophysical Research-Atmospheres **108**, 4668 (2003).

[64] K. S. Eikema and K. S. E. Eikema, Physical Review Letters **86**, 5679 (2001).

[65] M. Scheid, D. Kolbe, F. Markert, T. W. Hänsch, and J. Walz, Opt. Express **17**, 11274 (2009), URL `http://www.opticsexpress.org/abstract.cfm?URI=oe-17-14-11274`.

[66] W. BISCHEL, B. PERRY, and D. CROSLEY, Applied Optics **21**, 1419 (1982).

[67] S. F. Adams and T. A. Miller, Chem. Phys. Lett. **295**, 305 (1998).

[68] K. Omidvar, Phys. Rev. A **22**, 1576 (1980), **30**, 2805(E) (1985).

[69] I. Gerhardt, G. Wrigge, G. Zumofen, J. Hwang, A. Renn, and V. Sandoghdar, Physical Review A (Atomic, Molecular, and Optical Physics) **79**, 011402 (pages 4) (2009), URL `http://link.aps.org/abstract/PRA/v79/e011402`.

[70] R. deCarvalho, Ph.D. thesis, Harvard University (2003).

[71] R. Michniak, Ph.D. thesis, Harvard University (2004).

[72] J. D. Weinstein, Ph.D. thesis, Harvard University (2001).

[73] W. Ketterle and N. VanDruten, Adv. At. Mo. Opt. Phys. **37**, 181 (1996), advances In Atomic, Molecular, and Optical Physics, Vol 37.

[74] O. Luiten, M. Reynolds, and J. Walraven, Physical Review a **53**, 381 (1996).

[75] N. Brahms, Ph.D. thesis, Harvard University (2008).

[76] J. D. Weinstein, R. deCarvalho, C. I. Hancox, and J. M. Doyle, Phys. Rev. A **65**, 021604(R) (2002).

[77] S. C. Doret, Ph.D. thesis, Harvard University (2009).

[78] F. Pobell, *Matter and methods at low temperatures* (Springer-Verlag, Berlin, 1996), 2nd ed., ISBN 3540585729 (Berlin : alk. paper).

[79] D. G. Fried, Ph.D. thesis, Massachusetts Institute of Technology (1999).

[80] S. Doret, C. Connolly, W. Ketterle, and J. Doyle, Physical Review Letters **103**, 103005 (2009).

[81] J. Corless, J. West, J. Bromage, and C. Stroud, Review of Scientific Instruments **68**, 2259 (1997).

[82] E. Eyler, A. Yiannopoulou, S. Gangopadhyay, and N. Melikechi, Optics Letters **22**, 49 (1997).

[83] S. Hannemann, E.-J. van Duijn, and W. Ubachs, Review of Scientific Instruments **78**, 103102 (pages 9) (2007), URL `http://link.aip.org/link/?RSI/78/103102/1`.

[84] M. Hori and A. Dax, Optics Letters **34**, 1273 (2009).

[85] I. D. Setija and I. D. Setija, Physical Review Letters **70**, 2257 (1993).

[86] T. Nakayama, K. Takahashi, and Y. Matsumi, Geophysical Research Letters **32**, L24803 (2005).

[87] P. Zhang, V. Kharchenko, A. Dalgarno, Y. Matsumi, T. Nakayama, and K. Takahashi, Phys. Rev. Lett. **100**, 103001 (2008).

[88] S. Maxwell, N. Brahms, R. deCarvalho, D. Glenn, J. Helton, S. Nguyen, D. Patterson, J. Petricka, D. DeMille, and J. Doyle, Physical Review Letters **95**, 173201 (2005).

[89] D. Patterson and J. M. Doyle, Journal of Chemical Physics **126**, 154307 (2007).

[90] J. P. Beardmore, A. J. Palmer, K. C. Kuiper, and R. T. Sang, Review of Scientific Instruments **80**, 073105 (pages 5) (2009), URL `http://link.aip.org/link/?RSI/80/073105/1`.

[91] W. G. Kaenders, F. Lison, I. Müller, A. Richter, R. Wynands, and D. Meschede, Phys. Rev. A **54**, 5067 (1996).

[92] L. D. van Buuren, C. Sommer, M. Motsch, S. Pohle, M. Schenk, J. Bayerl, P. W. H. Pinkse, and G. Rempe, Physical Review Letters **102**, 033001 (2009).

[93] S. D. Hogan, D. Sprecher, M. Andrist, N. Vanhaecke, and F. Merkt, Physical Review A (Atomic, Molecular, and Optical Physics) **76**, 023412 (pages 11) (2007), URL `http://link.aps.org/abstract/PRA/v76/e023412`.

[94] E. GORDON, L. MEZHOVDEGLIN, O. PUGACHEV, and V. KHMELENKO, Cryogenics **16**, 555 (1976).

[95] T. Czerwiec, F. Greer, and D. Graves, Journal of Physics D-Applied Physics **38**, 4278 (2005).

[96] D. Voulot, R. McCullough, W. Thompson, D. Burns, J. Geddes, G. Cosimini, E. Nelson, P. Chow, and J. Klaassen, Journal of Vacuum Science & Technology A-Vacuum Surfaces and Films **16**, 3434 (1998).

[97] D. J. Bamford, L. E. Jusinski, and W. K. Bischel, Phys. Rev. A **34**, 185 (1986).

[98] D. J. Bamford, M. J. Dyer, and W. K. Bischel, Phys. Rev. A **36**, 3497 (1987).

[99] D. J. Bamford, H. A. P, M. J. Dyer, and W. K. Bischel, Journal of the Optical Society of America B-Optical Physics **5**, 1369 (1988).

[100] R. SAXON and J. EICHLER, Physical Review a **34**, 199 (1986).

[101] T. MCILRATH, R. HUDSON, A. AIKIN, and T. WILKERSON, Applied Optics **18**, 316 (1979).

[102] W. Wiese, J. Fuhr, and T. Deters, Journal of Physical and Chemical Reference Data pp. 1–& (1996).

[103] K. L. Bell and A. E. Kingston, Adv. At. Mo. Opt. Phys. **32**, 1 (1994).

[104] M. LITTMAN, Optics Letters **3**, 138 (1978).

[105] T. KAJAVA, H. LAURANTO, and R. SALOMAA, Applied Optics **31**, 6987 (1992).

[106] L. WESTLING, M. RAYMER, and J. SNYDER, Journal of the Optical Society of America B-Optical Physics **1**, 150 (1984).

[107] G. A. Bird, *Molecular gas dynamics and the direct simulation of gas flows*, Oxford engineering science series ;42 (Clarendon Press ;Oxford University Press,, Oxford :New York :, 1995).

[108] H. Wu and H. Wu, Physical Review A **56**, 560 (1997).

[109] W. Huang and J. Christopher, J. Phys. B: At. Mol. Opt. Phys **29**, L321 (1996).

[110] M. Stoll, J. M. Bakker, T. C. Steimle, G. Meijer, and A. Peters, Physical Review A (Atomic, Molecular, and Optical Physics) **78**, 032707 (pages 8) (2008), URL `http://link.aps.org/abstract/PRA/v78/e032707`.

[111] J. J. Gengler, T. C. Steimle, J. J. Harrison, and J. M. Brown, Journal of Molecular Spectroscopy **241**, 192 (2007).

[112] T. D. Varberg, R. W. Field, and A. J. Merer, Journal of Chemical Physics **95**, 1563 (1991).

[113] T. D. Varberg, R. W. Field, and A. J. Mere, Journal of Chemical Physics **92**, 7123 (1990).

[114] T. D. Varberg, J. A. Gray, R. W. Field, and A. J. Merer, Journal of Molecular Spectroscopy **156**, 296 (1992).

[115] S. R. Langhoff, C. W. Bauschlicher, Jr., and A. P. Rendell, J. Mol. Spectr. **138**, 108 (1989).

[116] H. Blomqvist, E. Ronnebro, D. Kyoi, T. Sakai, and D. Noreus, Journal of Alloys and Compounds **358**, 82 (2003).